DTIC FILE COPY

AD-A230 440

DTIC
ELECTE
JAN 07 1991
S E D

DEPARTMENT OF THE AIR FORCE

AIR UNIVERSITY

AIR FORCE INSTITUTE OF TECHNOLOGY

Wright-Patterson Air Force Base, Ohio

DISTRIBUTION STATEMENT A
Approved for public release;
Distribution Unlimited

91 1 3 181

AF I/GAE/ENY/90D-27

COMPUTATIONAL INVESTIGATION OF CIRCULATION CONTROL TURBULENCE MODELING

THESIS

T. Bryan Scruggs
Captain, USAF

AFIT/GAE/ENY/90D-27

Approved for public release; distribution unlimited

AFIT/GAE/ENY/90D-27

COMPUTATIONAL INVESTIGATION OF CIRCULATION CONTROL TURBULENCE MODELING

THESIS

Presented to the faculty of the School of Engineering

of the Air Force Institute of Technology

Air University

In Partial Fulfillment of the

Requirements for the Degree of

Master of Science in Aeronautical Engineering

T. Bryan Scruggs, B.S.

Captain, USAF

December, 1990

Accession For
NTIS GRA&I
DTIC TAB
Unannounced
Justification
By
Distribution/
Availability Codes
Dist | Avail and/or Special
A-1

Approved for public release; distribution unlimited

ACKNOWLEDGEMENTS

It took more than just the one name on the cover to complete this report. My thesis advisor, Dr Franke, provided much needed support and direction for which I am thankful. Without Dr Shang's sponsorship and support this thesis would not have been achieved. Thanks to Dr Visbal for his patience in answering all my questions. I would like to thank all of the members of Dr Shang's organization for their computer support and assistance. Thanks to all the people in WRDC/FIMM who devoted much of their time to helping me generate and refine the computational grids. And thanks to Steve Williams for his presence whenever I had another question.

Another special thanks goes to my classmates and to the memory of Wayne Wilsdon. Without them to help me along, I would have never gotten to this point.

Finally, I would like to thank my wife. Thank you Alice for all of your deeply appreciated assistance.

T. Bryan Scruggs

TABLE OF CONTENTS

	Page
Acknowledgements	ii
List of Figures	v
List of Tables	viii
List of Symbols	ix
Abstract	xiii
I. Introduction	1
1.1 Background	3
1.2 Objective	6
II. Analysis	8
2.1 Governing Equations	8
2.2 Numerical Implementation	17
2.3 Boundary Conditions	20
2.4 Turbulence Model and Point of Transition	23
2.5 Grid Generation	26
III. Results and Discussion	31
3.1 Circular Cylinder	31
3.2 103RE Airfoil	45
IV. Conclusions	76
4.1 Circular Cylinder	76
4.2 103RE Airfoil	77
V. Recommendations	79
Appendix A. Non-dimensional Variables	80
Appendix B. Jacobian Matrices	83

Appendix C. Program Inputs 86
Appendix D. Cylinder Flow Regimes 92
Appendix E. Data Point 35 Plots 98
Appendix F. Data Point 36 Plots 104
Bibliography 113
Vita 116

List of Figures

Figure		Page
1.	Circulation Control Airfoil Geometry.	2
2.	Inner Region of Airfoil Grid.	28
3.	Jet Exit/Coanda Surface Region of Airfoil Grid. . .	29
4.	Jet Exit Region of Airfoil Grid	30
5.	Velocity vectors, cylinder w/o slot, Re=40.	33
6.	Slotted cylinder geometry	35
7.	Abnormal velocities at slot exit, Re=40	35
8.	Cylinder Drag Oscillations.	38
9.	Vortex shedding from slot, Re=$3x10^6$, C_μ=0	39
10.	Vortex shedding from slot, Re=$3x10^6$, C_μ=0.	40
11.	Velocity vectors, cylinder w/slot, Re=$3x10^6$, C_μ=0.	41
12.	Mach Contours, data point 35, Bradshaw=0	47
13.	Velocity Vectors, data point 35, Bradshaw=0. . . .	48
14.	Velocity Vectors, data point 35, Bradshaw=4. . . .	49
15.	Velocity Vectors, data point 35, Bradshaw=10 . . .	51
16.	Mach Contours, data point 35, Bradshaw=25.	52
17.	Velocity Vectors, data point 35, Bradshaw=25 . . .	53
18.	Shrewsbury's Computational Streamlines	54
19.	Shrewsbury's Experimental Streamlines.	54
20.	C_l versus Bradshaw, data point 35.	56
21.	C_d versus Bradshaw, data point 35.	57
22.	C_μ versus Bradshaw, data point 35.	58
23.	C_μ versus Bradshaw, data point 35.	59

24. C_l versus Bradshaw, data point 35. 61
25. C_d versus Bradshaw, data point 35. 62
26. C_m versus Bradshaw, data point 35. 63
27. Mach Contours, data point 36, Bradshaw=0 65
28. Velocity Vectors, data point 36, Bradshaw=0. . . . 66
29. Mach Contours, data point 36, Bradshaw=4 67
30. Velocity Vectors, data point 36, Bradshaw=4. . . . 68
31. Mach Contours, data point 36, Bradshaw=23. 69
32. Velocity Vectors, data point 36, Bradshaw=23 . . . 70
33. C_l versus Bradshaw, data point 36. 72
34. C_d versus Bradshaw, data point 36. 73
35. C_m versus Bradshaw, data point 36. 74
36. C_μ versus Bradshaw, data point 36. 75
37. C_d versus Reynolds number for a cylinder 95
38. Reynolds number affects in super to transcritical. 96
39. Power spectra of Lift Fluctuations 97
40. Velocity vectors, data point 35, Bradshaw=2. . . . 99
41. Velocity vectors, data point 35, Bradshaw=8. . . . 100
42. Velocity vectors, data point 35, Bradshaw=14 . . . 101
43. Velocity vectors, data point 35, Bradshaw=20 . . . 102
44. Velocity vectors, data point 35, Bradshaw=20 . . . 103
45. Mach contours, data point 36, Bradshaw=2 105
46. Velocity vectors, data point 36, Bradshaw=2. . . . 106
47. Velocity vectors, data point 36, Bradshaw=6. . . . 107
48. Velocity vectors, data point 36, Bradshaw=10 . . . 108
49. Velocity vectors, data point 36, Bradshaw=14 . . . 109
50. Velocity vectors, data point 36, Bradshaw=18 . . . 110

51. Velocity vectors, data point 36, Bradshaw=20 . . . 111

52. Velocity vectors, data point 36, Bradshaw=20 . . . 112

List of Table

Table	Page
1. Computational and Experimental Test Conditions. . .	46

List of Symbols

Symbols	Description
A	Jacobian matrix
B	Jacobian matrix
C	Courant number
C_d	Drag coefficient
C_{df}	Drag coefficient due to friction
C_{dp}	Drag coefficient due to pressure
C_l	Lift coefficient
C_m	Moment coefficient
C_p	Momentum coefficient
$C_{1,2}$	Constants in Southerland's viscosity formula
c	Chord length
c_p	Specific heat at constant pressure
D_e	Explicit fourth order damping term
D_η, D_ξ	Implicit second order damping terms
E_t	Total Energy
e	Internal energy
F	Bradshaw curvature correction factor
F	Flux vector (x-direction)
$\tilde{F}$	Transformed flux vector
$\tilde{F}_l$	Non-viscous flux vector
$\vec{f}$	Body force vector
G	Flux vector (y-direction)
$\tilde{G}$	Transformed flux vector

$\vec{G}_I$	Non-viscous flux vector
I	Identity matrix
J	Transformation Jacobian
k	Coefficient of thermal conductivity
k_t	Turbulent coefficient of thermal conductivity
l	Boundary layer mixing length
M	Mach number
$\dot{m}_j$	Jet mass flow rate
n	normal direction
Pr	Prandtl number
Pr_t	Turbulent Prandtl number
p	Static pressure
p_c	Total pressure
p_∞	Freestream static pressure
Q	Heat generation
$\vec{q}$	Heat flux vector
q_∞	Freestream dynamic pressure
R	Universal gas constant, Jacobian matrix
S	Jacobian matrix
T	Static temperature
T_{PR}	Jet total pressure ratio
T_{TR}	Jet total temperature ratio
T_0	Total temperature
T_∞	Freestream static temperature
t	Time
U	Vector of dependent variables
U_∞	Freestream velocity

$\tilde{U}$	Transformed vector of dependent variables
u	X-component of velocity vector
u_c	Contravariant velocity
$\vec{V}$	Velocity vector
V, V_1, V_2	Viscous flux vectors
v	Y-component of velocity vector
v_c	Contravariant velocity
v_j	Jet exit velocity
W, W_1, W_2	Viscous flux vectors
x	Cartesian coordinate axis (streamwise)
y	Cartesian coordinate axis (normal)
α	Angle of attack
γ	Ratio of specific heats
Δ	Difference operator
δ	Central difference operator
δ_{ij}	Kronecker delta function
ϵ	Turbulent eddy viscosity
η	Computational coordinate axis (normal)
θ	Empirical curvature correction constant
λ	Stokes' viscosity hypothesis
λ_t	Turbulent Stokes' viscosity hypothesis
μ	Molecular viscosity
ξ	Computational coordinate axis (tangential)
ρ	Static density
ρ_∞	Freestream static density
$\underline{\sigma}$	Stress Tensor
$\underline{\tau}$	Viscous stress tensor

ϕ	Angle between x-axis and jet normal vector
ω	Vorticity
ω_e, ω_i	Damping coefficients
∇	Del operator

ABSTRACT

A computational study of the turbulence model parameters and their effect on the flow field of a circulation control airfoil was conducted. A Beam-Warming algorithm was used to solve the Navier-Stokes equations for flow around a circulation control airfoil. The turbulence model was a modified Baldwin-Lomax model. The modification was from Bradshaw and based on the extra strain rates produced by streamline curvature. Included in the modification is an empirical curvature correction constant, the Bradshaw constant. The effect of this empirical curvature correction on the flow about an airfoil was analyzed.

Using the simple geometry of a cylinder, the effects of the Bradshaw constant on the flow field were to be monitored. The effects of the Bradshaw constant on the flow field about the cylinder were then to be compared to the effects of the Bradshaw constant on the flow field about a circulation control airfoil. By comparing these two different but yet similar flow fields, the application of the Bradshaw modification to various geometries was to be analyzed. Comparison of the effects of the Bradshaw constant on the two flow fields was to provide an assessment of the sensitivity of the Bradshaw correction to different situations. The questionable convergence or non-convergence

of the solution for the cylinder precluded this cross correlation. However, a more indepth investigation, than done previously, of the effects of the Bradshaw constant on the solution about an airfoil were analyzed.

As the Bradshaw constant is increased, the flow field and the flow coefficients are affected. The flow field in the rear stagnation region develops from a flow without any vortices to a flow with a primary and secondary vortex as the Bradshaw constant is increased. This twin vortex flow field, obtained at higher values of the Bradshaw constant, is in close agreement with experimental results. Once a high enough value is reached for the Bradshaw constant, the flow coefficients are relatively unaffected by any further increase in the curvature correction. For higher blowing coefficients, these same trends are observed.

When the jet ratios or jet momentum were matched with experimental results, the moment coefficient provided good results. However, the lift and drag values were not in agreement with experimental results. As the accuracy of the lift and drag values was increased, the accuracy of the moment coefficient was degraded.

This report provides further insight into the effects of the Bradshaw-modified Baldwin-Lomax turbulence model. However, the results obtained indicate that a better turbulence model must be employed before CFD can be used to accurately predict the flow around a circulation control airfoil.

COMPUTATIONAL INVESTIGATION OF CIRCULATION CONTROL TURBULENCE MODELING

I. INTRODUCTION

How can we increase the airfoil's lift? What can be done to maximize the lift coefficient? Over the years, researchers have been continiously investigating these questions. Numerous concepts have been introduced to answer these questions. One concept generating a lot of interest in the last few years is the circulation control airfoil.

Circulation control augments an airfoil's lift by blowing a thin jet over a rounded trailing edge. By taking advantage of the Coanda effect, the jet delays separation, forces the stagnation point to the lower surface, and increases circulation around the airfoil.

The Coanda effect is the ability of a tangential jet to stay attached to a curved surface through large turning angles (6:53). The entrainment of the flow between the wall and the jet creates a low pressure region causing the jet to attach to the surface. The suction generated by the entrainment is sufficient to overcome the centrifugal forces, thus causing the jet to bend with the wall. The jet finally separates from the wall due to viscosity induced momentum losses (6:54).

The main difference between the circulation control airfoil and a conventional airfoil is the trailing edge configuration. Instead of a sharp trailing edge, the circulation control airfoil employs a rounded trailing edge. Thus, the Kutta condition, imposed on airfoils with sharp trailing edges, is not imposed on a circulation control airfoil (32:1). Instead, the location of the stagnation point is a function of the momentum of the jet and the freestream flow conditions. Thus, by varying the jet momentum the airfoil's lift can be varied (17:1). Figure 1 displays the geometry of a typical circulation control airfoil.

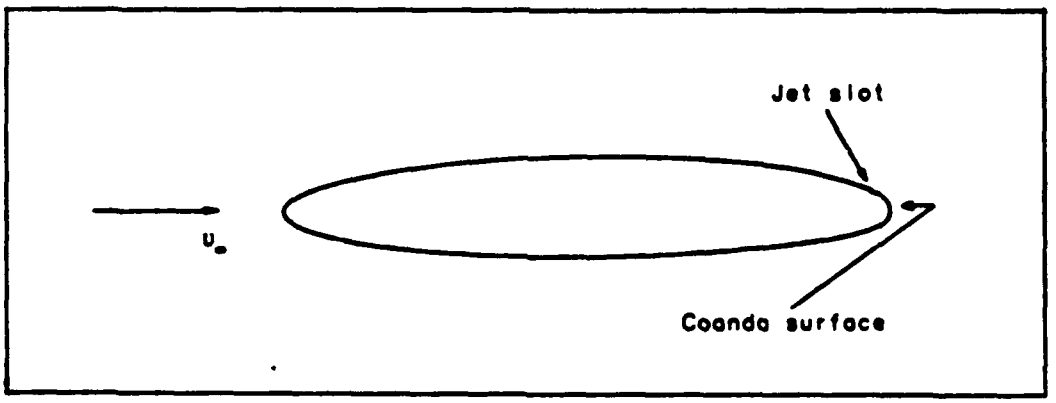

Figure 1. Circulation Control Airfoil Geometry

With this capability, a circulation control airfoil can obtain higher lift coefficients and lower aircraft stall speeds than conventional airfoils. This allows several benefits from reduced runway lengths to increased payload weights (32:1). However, the circulation control airfoil

experiences more drag than a typical airfoil. The rounded trailing edge creates a larger wake region than a sharp trailing edge airfoil. The wake region can be reduced by using a flap type system to create a sharp trailing edge when the additional lift is not needed. The added weight and complexity of pressurized ducts is another disadvantage of the circulation control airfoil concept (31:3).

The circulation control concept has many applications. Short takeoff and landing (STOL) aircraft can benefit by reducing forward speed while increasing lift. Circulation control airfoils have been investigated for application on the X-wing stopped rotor concept aircraft. The no-tail rotor (NOTAR) helicopter design uses circulation control to produce the anti-torque forces required for stable flight. These are just a few present applications of the circulation control airfoil concept (17:16).

1.1 Background

About 1910, Henry Coanda was trying to deflect the engine's exhaust away from his aircraft's wooden wings. Instead of deflecting the exhaust, the exhaust adhered to the deflection plates. This led to two important discoveries by Henry Coanda: 1) the "Coanda effect"; and 2) burning wings don't produce much lift (32:3).

Since then a tremendous amount of time has been spent on researching the circulation control airfoil concept. The National Gas Turbine Establishment in England started doing

extensive studies into the benefits of circulation control airfoils about 1960 (7). About the same time, V.E. Lockwood did some experimental work with a blowing slot(s) on a cylinder (15). Throughout the 1970s and up to present day, the David Taylor Naval Ship Research and Development Center (DTNSRDC) has compiled an extensive database on circulation control airfoils (9). In 1986, NASA held a circulation control workshop at Ames Research Center (18). This conference presented the latest developments in experimental and computational research and potential applications for circulation control airfoils. A good overview of the conference was compiled by Nielsen and Biggers (17).

As Nielsen and Biggers state, the computational codes "are promising, but as yet inadequate for a priori modeling of the Coanda flows." This inadequacy is due to the lack of an accurate model for the flow around the jet slot and the Coanda surface. How does the jet blowing interact with the freestream boundary layer? What complications does the rounded Coanda surface impose on the boundary layer? And, what type of corrections must be implemented to account for these effects? Even though researchers have been able to get good results, they agree that these questions must be answered before the computational algorithms can be used to predict circulation control performance.

Pulliam et al (20) used the thin-layer Navier-Stokes equations in generalized coordinates to compute the flow around a circulation control airfoil. They used an implicit

approximate factorization technique with the zero equation Baldwin-Lomax turbulence model to solve the governing equations. In addition, Pulliam et al used a correction to the Baldwin-Lomax model suggested by Baldwin to account for the curvature effects of the rounded trailing edge. A spiral grid was used to compute, instead of model, the flow at the slot exit. Even though the results were comparable to experimental results, the curvature correction had to be adjusted to "match" the computational results with the experimental results. As long as this "matching" process is required, the code can not be used to predict the performance of circulation control airfoils.

To account for the effects of curvature, Shrewsbury (26) and Williams (31) modified the Baldwin-Lomax turbulence model with an empirical curvature correction factor put forth by Bradshaw (6:68-71). Both researchers used this modified turbulence model in conjunction with Beam-Warming related algorithms to model the flow around a circulation control airfoil. Again, both researchers obtained reasonable results, but only after adjusting the curvature correction to "match" the computational results with the experimental results.

As Nielsen and Biggers stated, these computational codes do have promise. The Navier-Stokes solvers used by Pulliam, Shrewsbury, and Williams do provide reasonable results. However, the trial and error process associated with "matching" the computational results with the

experimental results through the varying of the empirical turbulence corrections must be eliminated. If computational methods are to be used in the research and design of circulation control airfoils, an approach must be developed that does not require "matching". Two courses of action are needed to eliminate this trial and error process:
1) experimental efforts need to concentrate on analyzing all the aspects, especially the turbulent makeup, of the complex flow field caused by the jet and Coanda surface;
2) computational programmers need to develop a broader knowledge about the effects of the turbulence correction factors. With this increased knowledge, the need to "match" computational results with experimental results may be eliminated. Thus, the computational codes can then be used to predict the performance of circulation control airfoils.

1.2 Objective

The purpose of this study is to further the efforts associated with the second course of action described above. Instead of validating the capability of the code to model a circulation control airfoil, as has been done previously, this research examines the correlation between the computational results and the Bradshaw curvature correction. Using the Beam-Warming algorithm and modified Baldwin-Lomax turbulence model employed by Williams, a systematic approach to the use of the curvature correction factor is examined. Instead of just "matching" computational results with

experimental results, this study will investigate the effect of the Bradshaw curvature correction on the computed flow field. In addition to examining the variation in the coefficients, how does the actual flow field change as the Bradshaw correction is increased? Can any trends in the effect of the Bradshaw correction be revealed that will allow the computational codes to be used to predict circulation control flow fields? To generalize this correlation for a variety of flow geometries, the algorithm is applied to the "simple" geometry of a two-dimensional circular cylinder. The effect of the Bradshaw correction on the flow field about the circular cylinder will then be compared to the effect of the Bradshaw correction on the flow field about the airfoil. By comparing the trends for both flow fields, an assessment of the curvature corrections effect for various flow geometries can be ascertained.

II. ANALYSIS

The complex nature of the flow around a circulation control airfoil requires the use of the Navier-Stokes equations. As a group, the Navier-Stokes equations comprise the conservation of mass (continuity), conservation of momentum (Newton's second law), and conservation of energy (first law of thermodynamics). The following subsection will present the derivation of the strong conservation vector form of the Navier-Stokes governing equations. The remaining subsections discuss the numerical implementation of the Navier-Stokes equations, the application of the boundary conditions, the modifications made to the Baldwin-Lomax turbulence model, and the generation of the grids.

2.1 Governing Equations

For unsteady, compressible, viscous flows the governing equations are (19:11)

Conservation of Mass -

$$\frac{\partial \rho}{\partial t} + \vec{\nabla} \cdot (\rho \vec{V}) = 0 \tag{1}$$

Conservation of Momentum -

$$\frac{\partial (\rho \vec{V})}{\partial t} + \vec{\nabla} \cdot (\rho \vec{V} \vec{V}) = \rho \vec{f} + \vec{\nabla} \cdot \underline{\sigma} \tag{2}$$

Conservation of Energy -

$$\frac{\partial E_t}{\partial t} + \vec{\nabla} \cdot E_t \vec{V} = \frac{\partial Q}{\partial t} + \rho \vec{f} \cdot \vec{V} + \vec{\nabla} \cdot (\underline{\sigma} \cdot \vec{V}) - \vec{\nabla} \cdot \vec{q} \qquad (3)$$

The total energy, E_t, is expressed as

$$E_t = \rho \left(e + \frac{1}{2} \vec{V}^2 \right) \qquad (4)$$

For the case of a Newtonian fluid the stress tensor, $\underline{\sigma}$, is

$$\underline{\sigma} = -pI + \underline{\tau} \qquad (5)$$

where the viscous stress terms are defined as

$$\tau_{ij} = -p\delta_{ij} + \mu \left(\frac{\partial u_i}{\partial x_j} + \frac{\partial u_j}{\partial x_j} \right) + \delta_{ij} \lambda \frac{\partial u_k}{\partial x_k} \qquad (6)$$

The viscosity functions are calculated using Stokes' hypothesis (23:60)

$$\lambda = -\frac{2}{3} \mu \qquad (7)$$

and Sutherland's formula (23:328)

$$\mu = C_1 \frac{T^{3/2}}{T + C_2} \qquad (8)$$

Closure of the Navier-Stokes equations is provided by the perfect gas law

$$p = \rho RT = \rho e (\gamma - 1) \qquad (9)$$

and Fourier's law of heat conduction

$$\vec{q} = -k\vec{\nabla}T \tag{10}$$

With the approximation of constant Prandtl number, Pr, the coefficient of thermal conductivity, k, is

$$k = \frac{c_p}{Pr}\mu \tag{11}$$

For a two-dimensional rectilinear system, the Navier-Stokes equations become (16:5)

Conservation of Mass -

$$\frac{\partial \rho}{\partial t} + \frac{\partial(\rho u)}{\partial x} + \frac{\partial(\rho v)}{\partial y} = 0 \tag{12}$$

Conservation of Momentum -

$$\frac{\partial(\rho u)}{\partial t} + \frac{\partial(\rho u^2 + p - \tau_{xx})}{\partial x} + \frac{\partial(\rho uv - \tau_{xy})}{\partial y} = 0 \tag{13}$$

$$\frac{\partial(\rho v)}{\partial t} + \frac{\partial(\rho uv - \tau_{xy})}{\partial x} + \frac{\partial(\rho v^2 + p - \tau_{yy})}{\partial y} = 0 \tag{14}$$

Conservation of Energy -

$$\frac{\partial E_t}{\partial t} + \frac{\partial(E_t u + pu - u\tau_{xx} - v\tau_{yx} + q_x)}{\partial x} + \frac{\partial(E_t v + pv - u\tau_{xy} - v\tau_{yy} + q_y)}{\partial y} = 0 \tag{15}$$

Note, the body forces are assumed negligible and the heat generation term is assumed constant with respect to time.

To facilitate the application of these equations to a general curvilinear coordinate system, the physical domain (x,y) must be transformed to the computational domain (ξ,η). The transformation relating the physical and computational domain is

$$\begin{aligned} \xi &= \xi(x,y) \\ \eta &= \eta(x,y) \end{aligned} \tag{16}$$

Through application of the chain rule, the physical domain derivatives become

$$\frac{\partial(\ )}{\partial x} = \frac{\partial \xi}{\partial x}\frac{\partial(\ )}{\partial \xi} + \frac{\partial \eta}{\partial x}\frac{\partial(\ )}{\partial \eta} \tag{17}$$

$$\frac{\partial(\ )}{\partial y} = \frac{\partial \xi}{\partial y}\frac{\partial(\ )}{\partial \xi} + \frac{\partial \eta}{\partial y}\frac{\partial(\ )}{\partial \eta} \tag{18}$$

After applying the chain rule and non-dimensionalizing (see Appendix A), the Navier-Stokes equations in matrix form for a general curvilinear coordinate system are

$$\frac{\partial U}{\partial t} + \xi_x \frac{\partial F}{\partial \xi} + \xi_y \frac{\partial G}{\partial \xi} + \eta_x \frac{\partial F}{\partial \eta} + \eta_y \frac{\partial G}{\partial \eta} = 0 \tag{19}$$

where

$$U = \begin{pmatrix} \rho \\ \rho u \\ \rho v \\ E_t \end{pmatrix} \tag{20}$$

$$F=\begin{pmatrix} \rho u \\ \rho u^2-\tau_{xx} \\ \rho uv-\tau_{xy} \\ (E_t+p)\,u-u\tau_{xx}-v\tau_{xy}-q_x \end{pmatrix} \tag{21}$$

$$G=\begin{pmatrix} \rho v \\ \rho uv-\tau_{xy} \\ \rho v^2-\tau_{yy} \\ (E_t+p)\,v-u\tau_{xy}-v\tau_{yy}-q_y \end{pmatrix} \tag{22}$$

The first equation is the conservation of mass; the center equations are the x and y momentum equations respectively and the final equation is the conservation of energy.

The turbulence is included through the turbulent eddy viscosity, ϵ, and the turbulent coefficient of thermal conductivity, k_t. With the inclusion of the turbulence, Stokes' hypothesis becomes

$$\lambda_t=-\frac{2}{3}(\mu+\epsilon) \tag{23}$$

and the turbulent coefficient of thermal conductivity is obtained by defining the turbulent Prandtl number, Pr_t,

$$k_t=c_p\frac{\epsilon}{Pr_t} \tag{24}$$

Sutherland's formula, Eq (8), is used to calculate the molecular viscosity, μ; the turbulent eddy viscosity is calculated with the turbulence model (sec 2.4); the

turbulent Prandtl number is assumed constant. With these definitions, the viscous stress and heat conduction terms become (3:86)

$$\tau_{xx} = -3\lambda_t u_x + \lambda_t (u_x + v_y) \tag{25}$$

$$\tau_{xy} = -\frac{3}{2}\lambda_t (u_y + v_x) \tag{26}$$

$$\tau_{yy} = -3\lambda_t v_y + \lambda_t (u_x + v_y) \tag{27}$$

$$q_x = -(k + k_t)\frac{\partial T}{\partial x} \tag{28}$$

$$q_y = -(k + k_t)\frac{\partial T}{\partial y} \tag{29}$$

Using the definition of the transformation Jacobian, J,

$$J = \frac{\partial(\xi, \eta)}{\partial(x, y)} = \xi_x \eta_y - \xi_y \eta_x \tag{30}$$

the Navier-Stokes equations are rewritten in strong conservation form (29:7)

$$\frac{\partial \tilde{U}}{\partial t} + \frac{\partial \tilde{F}}{\partial \xi} + \frac{\partial \tilde{G}}{\partial \eta} = 0 \tag{31}$$

where

$$\tilde{U} = \frac{1}{J} U \tag{32}$$

$$\tilde{F} = \frac{1}{J}(\xi_x F + \xi_y G) \tag{33}$$

$$\tilde{G} = \frac{1}{J}(\eta_x F + \eta_y G) \tag{34}$$

By separating the viscous and non-viscous terms, Eq 31 is rewritten as

$$\frac{\partial \tilde{U}}{\partial t} + \frac{\partial \tilde{F}_1}{\partial \xi} + \frac{\partial \tilde{G}_1}{\partial \eta} = \frac{\partial V}{\partial \xi} + \frac{\partial W}{\partial \eta} \tag{35}$$

This revision separates the functional relationships since

$$\tilde{F}_1 = f(\tilde{U}) \quad and \quad \tilde{G}_1 = f(\tilde{U}) \tag{36}$$

but

$$V = f(\tilde{U}, \tilde{U}_\xi, \tilde{U}_\eta) \quad and \quad W = f(\tilde{U}, \tilde{U}_\xi, \tilde{U}_\eta) \tag{37}$$

A further refinement separates the derivative relationships

$$\frac{\partial \tilde{U}}{\partial t} + \frac{\partial \tilde{F}_1(\tilde{U})}{\partial \xi} + \frac{\partial \tilde{G}_1(\tilde{U})}{\partial \eta} = \frac{\partial V_1(\tilde{U}, \tilde{U}_\xi)}{\partial \xi} + \frac{\partial V_2(\tilde{U}, \tilde{U}_\eta)}{\partial \xi} + \frac{\partial W_1(\tilde{U}, \tilde{U}_\xi)}{\partial \eta} + \frac{\partial W_2(\tilde{U}, \tilde{U}_\eta)}{\partial \eta} \tag{38}$$

Note $V=V_1+V_2$ and $W=W_1+W_2$. By substituting Eqs (25)-(27) in for the shear stresses and using Stokes' hypothesis, Eq (23), the matrices become

$$\tilde{U} = \frac{1}{J}\begin{pmatrix} \rho \\ \rho u \\ \rho v \\ E_t \end{pmatrix} \tag{39}$$

$$\tilde{F}_1 = \frac{1}{J}\begin{pmatrix} \rho u_c \\ \rho u u_c + \xi_x p \\ \rho v u_c + \xi_y p \\ (E_t + p)\, u_c \end{pmatrix} \tag{40}$$

$$\tilde{G}_1 = \frac{1}{J}\begin{pmatrix} \rho v_c \\ \rho u v_c + \eta_x p \\ \rho v v_c + \eta_y p \\ (E_t + p)\, v_c \end{pmatrix} \tag{41}$$

$$V_1 = \frac{1}{J}\begin{pmatrix} 0 \\ b_1 u_\xi + b_2 v_\xi \\ b_2 u_\xi + b_3 v_\xi \\ b_1 u u_\xi + b_2 (v u_\xi + u v_\xi) + b_3 v v_\xi + b_4 T_\xi \end{pmatrix} \tag{42}$$

$$V_2 = \frac{1}{J}\begin{pmatrix} 0 \\ c_1 u_\eta + c_2 v_\eta \\ c_3 u_\eta + c_4 v_\eta \\ c_1 u u_\eta + c_2 u v_\eta + c_3 v u_\eta + c_4 v v_\eta + c_5 T_\eta \end{pmatrix} \tag{43}$$

$$W_1 = \frac{1}{J}\begin{pmatrix} 0 \\ c_1 u_\xi + c_3 v_\xi \\ c_2 u_\xi + c_4 v_\xi \\ c_1 u u_\xi + c_2 v u_\xi + c_3 u v_\xi + c_4 v v_\xi + c_5 T_\xi \end{pmatrix} \tag{44}$$

$$W_2 = \frac{1}{J}\begin{pmatrix} 0 \\ d_1 u_\eta + d_2 v_\eta \\ d_2 u_\eta + d_3 v_\eta \\ d_1 u u_\eta + d_2 (v u_\eta + u v_\eta) + d_3 v v_\eta + d_4 T_\eta \end{pmatrix} \tag{45}$$

where the contravariant velocities are

$$u_c = \xi_x u + \xi_y v \tag{46}$$

$$v_c = \eta_x u + \eta_y v \tag{47}$$

and the viscous coefficients are

$$b_1 = (\mu+\varepsilon)\left(\frac{4}{3}\xi_x^2+\xi_y^2\right) \tag{48}$$

$$b_2 = \frac{1}{3}(\mu+\varepsilon)\xi_x\xi_y \tag{49}$$

$$b_3 = (\mu+\varepsilon)\left(\xi_x^2+\frac{4}{3}\xi_y^2\right) \tag{50}$$

$$b_4 = c_p\left(\frac{\mu}{Pr}+\frac{\varepsilon}{Pr_t}\right)\left(\xi_x^2+\xi_y^2\right) \tag{51}$$

$$c_1 = -(\mu+\varepsilon)\left(\frac{4}{3}\xi_x\eta_x+\xi_y\eta_y\right) \tag{52}$$

$$c_2 = -(\mu+\varepsilon)\left(\frac{2}{3}\xi_x\eta_y-\xi_y\eta_x\right) \tag{53}$$

$$c_3 = (\mu + \varepsilon)\,(\xi_x \eta_y - \frac{2}{3}\xi_y \eta_x) \tag{54}$$

$$c_4 = -(\mu + \varepsilon)\,(\xi_x \eta_x + \frac{4}{3}\xi_y \eta_y) \tag{55}$$

$$c_5 = -c_p\left(\frac{\mu}{Pr} + \frac{\varepsilon}{Pr_t}\right)(\xi_x \eta_x + \xi_y \eta_y) \tag{56}$$

$$d_1 = (\mu+\varepsilon)\,(\frac{4}{3}\eta_x^2 + \eta_y^2) \tag{57}$$

$$d_2 = \frac{1}{3}(\mu+\varepsilon)\,\eta_x \eta_y \tag{58}$$

$$d_3 = (\mu+\varepsilon)\,(\eta_x^2 + \frac{4}{3}\eta_y^2) \tag{59}$$

$$d_4 = c_p\left(\frac{\mu}{Pr} + \frac{\varepsilon}{Pr_t}\right)(\eta_x^2 + \eta_y^2) \tag{60}$$

2.2 Numerical Implementation

The numerical technique used to solve the Navier-Stokes equations is based on the Beam and Warming approximate factorization algorithm (5,30) with a Baldwin-Lomax Turbulence Model (4). The code was developed by Dr. Miguel R. Visbal of the Air Force Wright Aeronautical Laboratories (28,29). Steve Williams added some modifications to the code to adapt it to circulation control airfoils (31).

The algorithm solves the strong conservation form of the Navier-Stokes equations (Eq 38). The solution algorithm for first order Euler time differencing is written as

$$[I+\Delta t(\frac{\partial A^n}{\partial \xi}-\frac{\partial^2 R^n}{\partial \xi^2})][I+\Delta t(\frac{\partial B^n}{\partial \eta}-\frac{\partial^2 S^n}{\partial \eta^2})]\Delta \tilde{U}^n=$$
$$-\Delta t[\frac{\partial}{\partial \xi}(\tilde{F}_1-V_1-V_2)^n+\frac{\partial}{\partial \eta}(\tilde{G}_1-W_1-W_2)^n] \quad (61)$$

The Jacobian matrices A, B, R, and S are (see Appendix B)

$$A=\frac{\partial \tilde{F}_1}{\partial \tilde{U}} \qquad B=\frac{\partial \tilde{G}_1}{\partial \tilde{U}} \quad (62)$$

$$R=\frac{\partial V_1}{\partial \tilde{U}_\xi} \qquad S=\frac{\partial W_2}{\partial \tilde{U}_\eta} \quad (63)$$

and n is the temporal index. The equation is solved in three steps:

1) along lines of constant η

$$[\vec{I}+\Delta t(\frac{\partial A^n}{\partial \xi}-\frac{\partial^2 R^n}{\partial \xi^2}]D^n=$$
$$-\Delta t[\frac{\partial}{\partial \xi}(\tilde{F}_1-V_1-V_2)^n+\frac{\partial}{\partial \eta}(\tilde{G}_1-W_1-W_2)^n] \quad (64)$$

2) along lines of constant ξ

$$[I+\Delta t(\frac{\partial B^n}{\partial \eta}-\frac{\partial^2 S^n}{\partial \eta^2})]\Delta \tilde{U}^n=D^n \quad (65)$$

3) update solution

$$\tilde{U}^{n+1}=\tilde{U}^n+\Delta \tilde{U}^n \quad (66)$$

The spatial derivatives are computed using second order central differences. This setup requires the solution of a block tridiagonal system for steps 1) and 2) along each coordinate line, where each block has dimensions 4x4.

To damp any numerical instabilities, artificial viscosity terms are added to the algorithm. An explicit fourth order term is added to the right-hand side of Eq (61)

$$D_e = -\frac{1}{J}\omega_e \Delta t (\delta^4_\xi + \delta^4_\eta) U^n \tag{67}$$

In addition, second order implicit damping terms are added to enhance stability. The implicit terms are inserted within the applicable operators on the left-hand side of Eq (61)

$$D_\xi = -\frac{1}{J}\omega_i \Delta t \, \delta^2_\xi \, JI \tag{68}$$

$$D_\eta = -\frac{1}{J}\omega_i \Delta t \, \delta^2_\eta \, JI \tag{69}$$

The δ operators are central difference operators in the respective directions and of the respective order.

Local time stepping is introduced to accelerate convergence to a steady state solution. The time step is computed by

$$\Delta t = C \Delta t_{max} \tag{70}$$

where C is the Courant number. Appendix C contains a list and description of the required program inputs.

Convergence of the code was determined by monitoring the oscillations of the lift and drag coefficients. A solution was assumed valid when the amplitude of the

oscillations was less than 0.1 percent for both the lift and drag coefficients. The convergence criteria was modified for the cylinder geometry at high Reynolds numbers since a steady-state solution was not expected due to the presence of vortex shedding. The convergence criteria for the cylinder at high Reynolds numbers was to allow only a one percent scatter about a periodic/quasi-periodic pattern.

2.3 Boundary Conditions

Boundary conditions must be specified at the grid exterior boundary, the grid cut line, the airfoil surface, and the jet slot. The exterior boundary of the grid is divided into an inflow and outflow portion. Typical freestream conditions are used along the inflow

$$u = U_\infty \cos(\alpha) \tag{71}$$

$$v = U_\infty \sin(\alpha) \tag{72}$$

$$p = p_\infty \tag{73}$$

$$\rho = \rho_\infty \tag{74}$$

Along the outflow, subsonic velocity is assumed with

$$\frac{\partial v}{\partial x} = 0 \tag{75}$$

$$\frac{\partial \rho}{\partial x} = 0 \tag{76}$$

$$p = p_\infty \tag{77}$$

$$\frac{\partial u}{\partial x} = 0 \tag{78}$$

The grid overlapped two points on both sides of the cut line. Along these overlapped lines periodic boundary conditions are enforced.

On the airfoil surface, except the jet slot, no-slip and adiabatic wall boundary conditions are imposed:

$$u = v = 0 \tag{79}$$

$$\frac{\partial p}{\partial n} = 0 \tag{80}$$

$$\frac{\partial T}{\partial n} = 0 \tag{81}$$

The jet slot is assumed convergent with total temperature and pressure constant across the exit. The flow out the slot is assumed to be isentropic. The pressure at the slot is extrapolated with the use of Eq (82)

$$\frac{\partial p}{\partial x} = 0 \tag{82}$$

Using the jet static pressure calculated from Eq (82) and the input variable of jet total pressure over freestream static pressure (see Appendix C), the ratio of jet static pressure to jet freestream pressure can be determined. Using the isentropic relationship,

$$\left(\frac{p_o}{p}\right)_{jet} = \left(1 + \frac{\gamma-1}{2} M_1^2\right)^{\frac{\gamma}{(\gamma-1)}} \tag{83}$$

the jet Mach number can be calculated. With the jet Mach number and the ratio of jet total temperature to freestream static temperature (input variable), the jet static temperature can be calculated with the isentropic relationship

$$\left(\frac{T_o}{T}\right)_{jet} = 1 + \frac{\gamma-1}{2} M_1^2 \tag{84}$$

With the jet Mach number and static temperature, the jet velocity components can be calculated

$$u = M(\gamma RT)^{1/2} \cos\phi \tag{85}$$

$$v = M(\gamma RT)^{1/2} \sin\phi \tag{86}$$

where ϕ is the angle of the jet midline with the coordinate axes. Note the flow at the exit is limited to sonic velocity due to chocking (31).

The input values of jet pressure and temperature ratio and the slot height dictate the jet momentum coefficient. The jet momentum coefficient is defined as (31:17)

$$C_\mu = \frac{\dot{m}_j V_j}{q_\infty c} \tag{87}$$

Note, the jet velocity is determined assuming isentropic expansion out the jet slot.

The drag calculation is modified due the presence of the jet thrust. The modified drag coefficient is calculated by subtracting the momentum coefficient from the friction and pressure drag (31:18)

$$C_d = C_{d_f} + C_{d_p} - C_\mu \tag{88}$$

2.4 Turbulence Model and Point of Transition

The accuracy of the computational solution for flow around a circulation control airfoil is heavily dependent on correctly predicting the point of boundary layer detachment from the Coanda surface. The turbulence model strongly influences the location of the separation point. Thus, without a valid turbulence model the computational solution is not accurate.

As discussed previously, the turbulence model most widely used for circulation control modeling is the Baldwin-Lomax model (4). This zero equation model is widely used due to its simplicity and versatility. But, this model requires modifications to handle the flow around the Coanda surface.

The rounded Coanda surface can have a surprisingly large effect on the turbulent boundary layer. Streamline curvature, caused by the Coanda surface, is a dominant source of additional strain rates in turbulent boundary layers. The extra rates of strain can have both a stabilizing and destabilizing effect on the flow. Balancing

the centrifugal and pressure forces on a fluid element results in a stabilizing effect in regions where the velocity increases normal to the surface, $\partial U/\partial n > 0$. In regions where the velocity decreases normal to the surface, $\partial U/\partial n < 0$, streamline curvature has a destabilizing effect on the flow. These instabilities can increase or decrease the turbulent transport of the flow. The streamline curvature of a flow field can be an order of magnitude more important to turbulent boundary layer development than the normal pressure gradient (6).

To account for this behavior, Bradshaw (6) recommends adjusting the mixing length. The Baldwin-Lomax model calculates the turbulent eddy viscosity of the inner layer

$$(\mu_t)_{inner} = \rho \omega l^2 \tag{89}$$

To account for the streamline curvature, the length is multiplied by a curvature correction factor, F,

$$F = 1 - \theta S \tag{90}$$

The parameter S represents the ratio of extra strain rates induced by the streamline curvature to the inherent strain rates

$$S = \frac{\frac{U}{r}}{\frac{\partial U}{\partial n}} \tag{91}$$

θ is an empirical curvature correction constant which varies from case to case but is of the order of ten.

Adverse pressure gradients normal to the flow have a big impact on boundary layer transition. Laminar flows can not withstand any appreciable adverse pressure gradients. The adverse pressure gradient tends to amplify any initial velocity oscillations, thus increasing the tendency to transition to fully turbulent flow. The appearance of the low frequency Tollmien-Schlichting waves in the laminar boundary layer is the first indication of boundary layer instability. As the velocity oscillations grow, the laminar boundary layer quickly degenerates into a fully turbulent boundary layer. Even though the phrase "point of transition" is used throughout the literature, the transformation from a laminar to a turbulent boundary layer occurs over a finite distance (23:445-500).

This study took a conservative approach towards specifying the transition from laminar to turbulent. Using the Pohlhausen method based on the elliptic airfoil's slenderness ratio (23:492-499), the point of instability was determined. Then the pressure field between the front stagnation point and the point of instability is examined. The minimum pressure point located in this region is then specified as the "point of transition". This criteria leads to an increase in calculated drag when compared to experimental results since the actual "point of transition" is downstream of the minimum pressure point and point of instability, in general (23:489-500).

2.5 Grid Generation

Due to the rounded trailing edge and variable separation point location, circulation control airfoils are not conducive to the use of C-grids. However, an O-grid conforms to the Coanda surface and the cut line does not have to be located in the wake region. For both the circular cylinder and the airfoil, O-grids were used with the cut line at the leading edge of the model. All grids were generated with GridGen-2D, a software package developed by General Dynamics for the Air Force.

Once the surface contour, cut line, and exterior boundary were defined, Vinikour stretching was used to cluster the grid points around the critical regions, i.e. jet slot and Coanda surface. The grid lines were generated using a Soni TFI algebraic solver with further refinement accomplished using an elliptic solver. GridGen-2D allows several variations on the type of elliptic solver. The grids used in this study were developed using Poisson's equation with a Sorenson weighting function and with orthogonality enforced at the surface. The grid around the entire airfoil is shown in Figure 2; Figure 3 is a closeup of the jet slot and Coanda surface.

A major headache in circulation control airfoil grid generation is the discontinuous surface geometry at the jet slot. The sharp corners dictate a high degree of grid skewness. In addition to the various techniques used with the GridGen-2D elliptic solver, a hyperbolic solver was

investigated to minimize the grid skewness (12). However, neither solver was able to drastically reduce the skewness, see Figure 4. The poor grid metrics caused by the skewness can have a degrading influence on the solution. A qualitative value for this degradation is unknown.

For the one inch diameter circular cylinder, the final grid had 207 points azimuthally and 151 points normal to the surface. To insure accurate modeling of the boundary layer, normal spacing at the wall was 0.00001 chords. The far-field boundary was circular with a diameter of 30 chords.

In order to compare answers with previous analysis, the 103RE (also known as the 103XW) airfoil used by Williams (31) was used for this study. However, the surrounding grid was modified slightly. The number of points around the airfoil was increased from 176 to 211 to provide better resolution over the Coanda surface. In comparison with the flow field around the cylinder, the streamlined flow around the airfoil reduces the threat of a reflected pressure wave. Therefore, the far-field diameter was reduced to 10 chords. Eighty points were distributed between the airfoil surface and the far-field boundary with an initial spacing at the wall of 0.000005 chords.

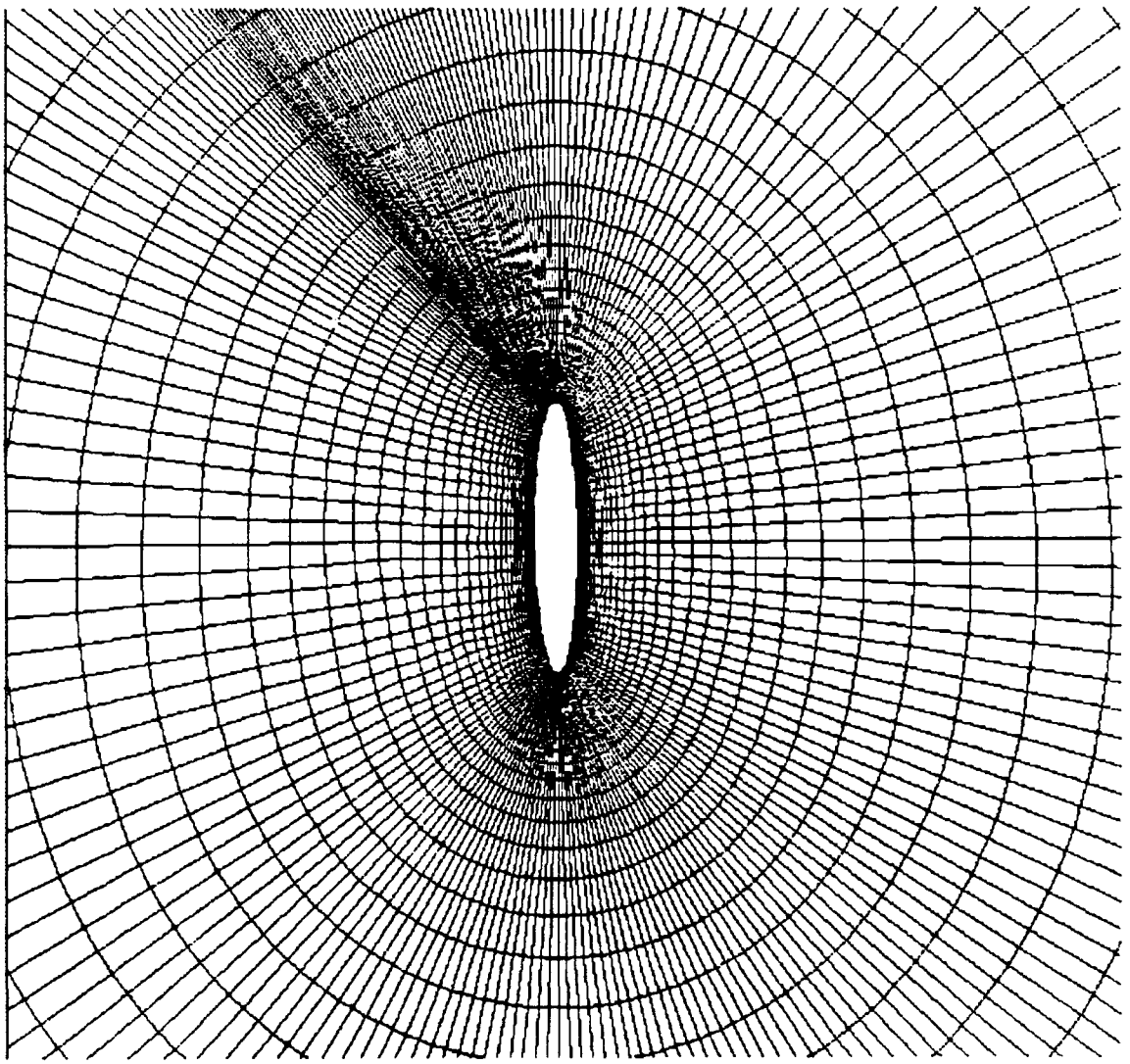

Figure 2. Inner Region of Airfoil Grid

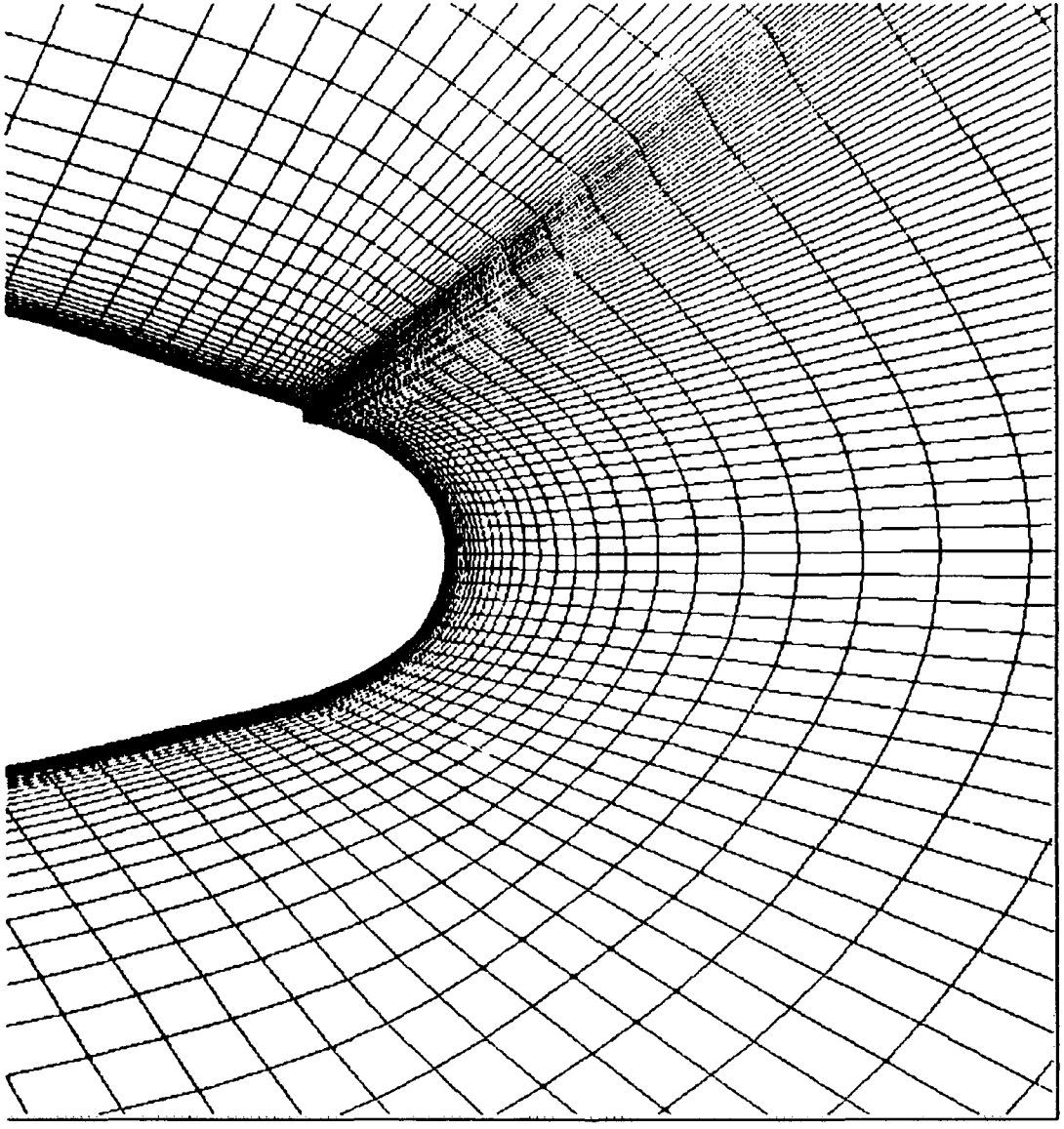

Figure 3. Jet Exit/Coanda Surface Region of Airfoil Grid

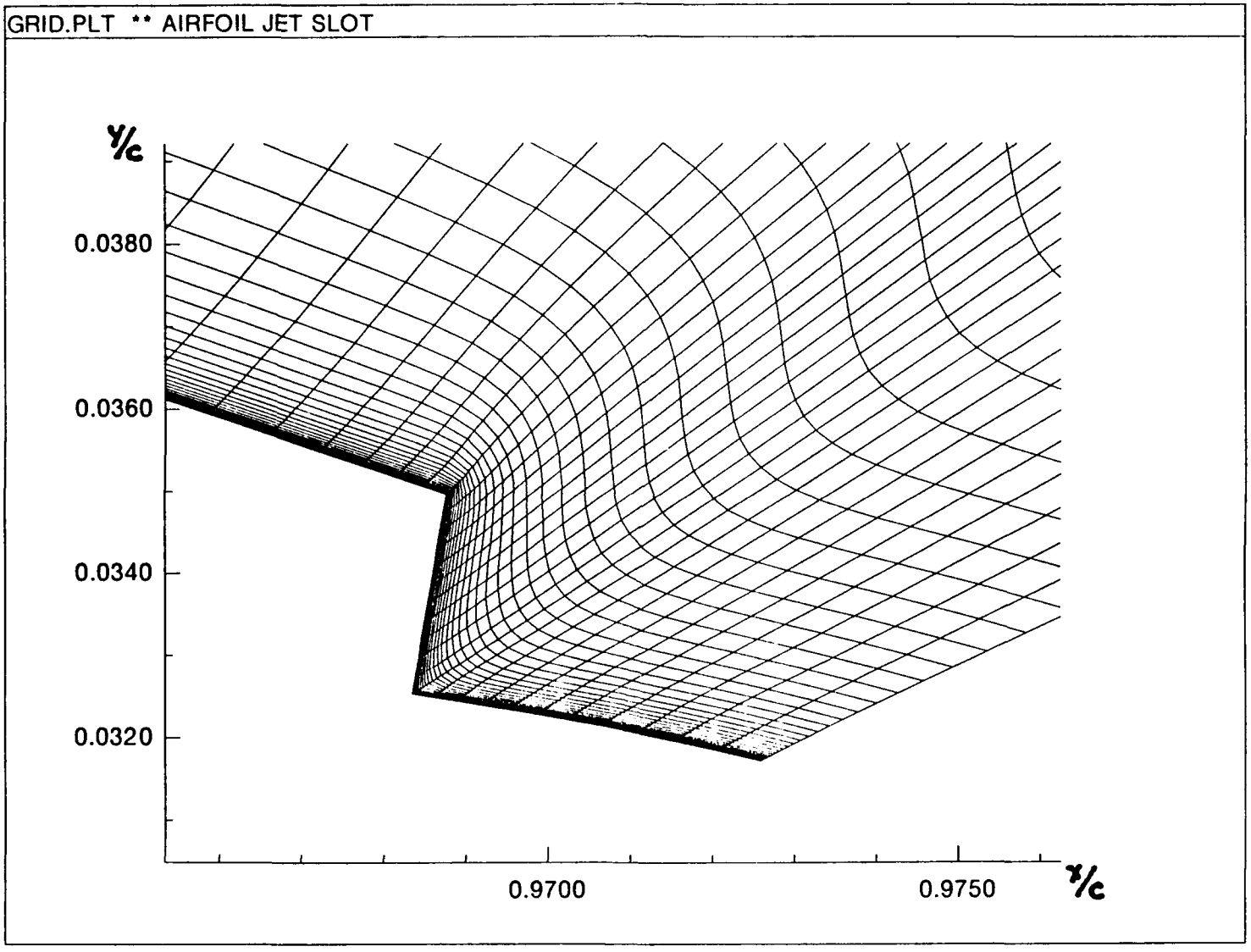

Figure 4. Jet Exit Region of Airfoil Grid

III. RESULTS AND DISCUSSION

To investigate the complexities of flow around a circulation control airfoil, two different geometries were analyzed - a circular cylinder, and an airfoil. The flow around both geometries was subjected to a Beam-Warming computational solution of the Navier Stokes equations. This chapter discusses the results obtained for both geometries. The first portion of the chapter discusses the results obtained with the circular cylinder. The results for the 103RE cross section experimental circulation control helicopter rotor follow the cylinder discussion.

3.1 Circular Cylinder

The flow around a circular cylinder is characteristic of flow past a "bluff body" (11:30). For a bluff body, the flow separates well ahead of the rear trailing edge, thus producing a large wake region. The exact location of the separation point and the nature of the flow in the wake region are highly dependent on the flow Reynolds number. Appendix D contains a breakdown of the flow regimes around a circular cylinder for a range of Reynolds numbers.

The multifarious nature of the flow around a circular cylinder requires a systematic analysis. The first step was to analyze the flow around a cylinder without a jet slot. Using a grid of 155 x 76, the code converged to a steady state solution for a Reynolds number of 40 with a freestream

Mach number of 0.2. A plot of the velocity vectors in the rear separated wake region is shown in Figure 5. The computed drag coefficient was 1.53, which is in good agreement with experimental values and computational results (28). This case served to validate the code for this Reynolds number regime and was used as a starting point for cases with jet slot blowing and higher Reynolds numbers. A slot was then added at the top of the cylinder, see Figure 6. The slot height was chosen as 0.01 to match a model currently being used at AFIT. Three fourths of the cylinder, from the rear horizontal plane clockwise to the top vertical plane, had a constant radius of 0.5. Due to the presence of the slot, the upper right quadrant of the cylinder had an increasing radius of curvature from 0.49 at the top to 0.5 at the rear trailing edge. A 155 x 155 grid was generated with clustering around and downstream of the slot exit.

The flow was computed for a Reynolds number of 40 and a Mach number of 0.2 without blowing. The presence of the slot discontinuity caused several disturbances in the flow field. Downstream of the slot several small vortices were apparent along with some alternating recirculation regions. In addition, the symmetric counter rotating vortices, characteristic of a cylinder without a slot, were no longer symmetric for the slotted cylinder. The vortices, along with the rear stagnation streamline, were skewed downward and the strength of the upper vortex increased while the

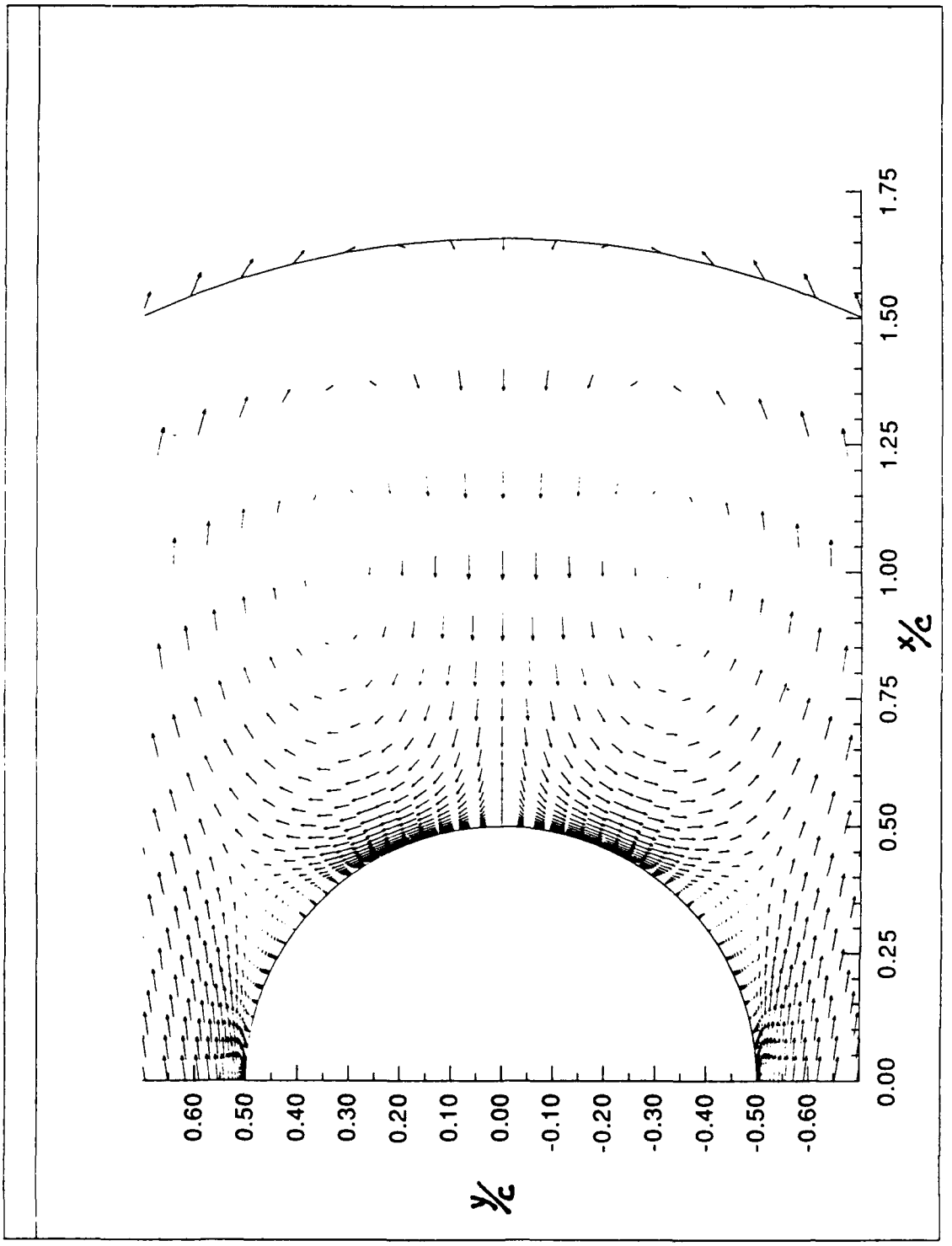

Figure 5. Velocity vectors, cylinder w/o slot, Re=40

strength of the lower vortex decreased. (Figures 8 and 9 show the same general trends observed for this converged Re=40 case). These disturbances resulted in an increase in the drag coefficient from 1.53 without the slot to 1.59 with the slot. The addition of the slot also caused an increase in the number of iterations required for convergence. Without the slot, the solution converged in approximately 900 iterations. With the slot, convergence was not achieved until approximately 2400 iterations. The initial condition used for both the slotted cylinder and the clean (unslotted) cylinder was a uniform flow field throughout the grid.

With a uniform flow field throughout, the code was run for several hundred iterations ($\approx$ 500) before the boundary conditions at the slot were changed to initiate blowing. The new boundary conditions corresponded to a momentum coefficient of approximately 0.01. Once the jet blowing was initiated the solution tended to diverge. Abnormal velocity vectors were being computed in the vicinity of the slot. A representative example of the flow field around the slot is diagramed in Figure 7. The next attempt allowed the non-blowing case to converge completely ($\approx$ 2500 iterations) before the boundary conditions were changed to initiate blowing. The same anomalous velocities were encountered near the slot.

With the converged, non-blowing case as an initial condition, the blowing was initiated at a lower momentum coefficient. By reducing the momentum coefficient, it was

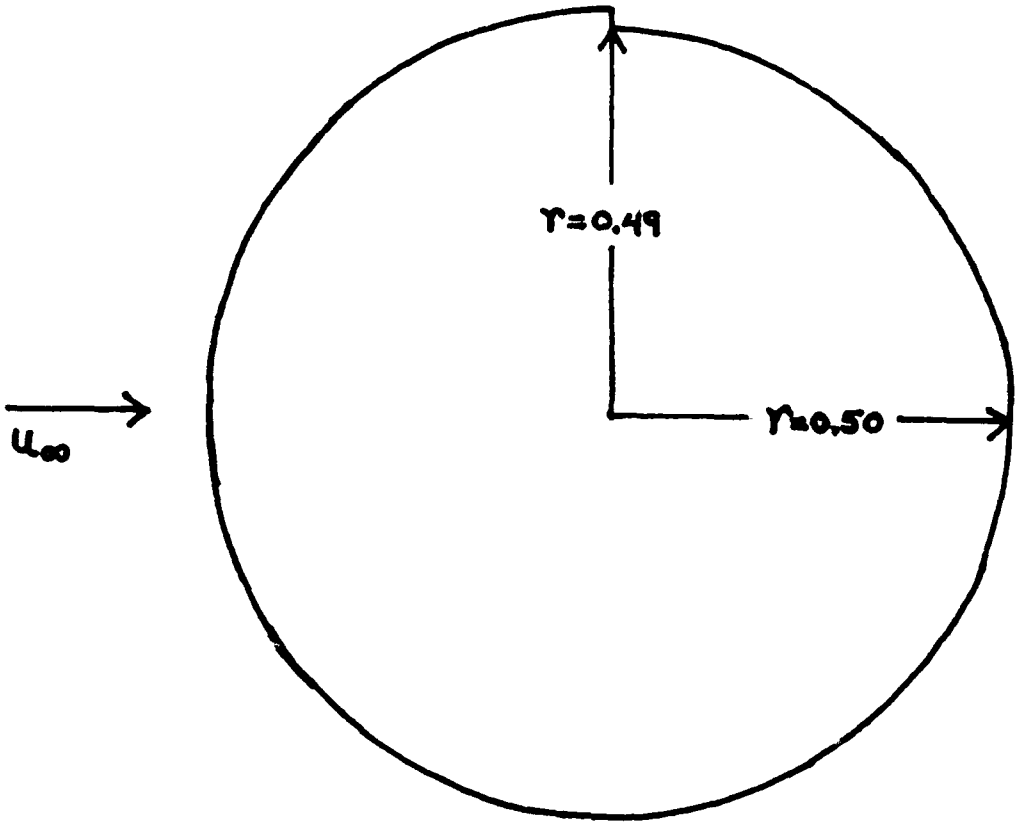

Figure 6. Slotted cylinder geometry

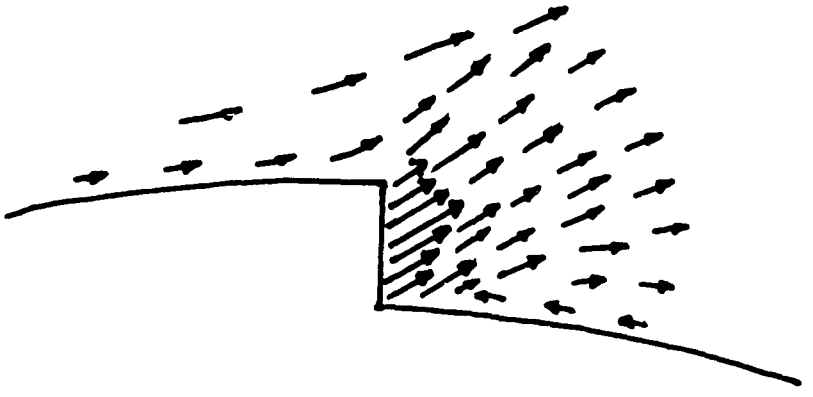

Figure 7. Abnormal velocities at slot exit, Re=40

hoped that the flow out the slot would not "overpower" the freestream flow, Re=40, M_∞=0.2. Again, the velocity vectors in the vicinity of the slot were similar to those presented in Figure 7.

In the hopes of solving the "overpowering" problem and to investigate more realistic conditions, the Reynolds number was increased. Even though the low Reynolds number regimes are not practical, they were to be compared with potential flow theory and theoretical procedures developed for jet blowing (8,27). By increasing the Reynolds number, comparisons with experimental data can be made (8,14,15) as well as comparisons with potential flow theory and theoretical models. However, increasing the Reynolds number introduces many complications. In the subcritical to upper transition regimes, see Appendix D, many things happen to the flow, from the disappearance of a regular Karmen vortex street to phenomenon associated with boundary layer transition. A Reynolds number of 3×10^6 was chosen for a variety of reasons: to avoid the boundary layer instabilities (i.e. separation bubbles) associated with the subcritical, critical, and supercritical regimes; to correspond to the Reynolds numbers used during wind tunnel testing of the airfoil (1); and to correspond to the anticipated wind tunnel testing of a cylinder at AFIT. These higher Reynolds numbers required the inclusion of the Baldwin-Lomax turbulence model. Based on experimental results (2:631), the boundary layer transition point was

specified as sixty-five degrees from the front stagnation point for both upper and lower surfaces. The blowing was not initiated because the non-blowing solution never "converged" to a steady-state or periodic/quasi-periodic state.

To stay away from instabilities caused by boundary layer transition, the transition point was specified as the front stagnation point. Again the solution never converged. The drag coefficient oscillated between 0.7 and 0.9, see Figure 8, without any defined period (the lift and moment coefficients were essentially constant at a value of zero). Figures 9 and 10 show the vortices and the recirculation immediately downstream of the slot; note, the slot is located between 0.49 and 0.50 on the vertical axis. The rear separated wake region is no longer characterized by symmetric recirculation vortices, see Figure 11.

A modification to the Baldwin-Lomax turbulence model was then included to limit the distance searched for maximum vorticity in the rear stagnation region. The boundary layer thickness calculated by the Baldwin-Lomax model on the front of the cylinder, before separation, was reviewed. Based on this thickness, a limit was imposed on the normal distance the Baldwin-Lomax model searched for the maximum vorticity (see Appendix C, input card 12). This modification did not create any major changes in the flow field results.

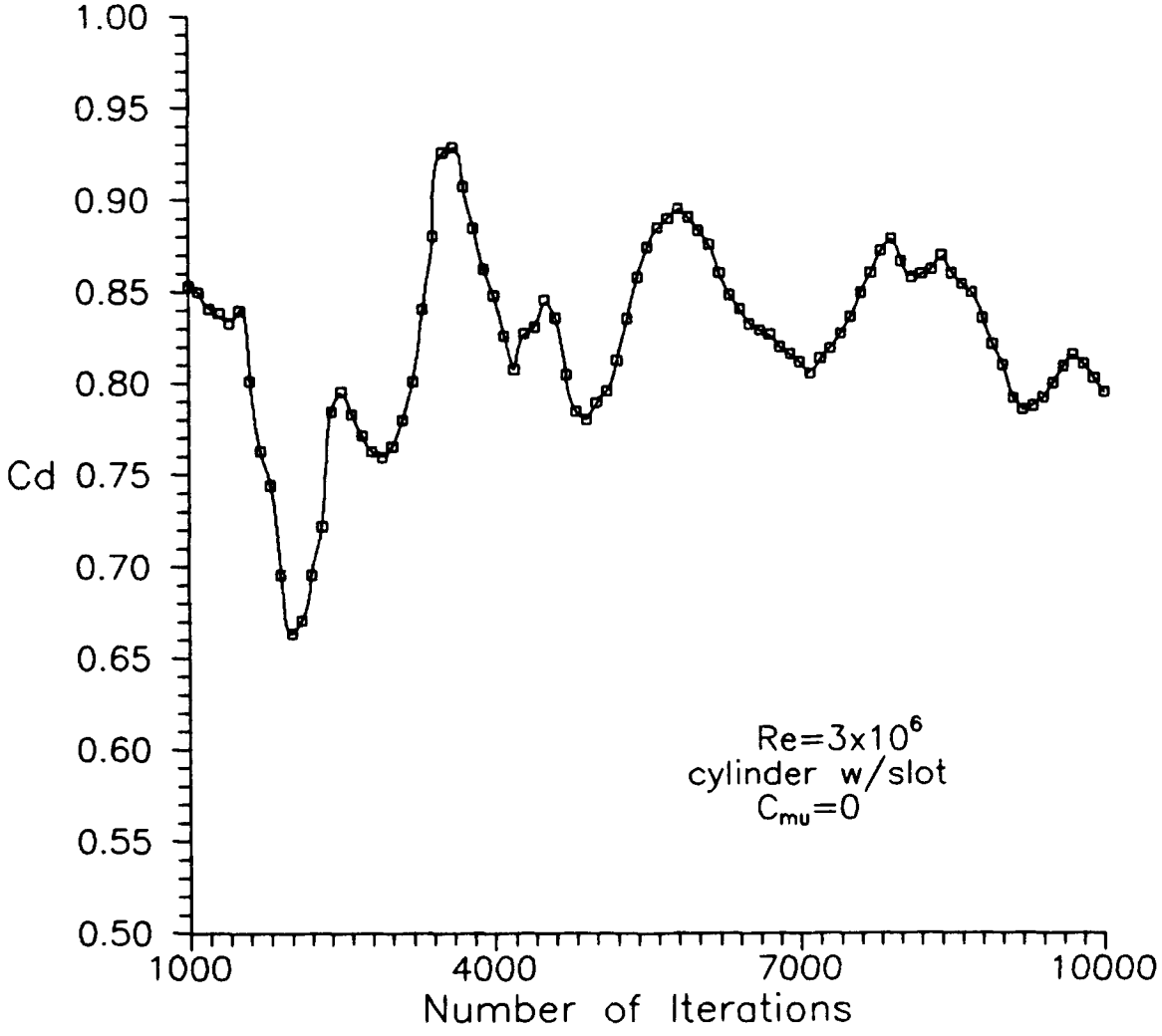

Figure 8. Cylinder Drag Oscillations

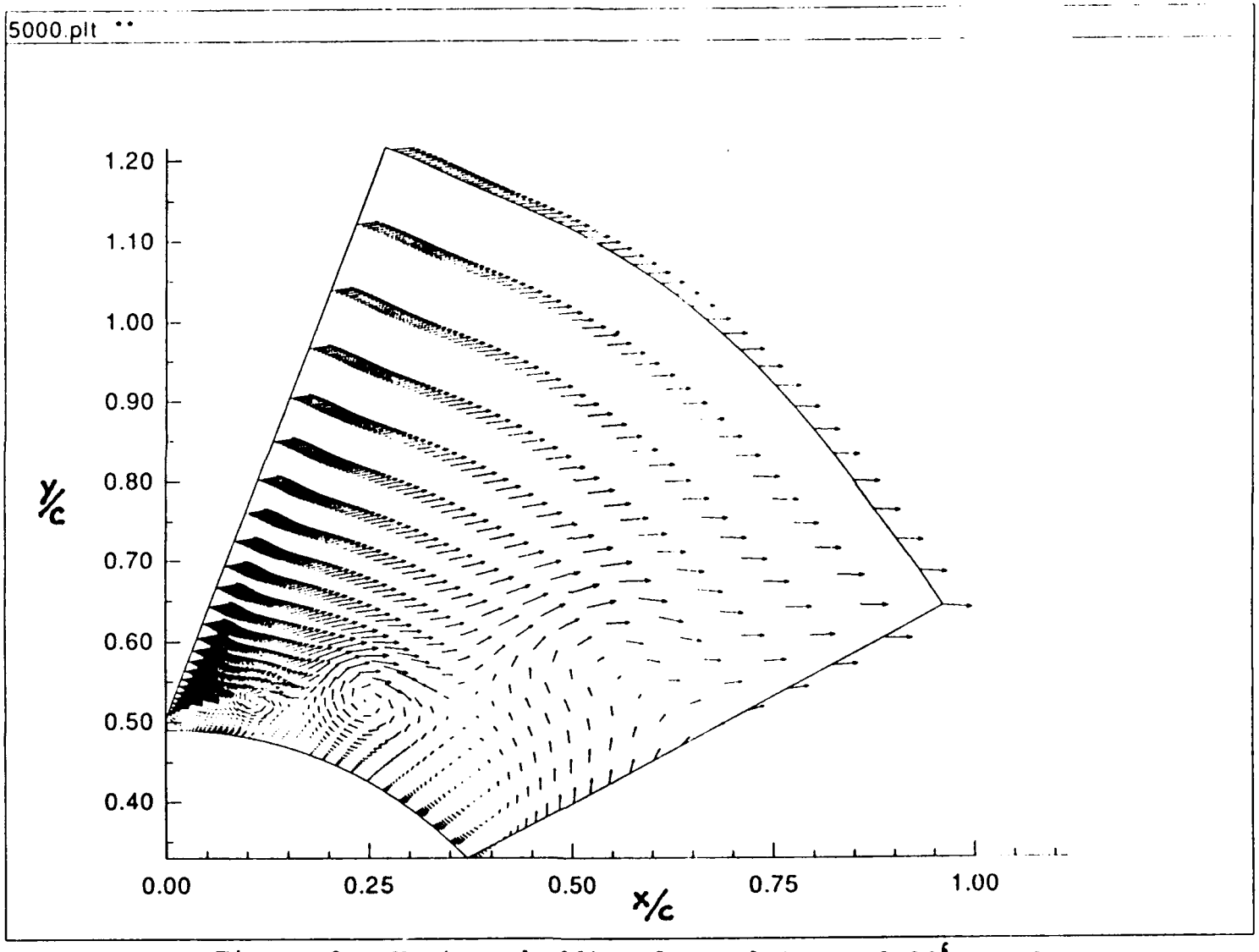

Figure 9. Vortex shedding from slot, Re=3x10^6, Cμ=0

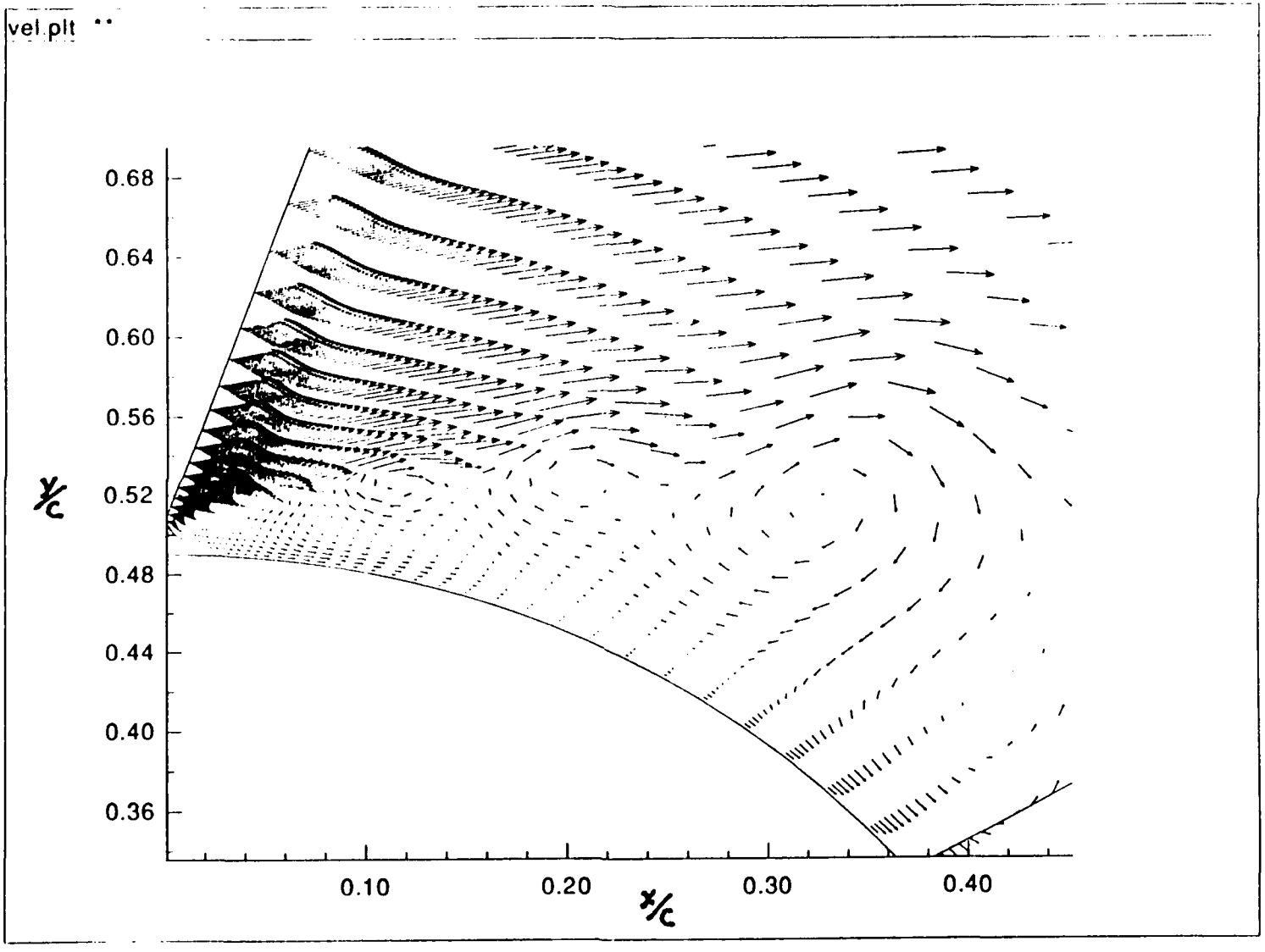

Figure 10. Vortex shedding from slot, Re=3x10^6, Cμ=0

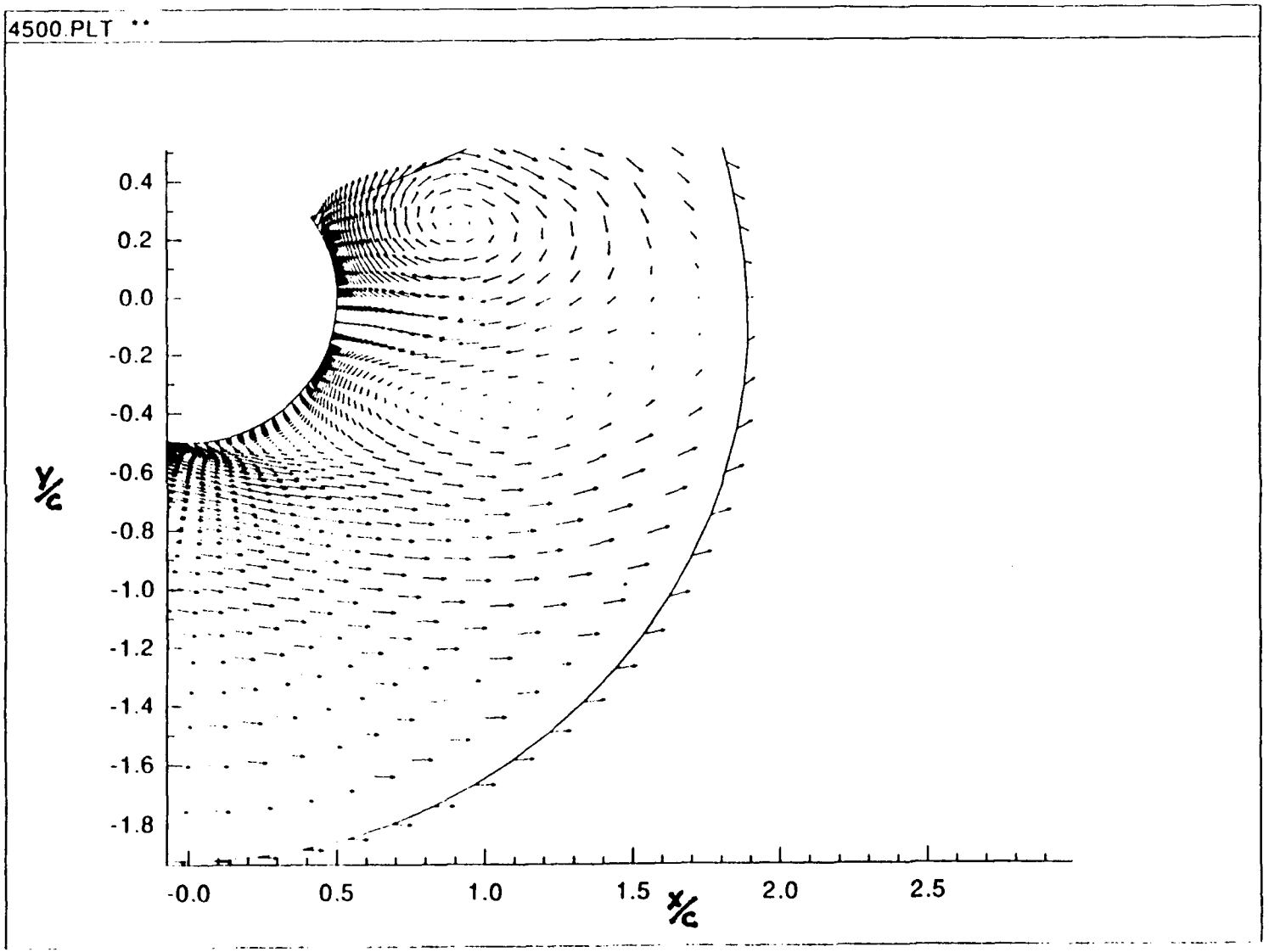

Figure 11. Velocity vectors, cylinder w/slot, Re=3x10^6, Cμ=0

To eliminate any additional perturbations, a new grid was developed for a cylinder without a slot. The same case was run, with a Reynolds number of 3×10^6 and the boundary layer transition point at the leading edge. The same basic results were obtained. The next step was to generate a new grid with more points in the boundary layer and a larger far-field radius (Δwall=.00001, far-field radius=20). Again this did not produce a "converged" solution.

A variety of factors may contribute to the lack of a steady converged solution - a) actual flow phenomena, b) turbulence model, and c) the grid.

a) Flow Phenomena

The Reynolds number examined corresponds to the upper transition regime (see Appendix D). For this regime, experimental tests show that the mean lift coefficient is slightly greater than zero (0.02 to 0.03) and the drag coefficient is increasing from approximately 0.2 to 0.5 (22). The computed lift values were approximately zero while the drag coefficient was a bit high at 0.8 to 0.9. However, the big factor is the lack of a definitive peak in the power spectra of the lift fluctuations, see Figure 39. Schewe (22) plots experimental results of the lift fluctuations versus the Strouhal number (a non-dimensional frequency) for a variety of Reynolds numbers. For the upper transition regime of Reynolds numbers, the Strouhal number is characterized by broadband low frequency values. This broad spectrum implies a lack of periodicy in the lift

fluctuations and the vortex shedding frequency. This could be responsible for the computational solutions' erratic behavior. Other computational investigations have cited this as a reason for the erratic drag oscillations (10).

b) Turbulence Model

To check the effect of the turbulence model, iterations were run without the turbulence model. Starting with a uniform flow field, the code was run for 100 iterations without the turbulence model. This was done to allow the uniform flow field to adapt to the cylinder geometry. At iteration 101, the Baldwin-Lomax turbulence model was turned on (with the limit on the search for maximum vorticity in the normal direction and without the Bradshaw curvature modification). After approximately 4000 iterations, the results were typical of previous runs. At this point, the turbulence model was turned off. After approximately 3000 more iterations, the results were reexamined. The values for the drag coefficient were not as erratic or as large in amplitude as the values obtained with the turbulence model. An examination of the parameters, i.e. F_{wake}, calculated in the turbulence model showed a rather abrupt change upon reaching the wake region.

Obviously, the zero equation Baldwin-Lomax turbulence model is not the best choice for use with a circular cylinder with large separated flow regions. Ideally, the Baldwin-Lomax model is most easily applied to a C-grid configuration, but the primary problem is the poor handling

of near wake regions containing separated flow. The circular cylinder precluded the use of a C-grid and amplified turbulence model instabilities due to the extensive separated wake region. Baldwin-Lomax models can not accurately model regions of recirculating flow. For recirculating flows, Launder and Spalding (13) show that a two equation, eddy-viscosity turbulence model (k-ε model) is better suited for these regions then a Baldwin-Lomax model.

c) Grid

For high Reynolds numbers, an extensive grid is required in the rear quadrant of the cylinder to properly model the flow. Without a lot of grid points imbedded in the boundary layer and near wake region, all of the flow idiosyncrasies can not be distinguished. In addition, the far-field location is critical to convergence. Without a significant far-field radius the wake will not be modeled correctly. Another major consequence of an inadequate far-field location is the reflection of pressure waves. With an insufficient far-field location, reflected pressure waves can corrupt the solution.

The final grid used for this case, 207 x 151, is believed to have been fine enough to resolve the above mentioned problems. The normal spacing at the surface was 0.00001 and the far-field boundary was circular with a diameter of 30 chords. The same results obtained with the previous grid were obtained with this expanded grid.

3.2 103RE Airfoil

As stated in the Introduction, the objective was to obtain correlations between the empirical curvature correction constant and the flow coefficients (C_l, C_d, and C_m) and flow field around a circular cylinder. These correlations were then to be compared to the curvature correction's effect on the flow coefficients and flow field around the airfoil. However, as previously covered, a "converged" solution for flow around the cylinder was not obtained. Instead, effects of the curvature correction on the flow around the streamlined airfoil were investigated.

In previous research, a range of values for the Bradshaw curvature correction have been used. Shrewsbury obtained "results more nearly in agreement" with a Bradshaw value of 25 (24). A Bradshaw value of 3.2 "matched" lift coefficient values but not drag and moment coefficient values for Williams (31). After varying the Bradshaw constant from 0 to 10, the value of 3.2 was chosen because the computed lift coefficient happened to coincide with the experimental lift coefficient at θ=3.2, for a single momentum coefficient. Since the drag and moment coefficients did not match at θ=3.2, does the computed flow field match experimental observations? Instead of just "matching" values, can a correlation between the Bradshaw curvature correction and the computed flow field be made? Using the same data points used by Williams, see Table 1, the Bradshaw constant was varied from 0 to 25 to monitor the effects of θ on the flow field.

Table 1. Computational and Experimental Test Conditions (31)

Pt	M_∞	Re $(1x10^6)$	α_{eff}	P_0/P_∞	T_0/T_∞	$C_\mu]_{exp}$
35	0.3	3.11	-0.92	1.137	0.956	.0094
36	0.3	3.09	-1.66	1.284	0.934	.0179

With a Bradshaw value of zero, Figures 12 and 13 show the flow field characteristics in the trailing edge region for data point 35. The Mach contours, Figure 12, show the freestream flow being entrained by the jet and separation occurring just prior to the trailing edge point. For this low of a blowing coefficient, $C_\mu]_{comp}$=0.0094, the separation point is not expected to reach the lower surface of the airfoil. Figure 13 shows a close-up of the velocity vectors in the separation region. The separation point and reverse flow due to the adverse pressure gradient are easily distinguishable. Note the absence of any vortex in the flow field.

As the Bradshaw value is increased, with the jet pressure and temperature ratios held constant, several important flow field changes occur. The separation point tends to move closer to the jet slot and two counterrotating vortices start to appear. In Figure 14, with a Bradshaw value of 4, the separation point has moved up to a y/c location of approximately 0.010 versus a location of 0.006 in Figure 13. In addition, two vortices have been formed in the separation region; an upper vortex with a clockwise

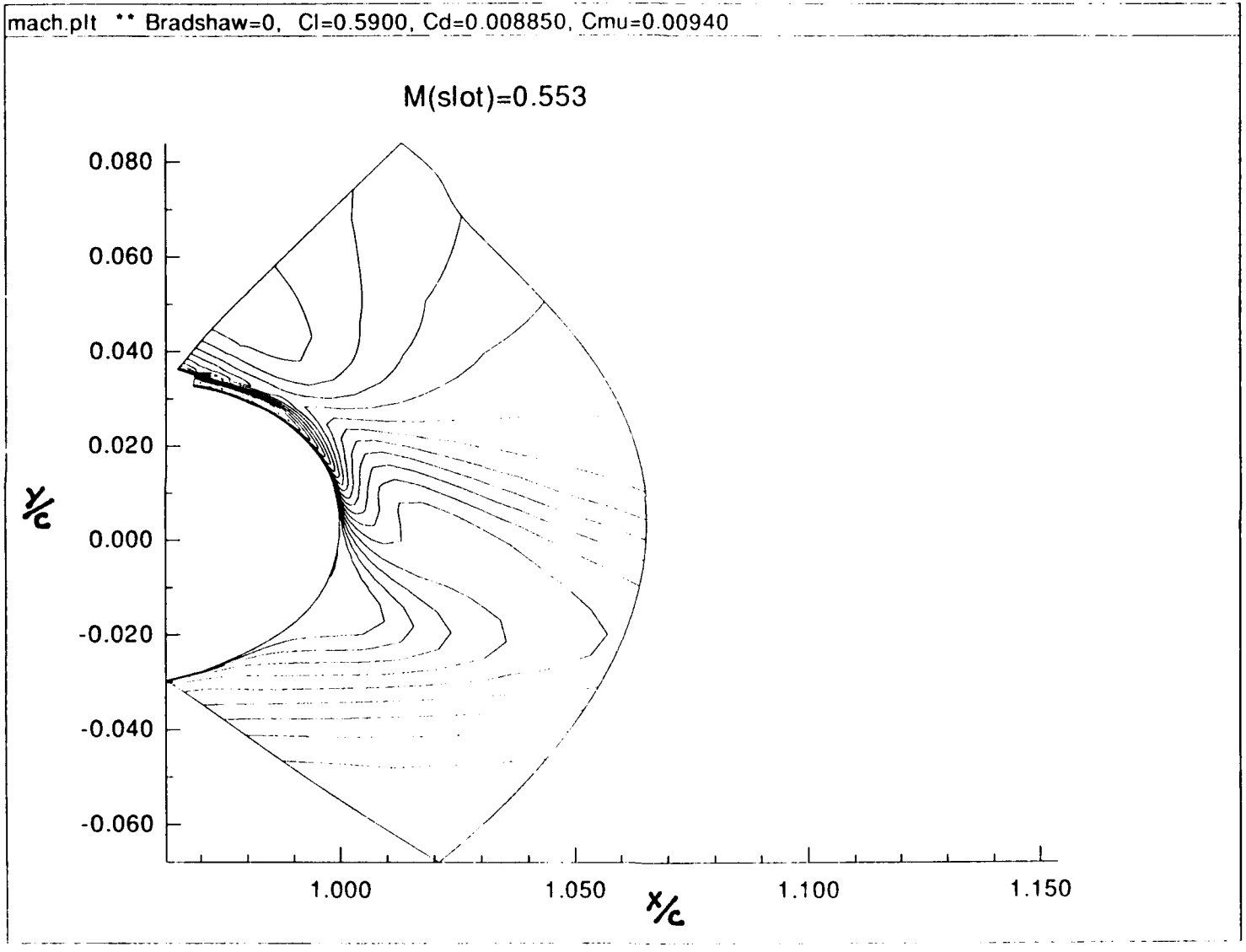

Figure 12. Mach contours, data point 35, Bradshaw=0

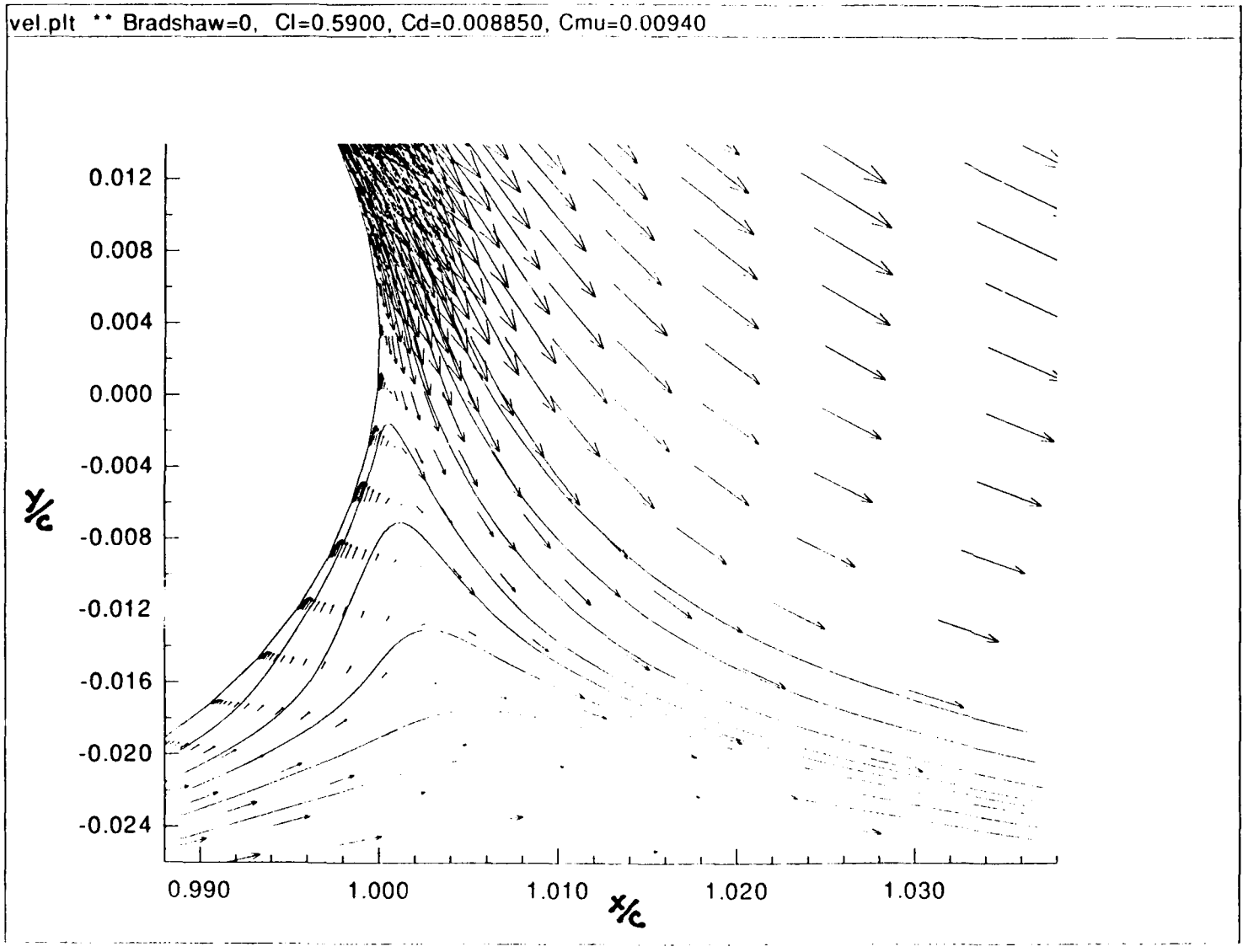

Figure 13. Velocity vectors, data point 35, Bradshaw=0

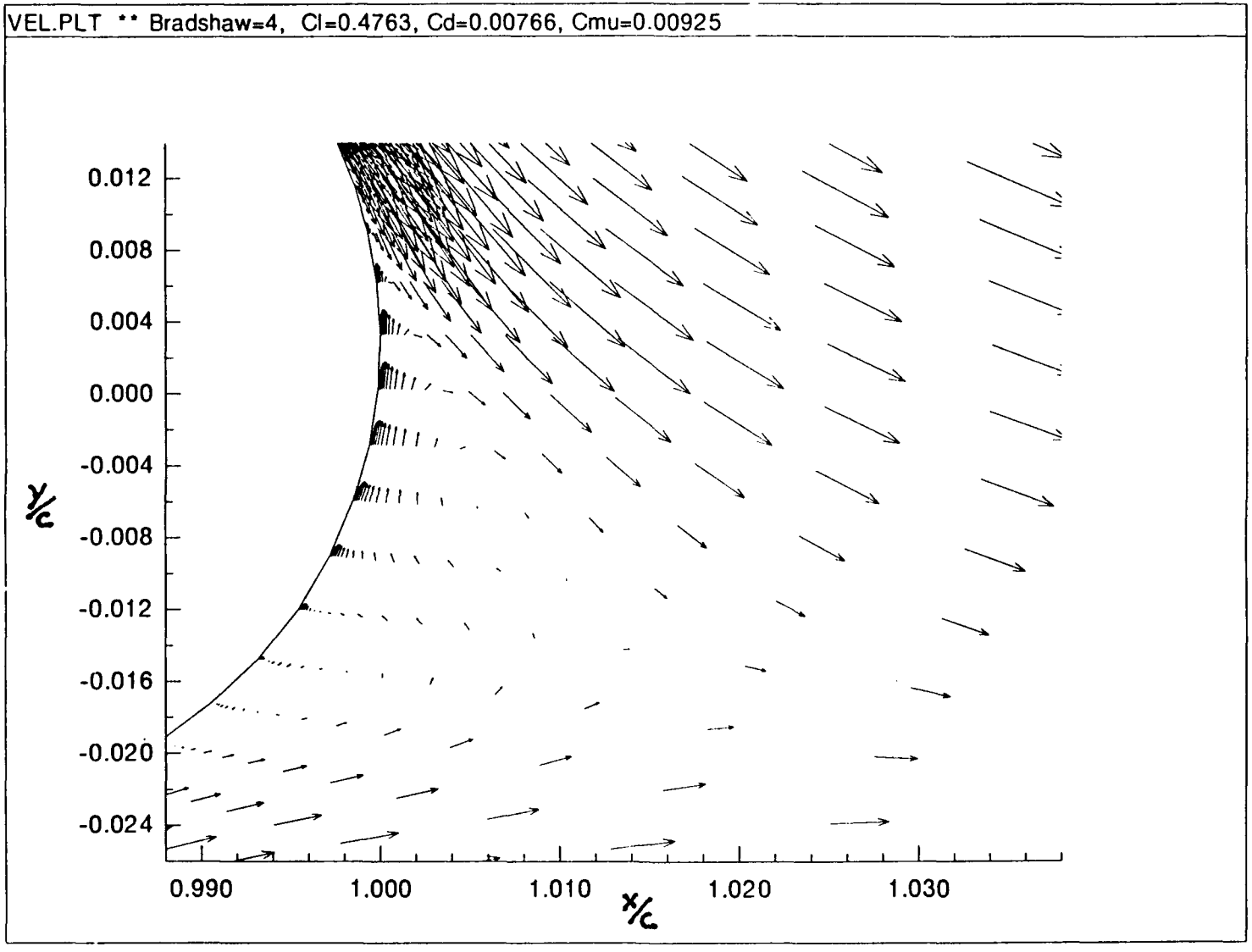

Figure 14. Velocity vectors, data point 35, Bradshaw=4

rotation and a lower vortex with a counterclockwise rotation against the airfoil surface. By the time the Bradshaw constant is 10, the separation point is above 0.012 and two definite vortices exist in the separation region, see Figure 15.

With θ=25, Figures 16 and 17 show the Mach contours and velocity vectors, respectively, around the Coanda surface. A comparison of Figures 13 and 17, show the substantial rearward progression of the separation point from approximately y/c = 0.006 to y/c > 0.012. The only input parameter changed was the empirical Bradshaw curvature correction; so what flow pattern, Figure 13 or Figure 17, is the actual model of the physical flow field? In reference 25, Shrewsbury diagrams the computational and experimental streamlines for a higher jet momentum value and for a different airfoil geometry, see Figures 18 and 19. However, these figures can still provide insight into the true flow field pattern. Comparison of the experimental streamlines, Figure 19, with the previously discussed computational streamlines, Figures 12-17, show the higher Bradshaw values provide a more accurate model of the flow field. However, the definitive stagnation streamline separating the two vortices is not evident in the computational solutions.

A better model of the flow in the trailing edge region is expected if a more sophisticated turbulence model were employed. Launder and Spalding (13) compare a two equation eddy viscosity model with other turbulence models for a

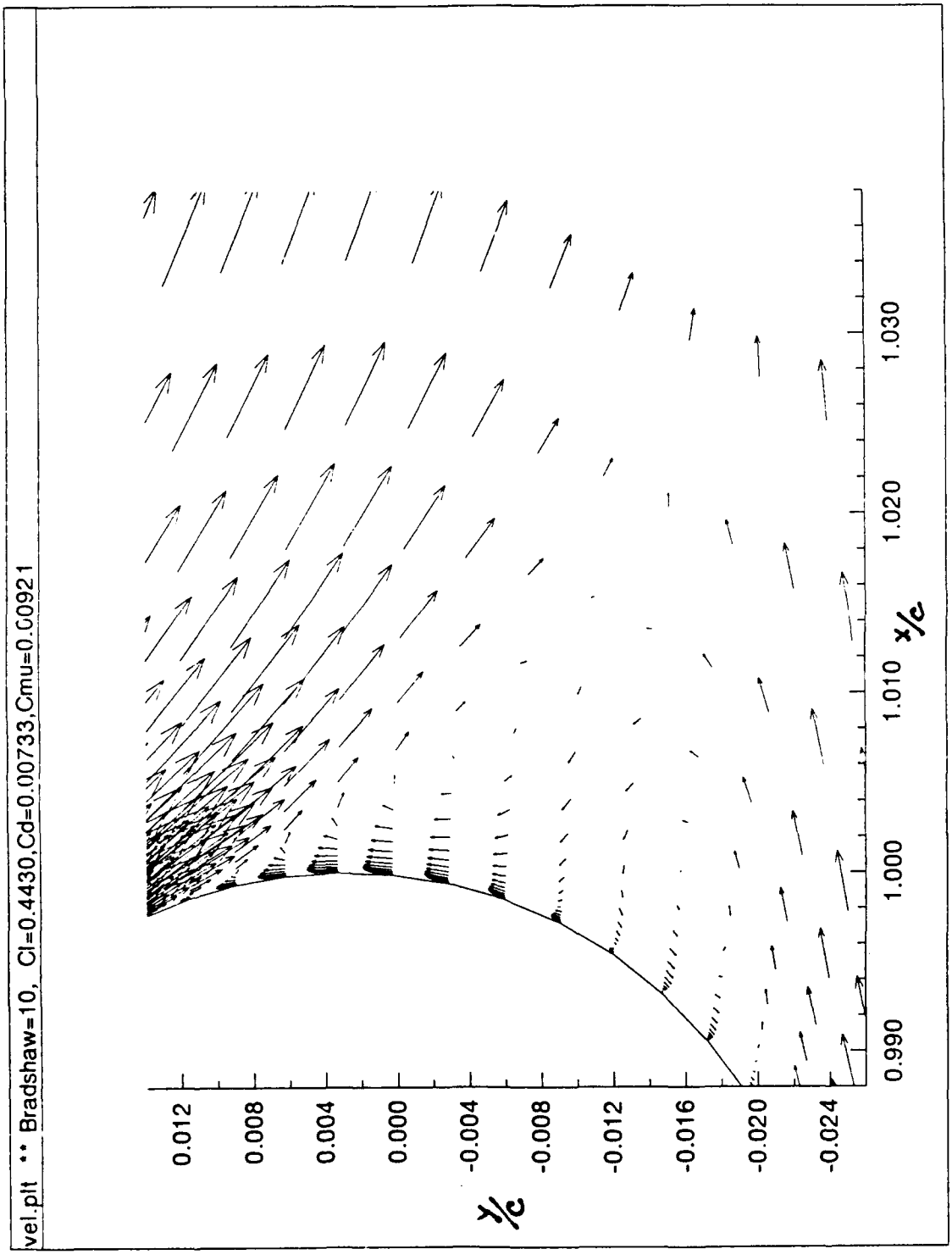

Figure 15. Velocity vectors, data point 35, Bradshaw=10

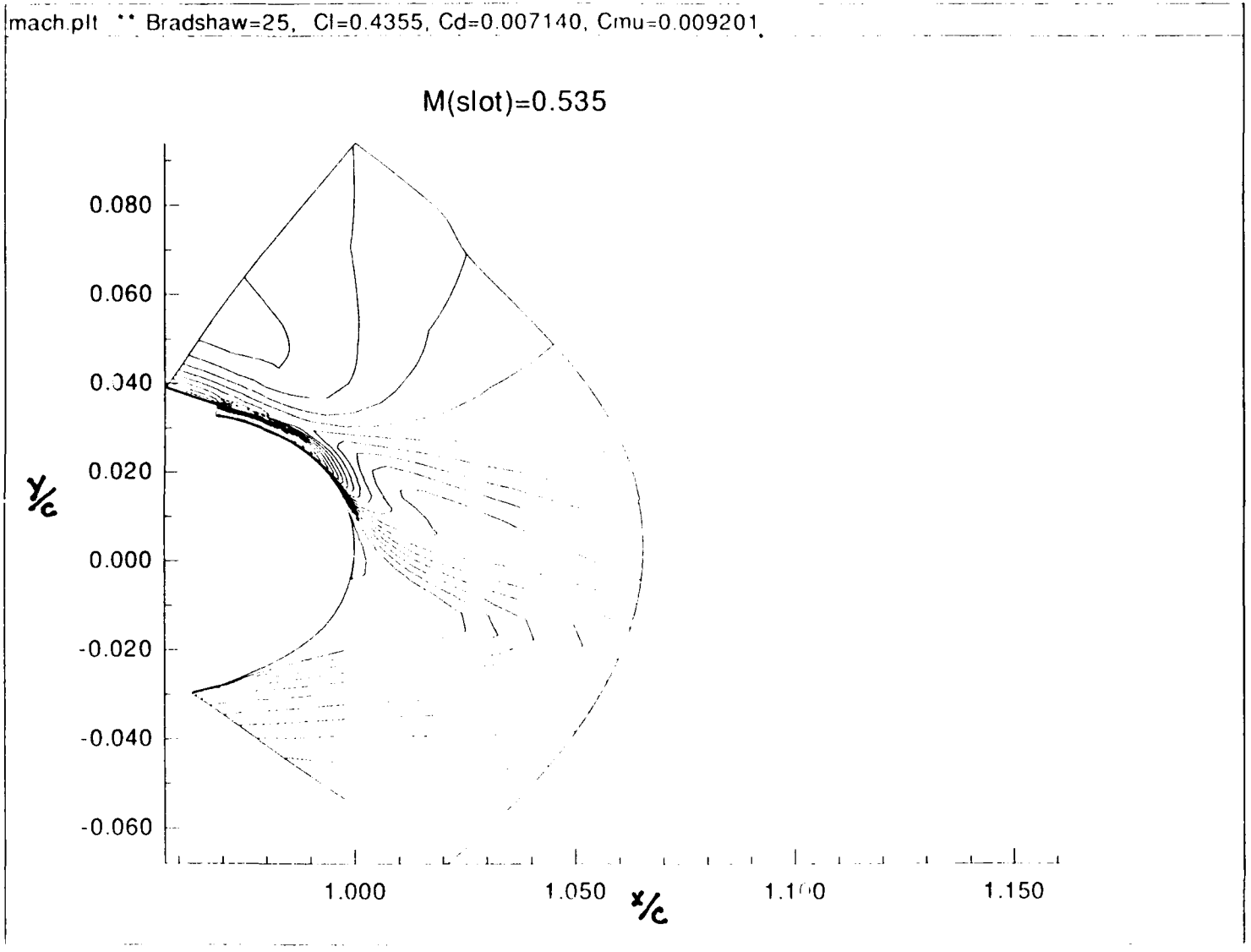

Figure 16. Mach contours, data point 35, Bradshaw=25

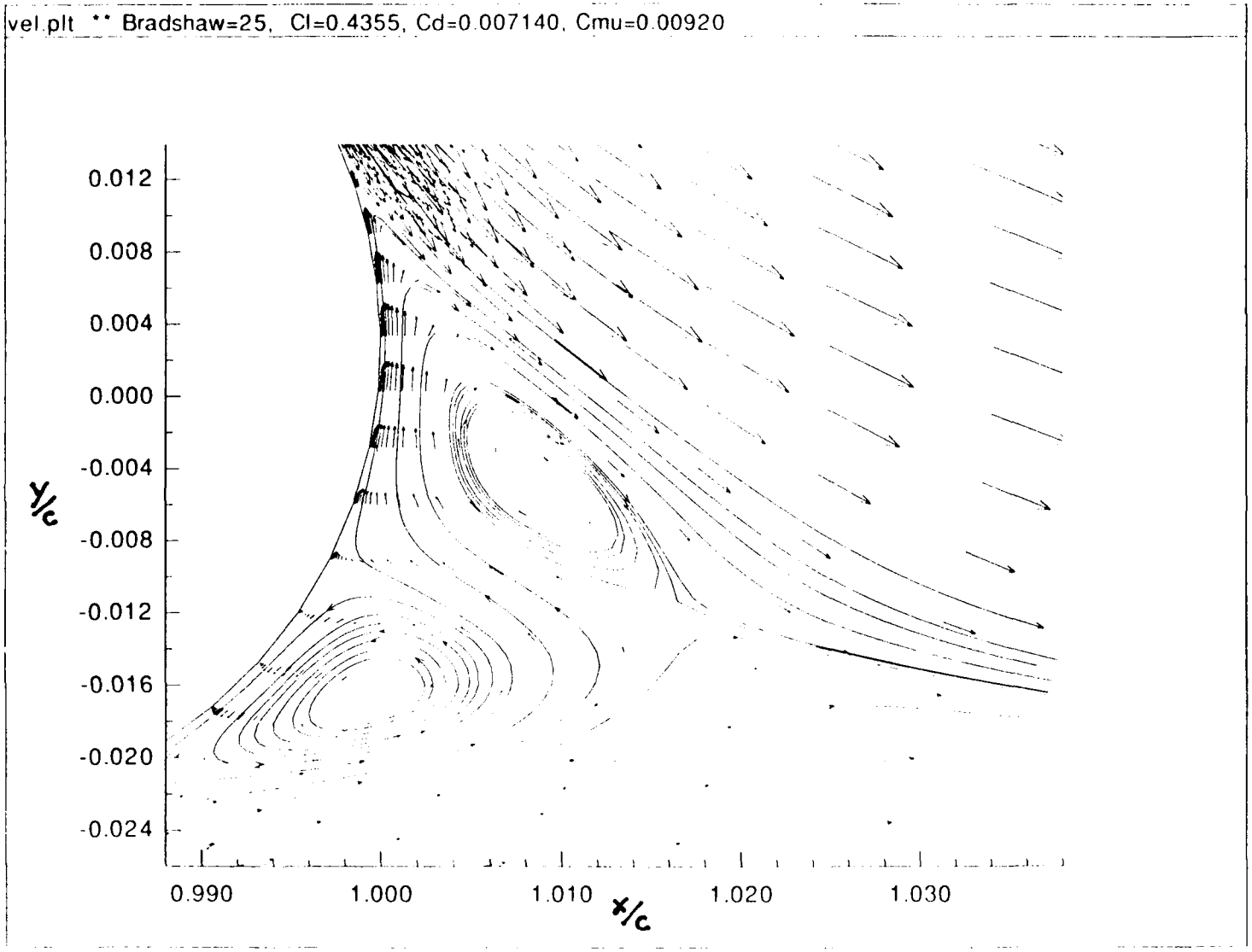

Figure 17. Velocity vectors, data point 35, Bradshaw=25

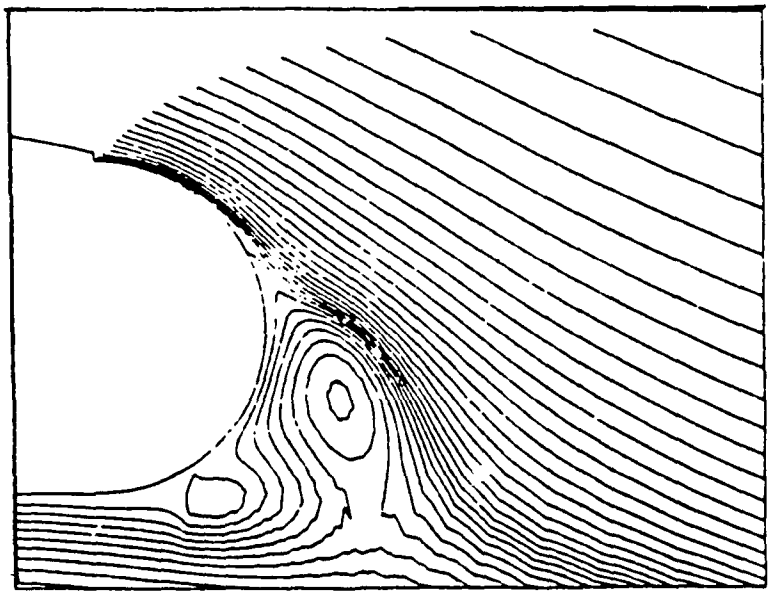

Figure 12. Shrewsbury's computational streamlines

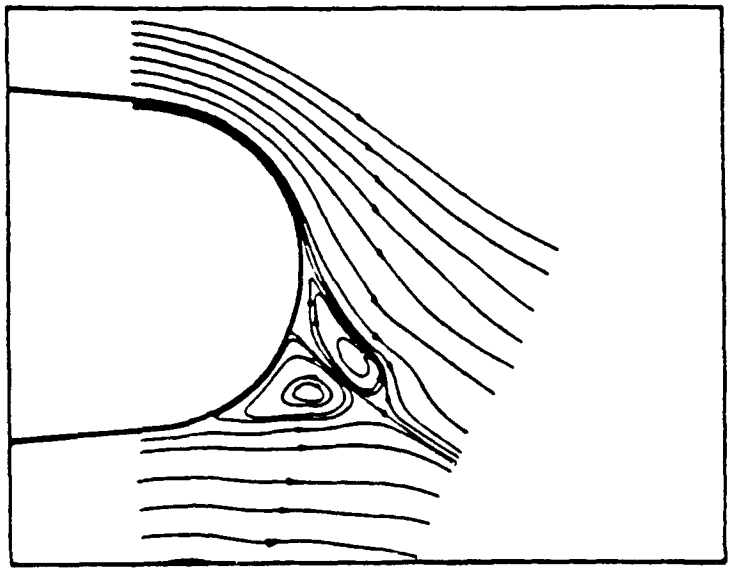

Figure 13. Shrewsbury's experimental streamlines

variety of flows. Two of the more interesting flow conditions are a wall jet and a recirculation zone. Launder and Spalding show the k-ϵ model provides a more accurate prediction of the velocity decay of a wall jet over a convex surface. In addition, they point out the accurate results obtained with the two equation model for recirculation regions. They conclude by saying the two equation eddy viscosity model "is the simplest kind of model that predicts both near-wall and free-shear-flow phenomena...its use has led to accurate predictions of flows with recirculation as well as those of the boundary layer kind." For these reasons, the adaptation of a k-ϵ model would most probably provide better predictions of the flow field.

The variation of the Bradshaw constant has an effect on more than just the flow characteristics. With increasing Bradshaw values, the various flow coefficients, C_l, C_d, C_m, and C_p change. The change in the coefficients with Bradshaw constant are plotted in Figures 20-23. The experimental values are those obtained by Abramson for the 103RE airfoil (1). All of the coefficients decrease in magnitude as Bradshaw is increased. But the more important trend is the asymptotic behavior of the curves. Above a Bradshaw value of 11, all of the parameters tend to stabilize at some constant value. This corresponds to the drastic flow field change between θ=0 and 10 and the relative steadiness of the flow field between θ=10 and 25.

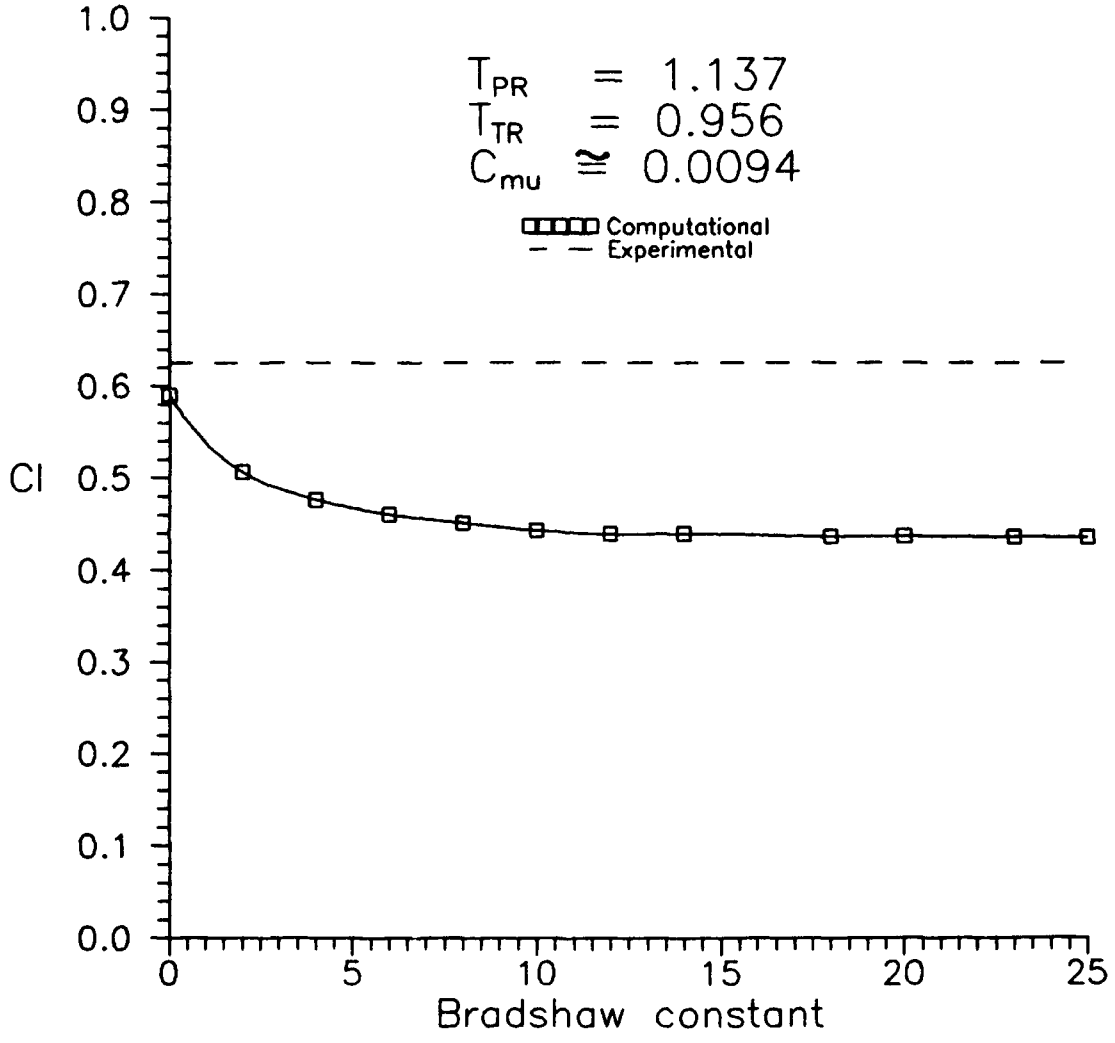

Figure 20. C_l versus Bradshaw, data point 35

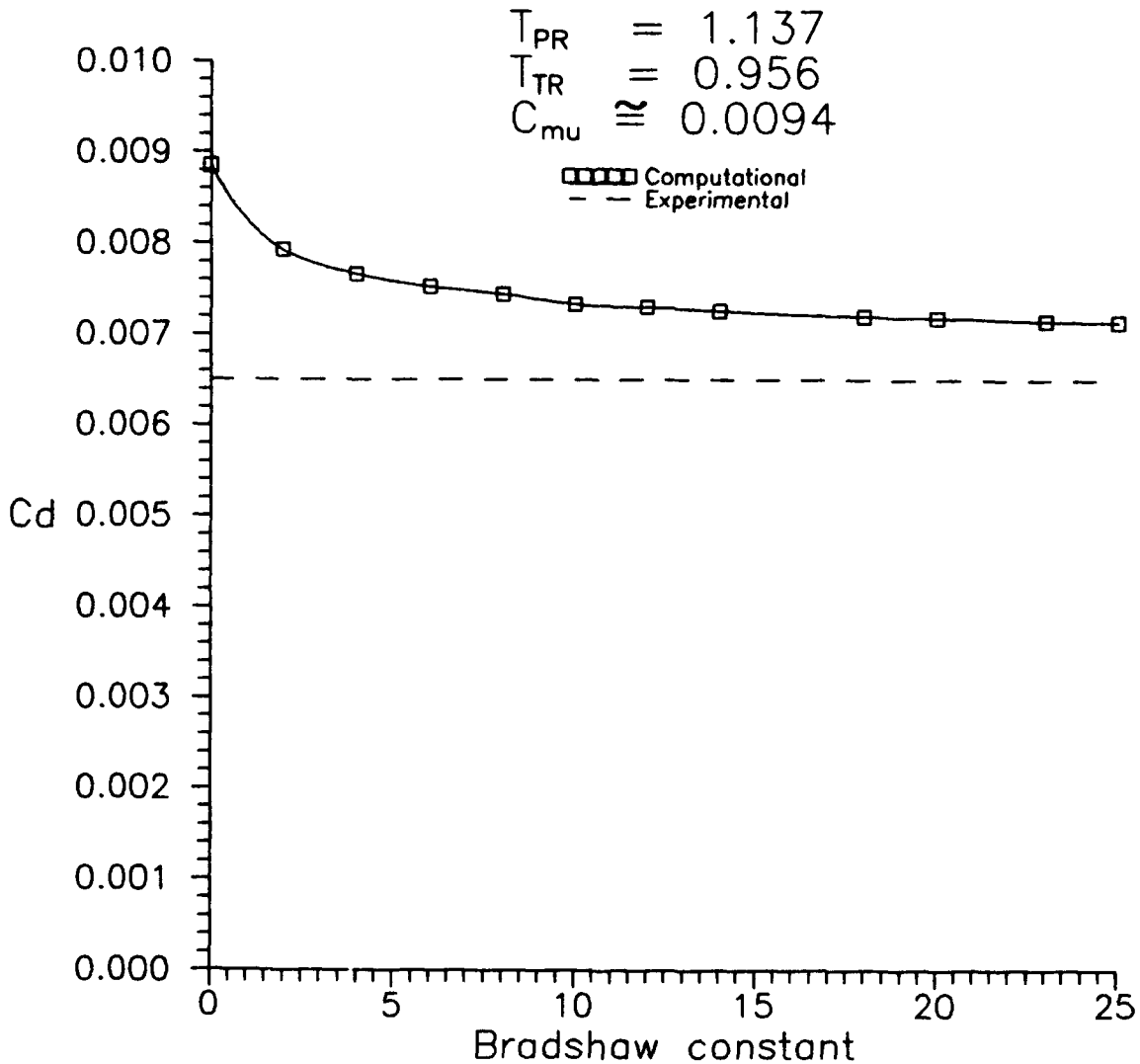

Figure 21. C_d versus Bradshaw, data point 35

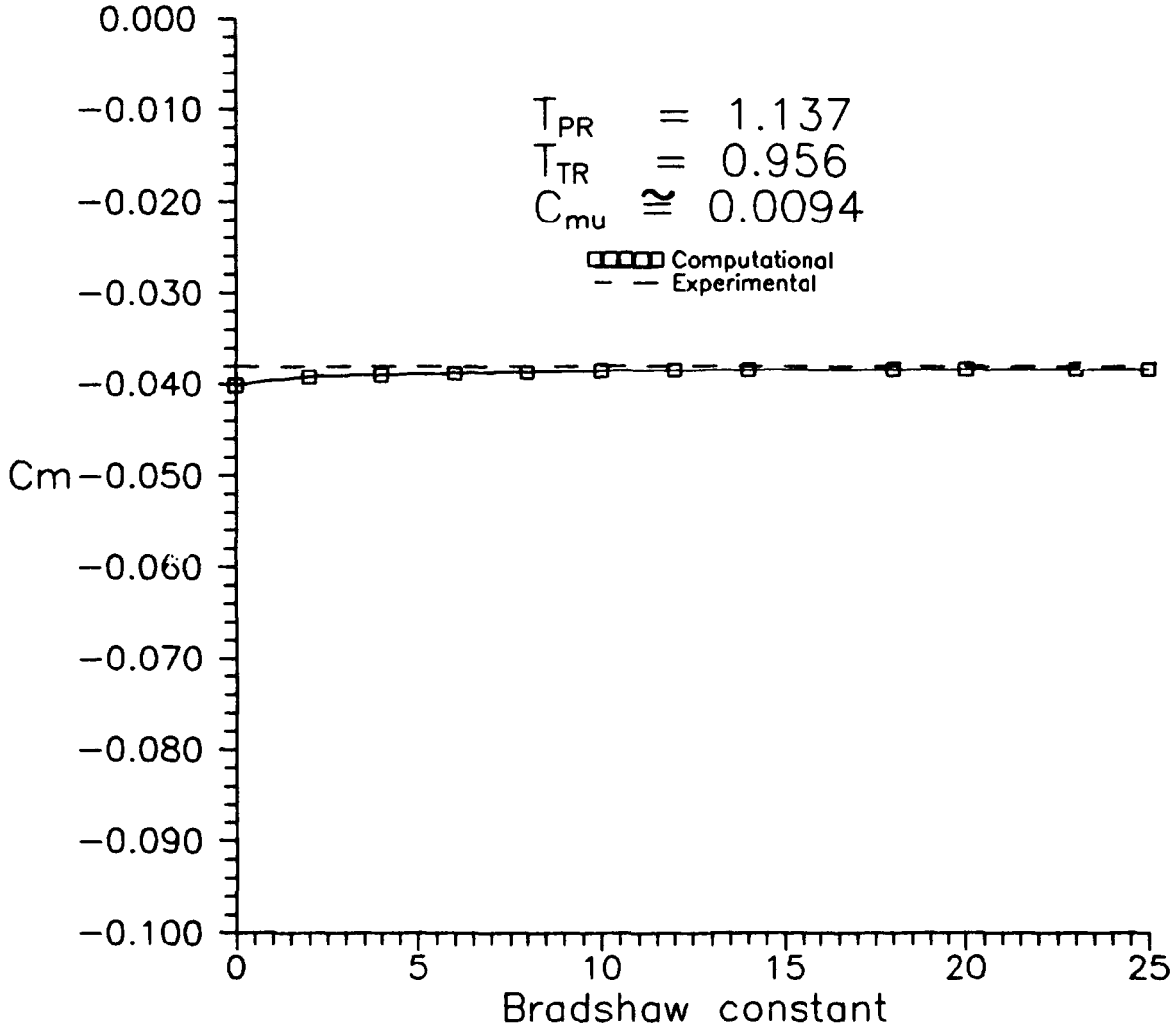

Figure 22. C_m versus Bradshaw, data point 35

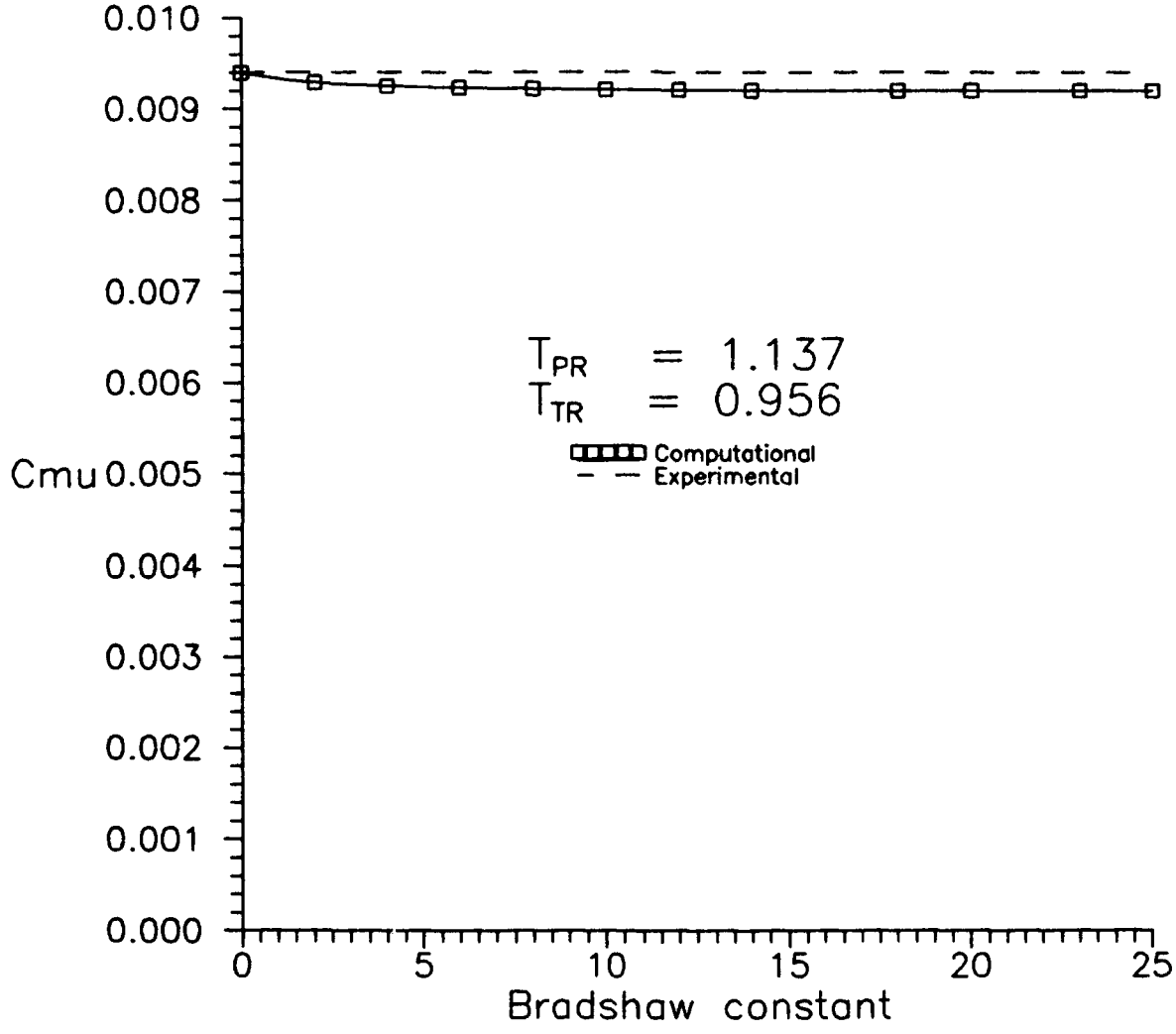

Figure 23 C_{mu} versus Bradshaw, data point 35

These variations in the flow coefficients bring several questions to mind. Could more accurate flow coefficients be computed if the momentum coefficient was matched with the experimental value instead of matching the jet pressure and temperature ratios? What value of jet ratios or momentum coefficient would be required to have the stable region of the flow coefficients ($\theta > 11$) accurately compare with the experimental results? Could all three of the coefficients, lift, drag, and moment, aline with the experimental values for the same jet momentum or jet pressure ratios? Figures 24-26 answer these questions.

On Figures 24-26 are four lines corresponding to the experimental data and the various computational variations. The three computational lines are: 1) the jet pressure and temperature ratios are matched with experimental data; 2) the momentum coefficient is matched with experimental data; 3) a constant momentum coefficient that best predicts the experimental values in the stable region ($\theta > 11$). As shown, the matching of jet momentum coefficients provides a better prediction of the actual flow values, but still not perfect. The momentum coefficient had to be increased by 34 percent, to C_{μ}=0.0126, before computed coefficients came into agreement with experimental coefficients.

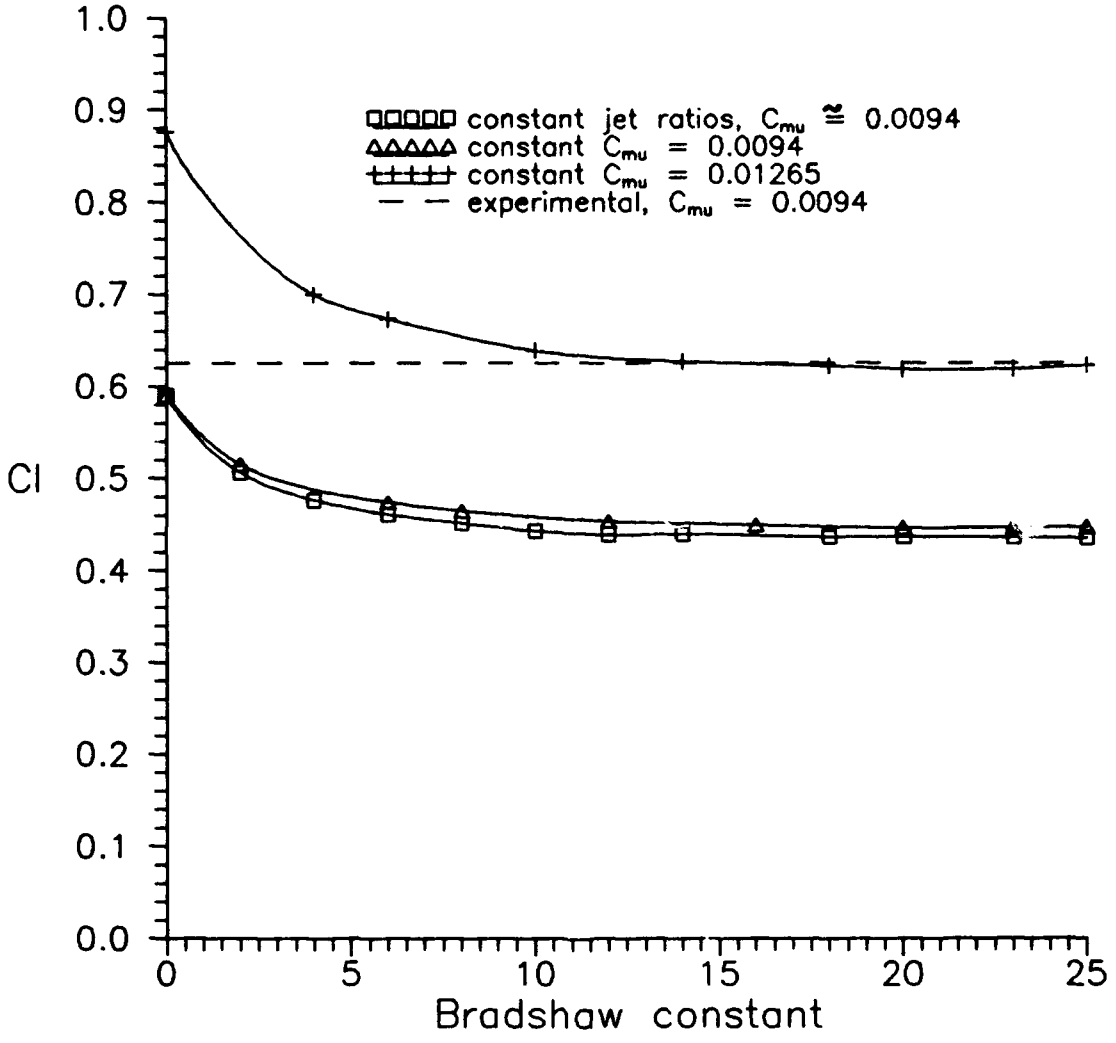

Figure 24 C_l versus Bradshaw, data point 35

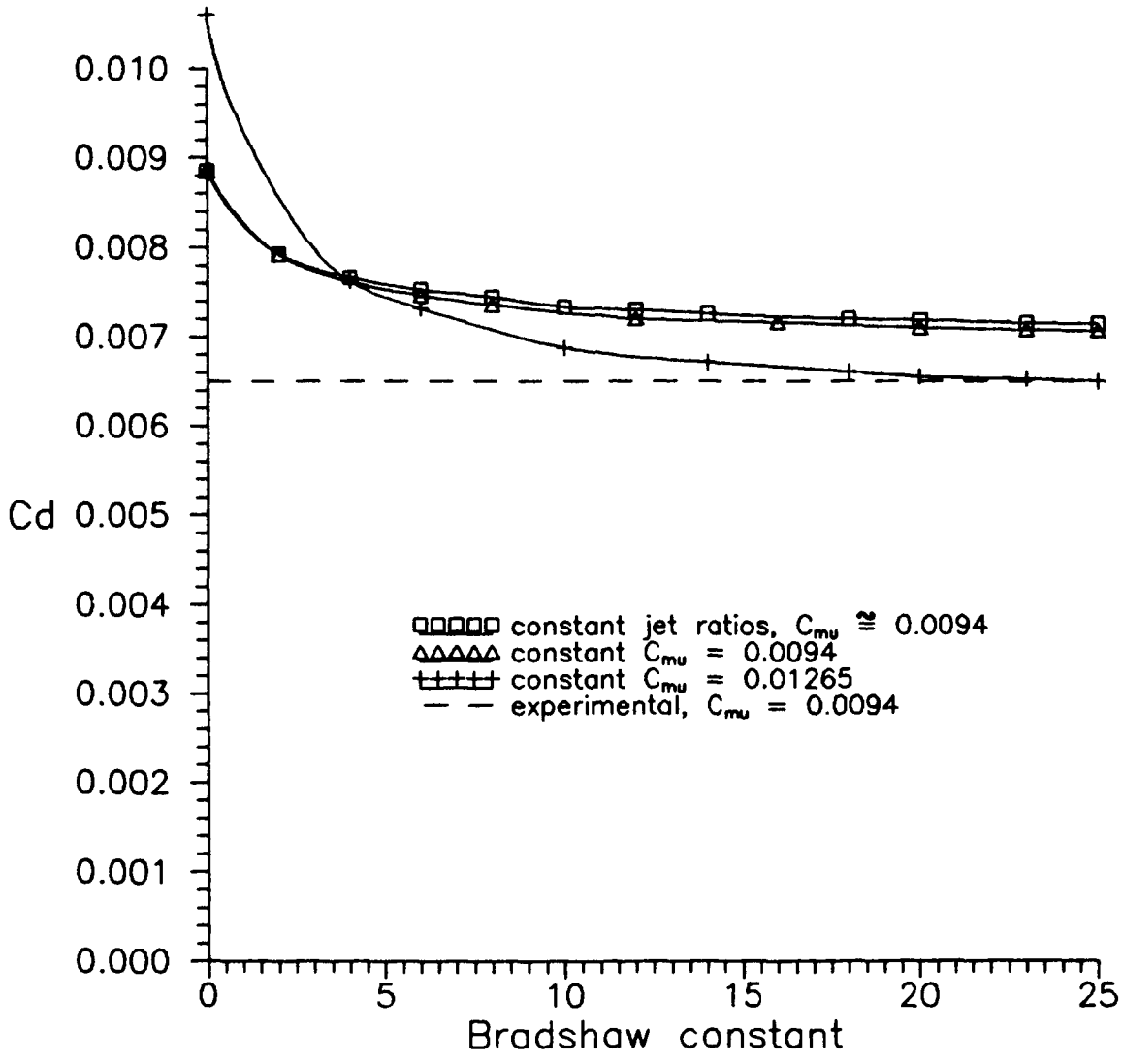

Figure 25 C_d versus Bradshaw, data point 35

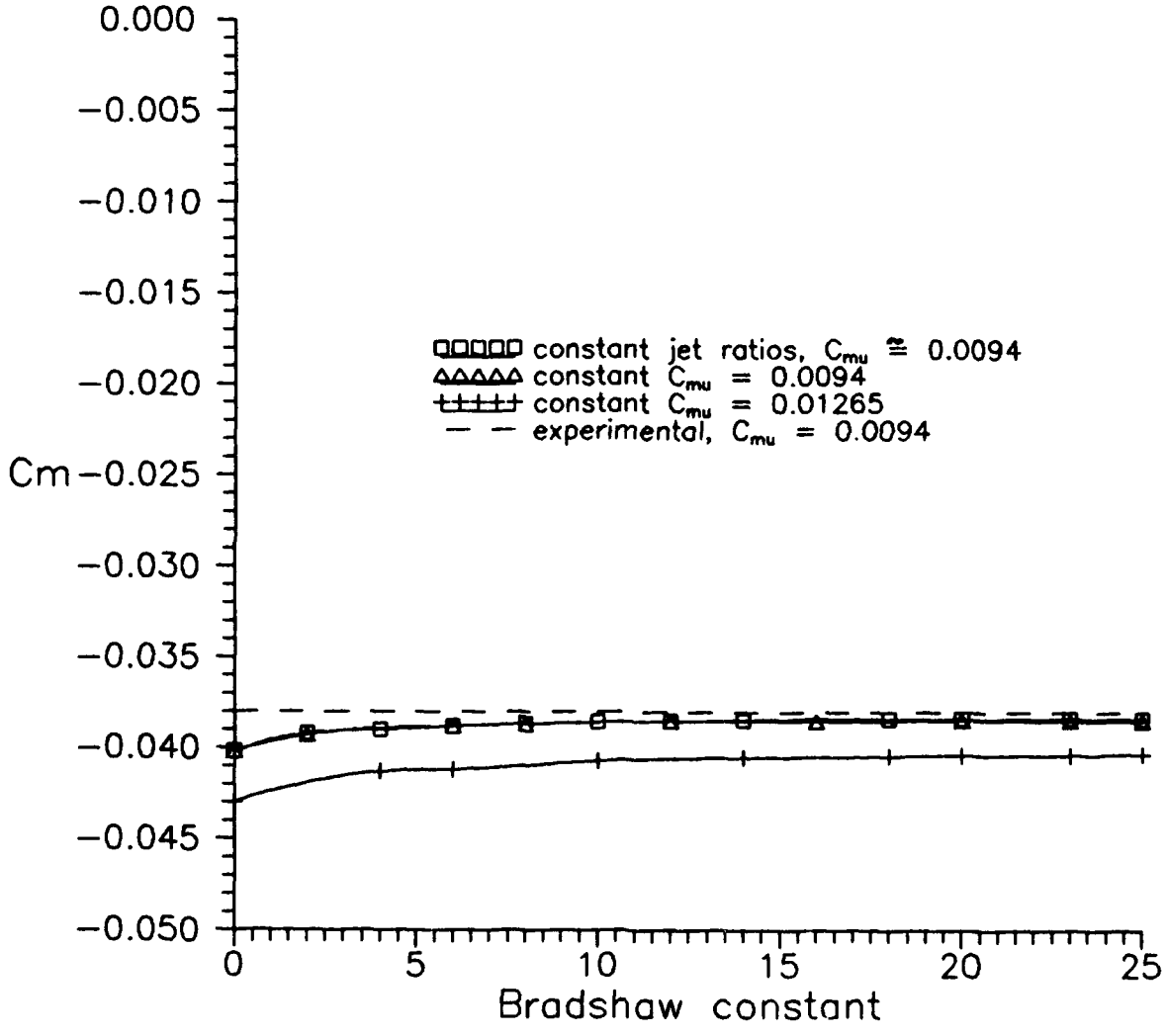

Figure 26 C_m versus Bradshaw, data point 35

The Bradshaw constant did not have a noticeable effect on any other flow characteristics. The boundary layer transition point remained constant along with the leading edge stagnation point. Various additional plots for data point 35 are contained in Appendix E.

The next step is to see if these same trends are evident for different flow conditions. Going to the higher jet blowing associated with data point 36, the same variation of the Bradshaw constant was repeated.

The Mach contours and velocity vectors for θ=0 are plotted in Figures 27 and 28. As is expected the separation point is further from the jet slot and a higher degree of entrainment is evident when compared with data point 35. The velocity vector diagram shows two vortices have already been formed. Does this signify a breakdown in the trends established for data point 35? Not necessarily, for a Bradshaw value of 4, see Figures 29 and 30, the separation point moves toward the jet slot and the vortex pattern changes slightly. The y/c location of the separation point for θ=4 is located at approximately 0.005 compared to -0.005 for θ=0. As seen on the Mach contour plot, the strength of the upper vortex increases. In addition, the lower vortex becomes more circular in nature than the elongated vortex for a Bradshaw value of 0. These same general trends continue through θ=23, see Figures 31 and 32.

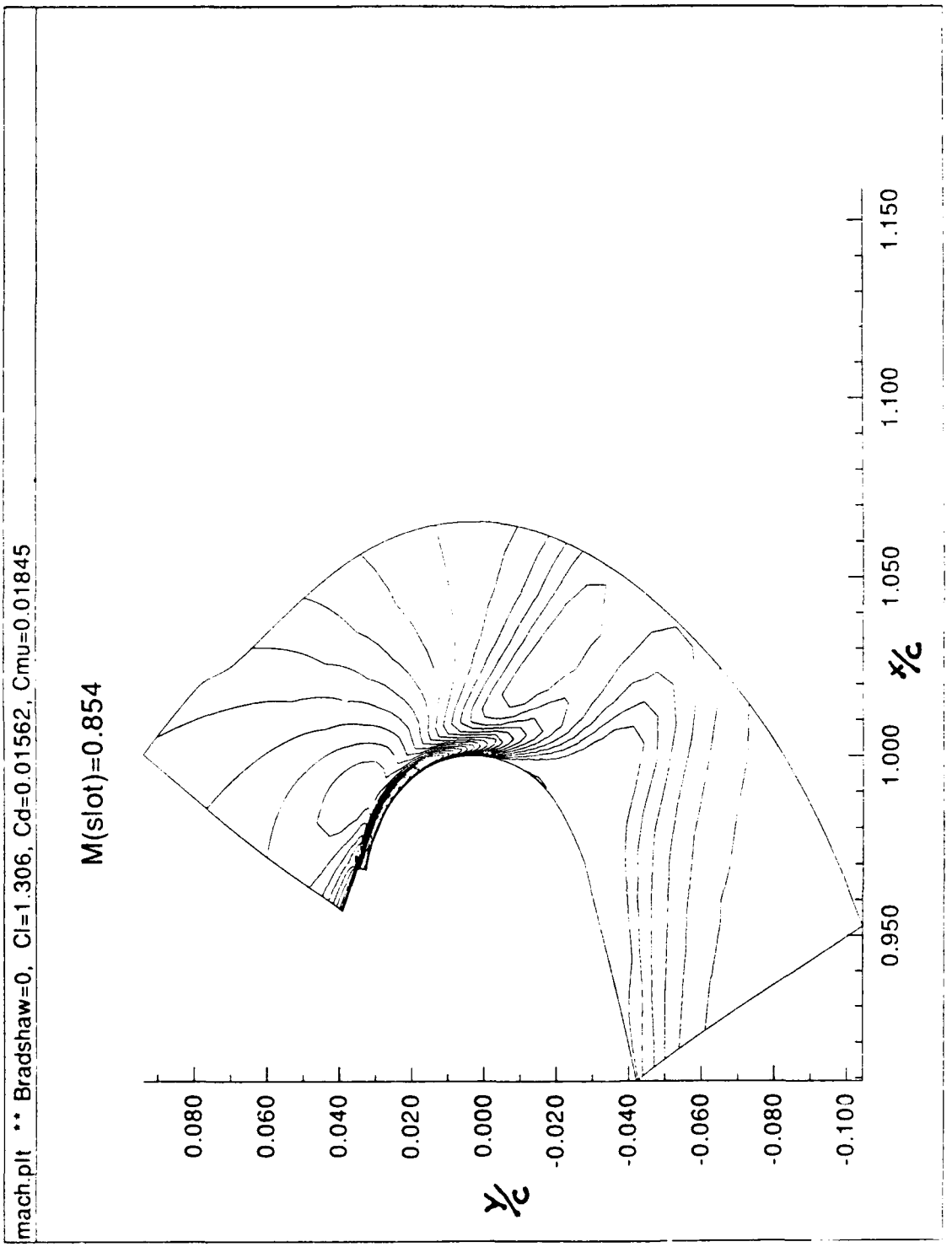

Figure 27. Mach contours, data point 36, Bradshaw=0

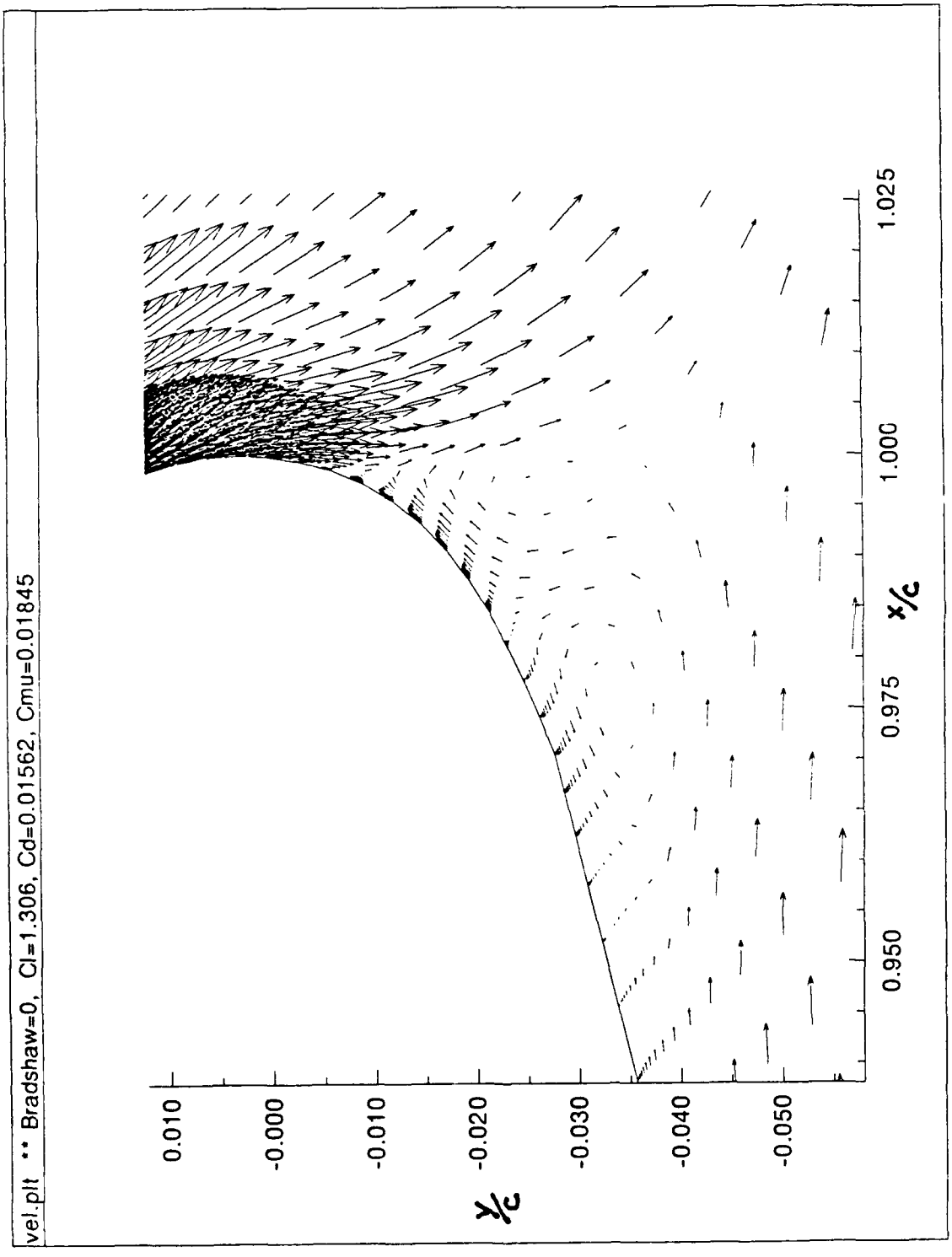

Figure 28. Velocity vectors, data point 36, Bradshaw=0

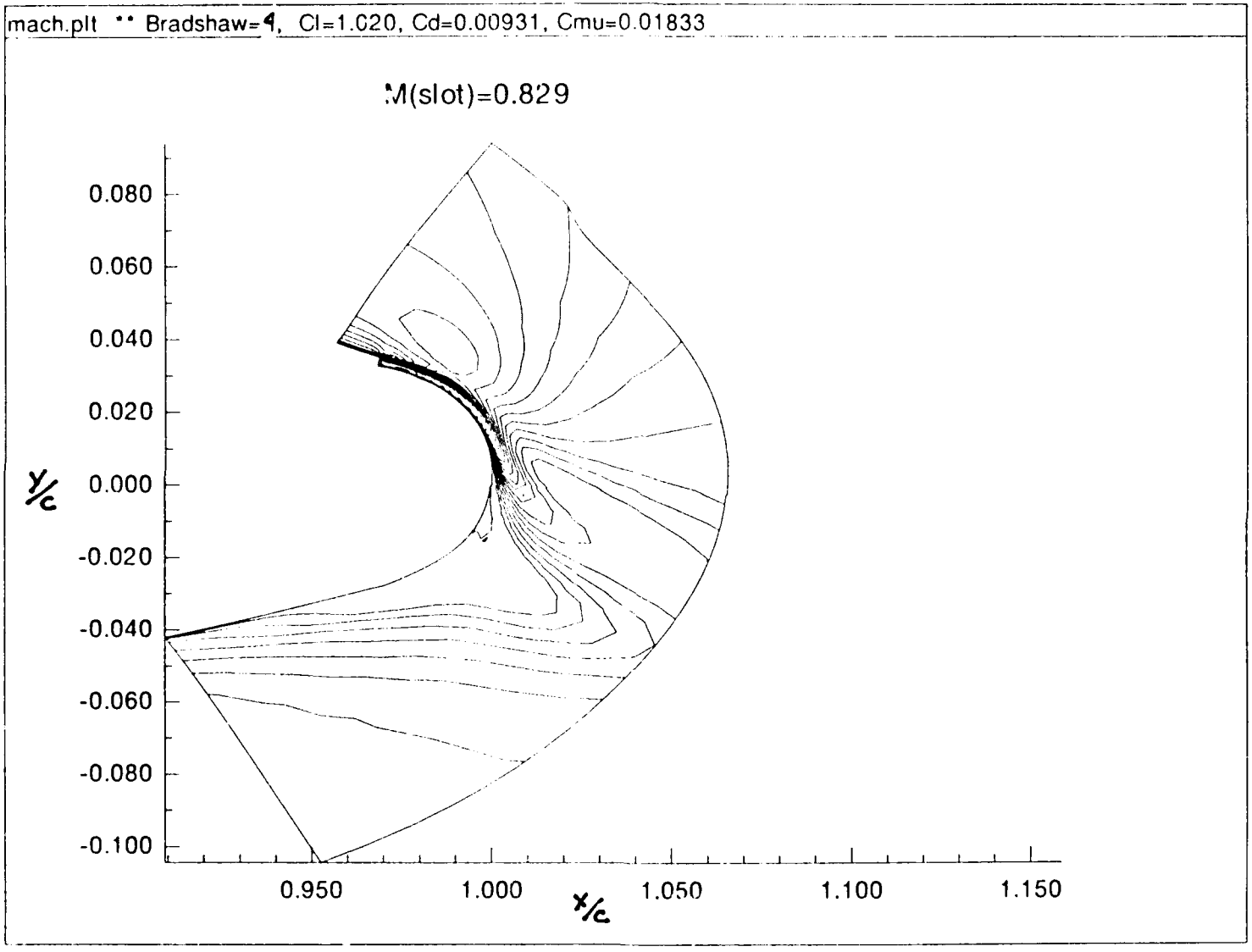

Figure 29. Mach contours, data point 36, Bradshaw=4

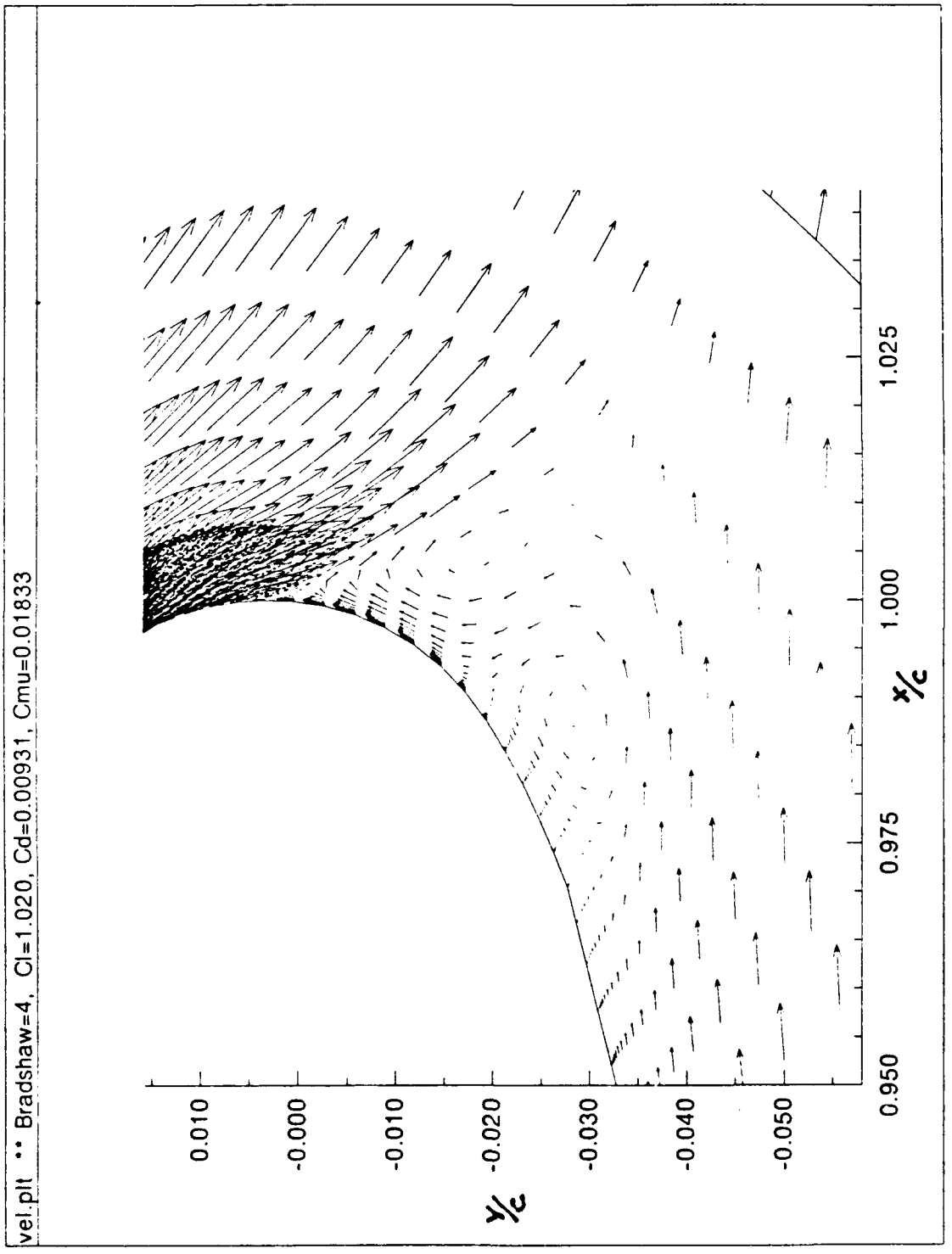

Figure 30. Velocity vectors, data point 36, Bradshaw=4

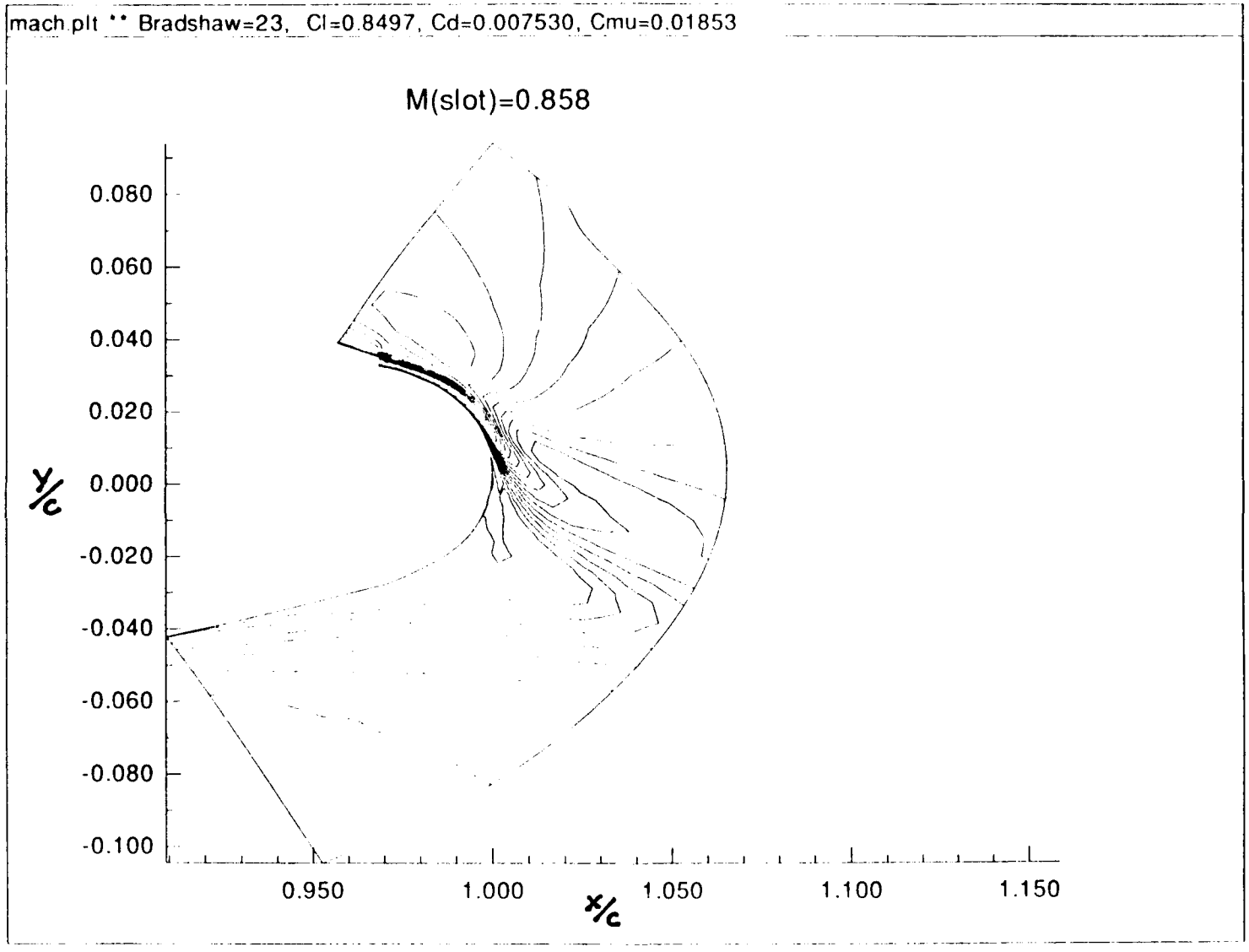

Figure 31. Mach contours, data point 36, Bradshaw=23

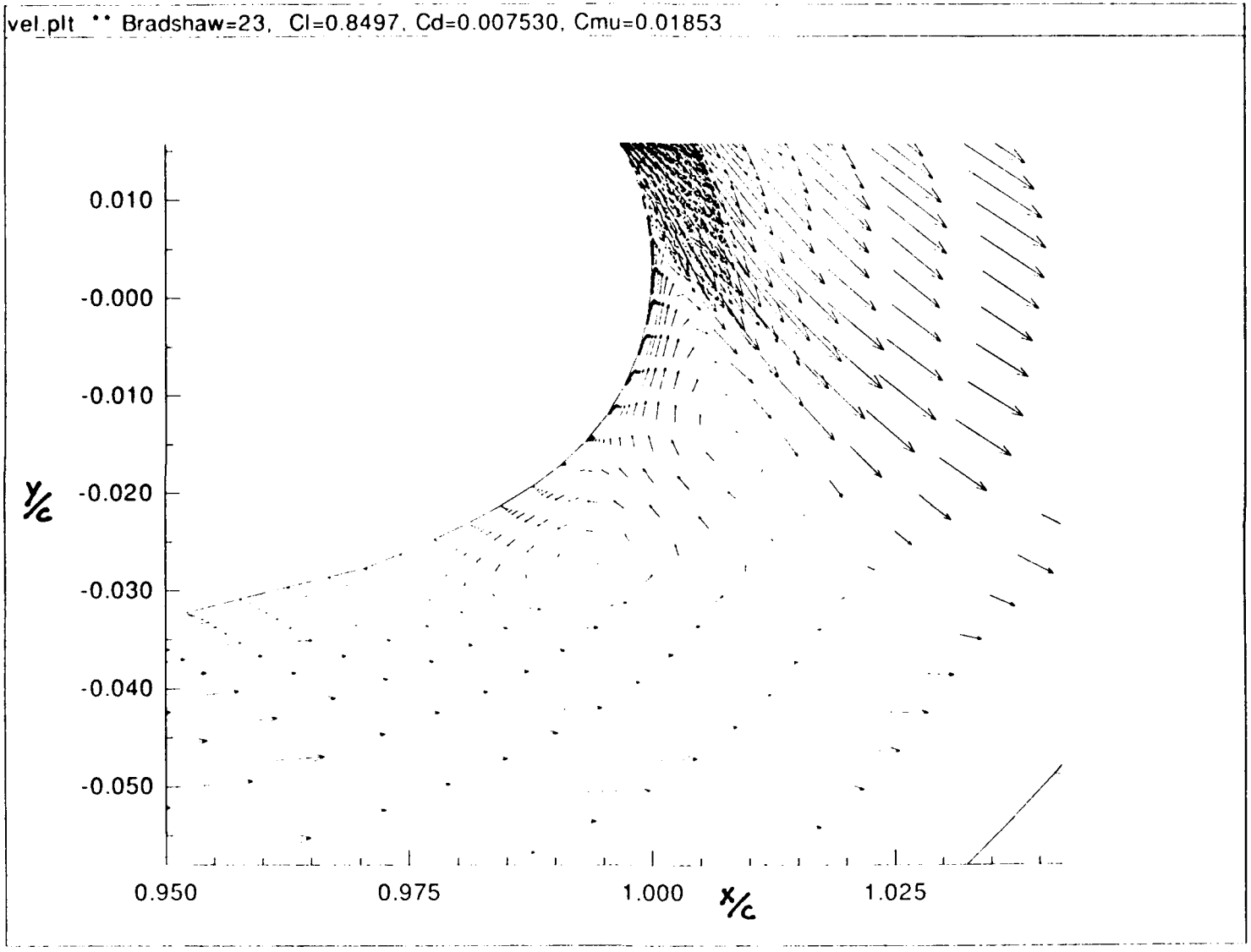

Figure 32. Velocity vectors, data point 36, Bradshaw=23

Again, the question arises as to which flow pattern best represents the real flow conditions? Based on the previous data point and the trends with this data point, it is safe to conclude the higher Bradshaw values are a better indicator of the true flow conditions.

The same general trends for the flow coefficients are seen in Figures 33 - 36. However, the Bradshaw value where the coefficients appear to reach a steady value is increased to 15 or more. The accuracy of the lift and moment coefficients is comparable to the lower C_μ case, but the drag coefficient is substantially less accurate. Note, the computed C_l coincides with experimental results at θ slightly greater than two. However, the flow field nor the drag and moment coefficients agree with the experimental results. Appendix F contains additional plots of the flow for data point 36.

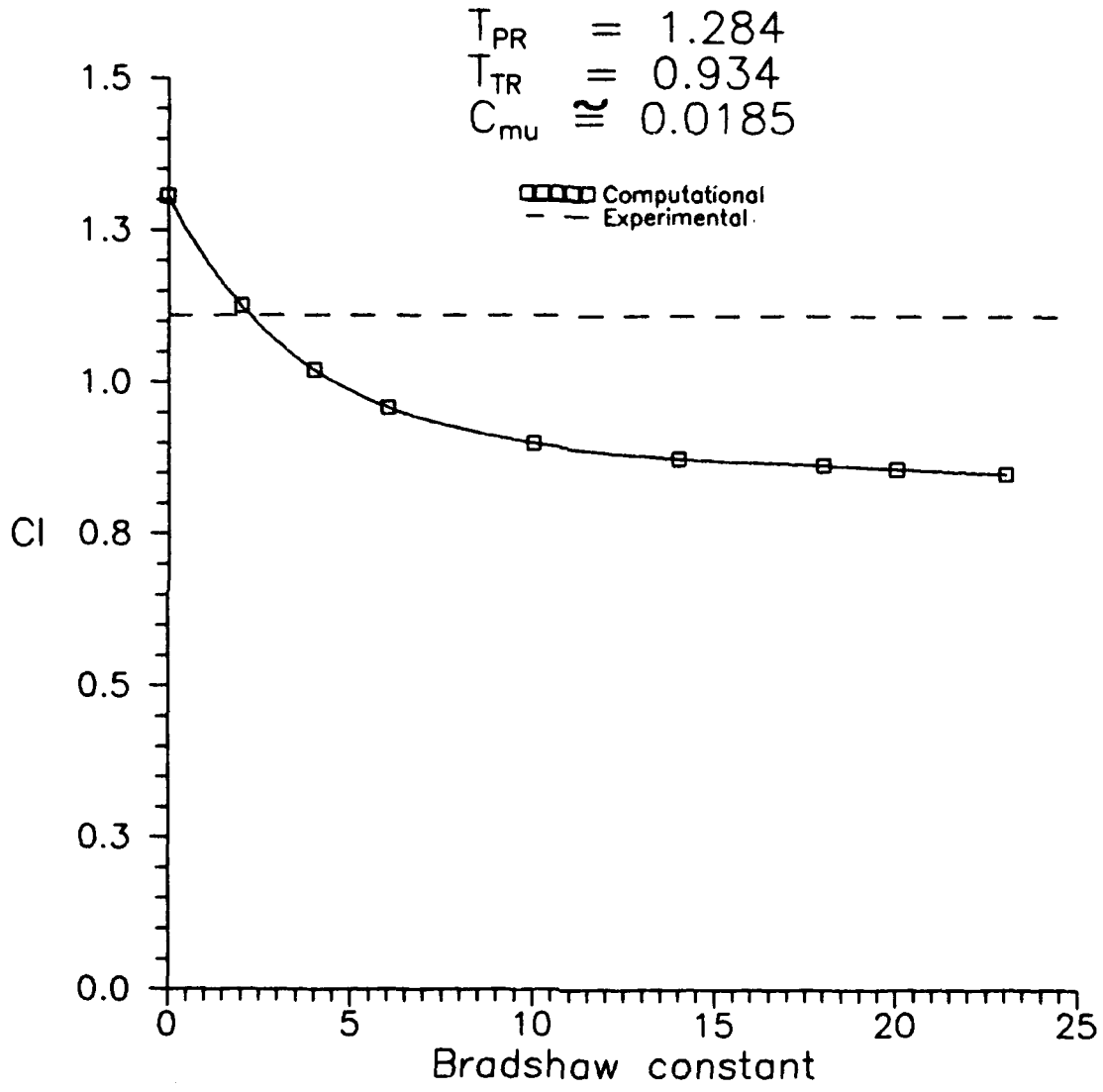

Figure 33 C_l versus Bradshaw, data point 36

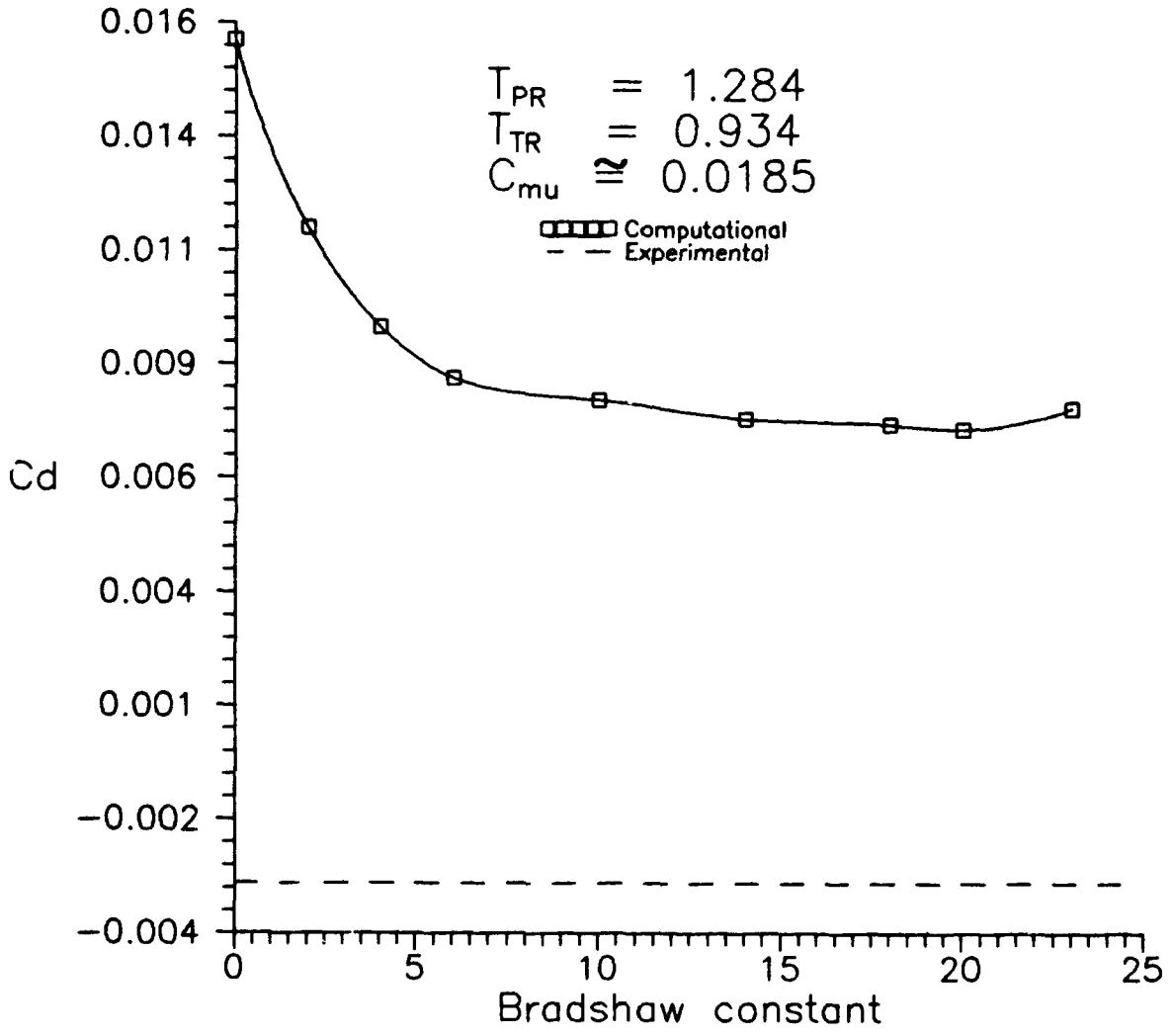

Figure 34 C_d versus Bradshaw, data point 36

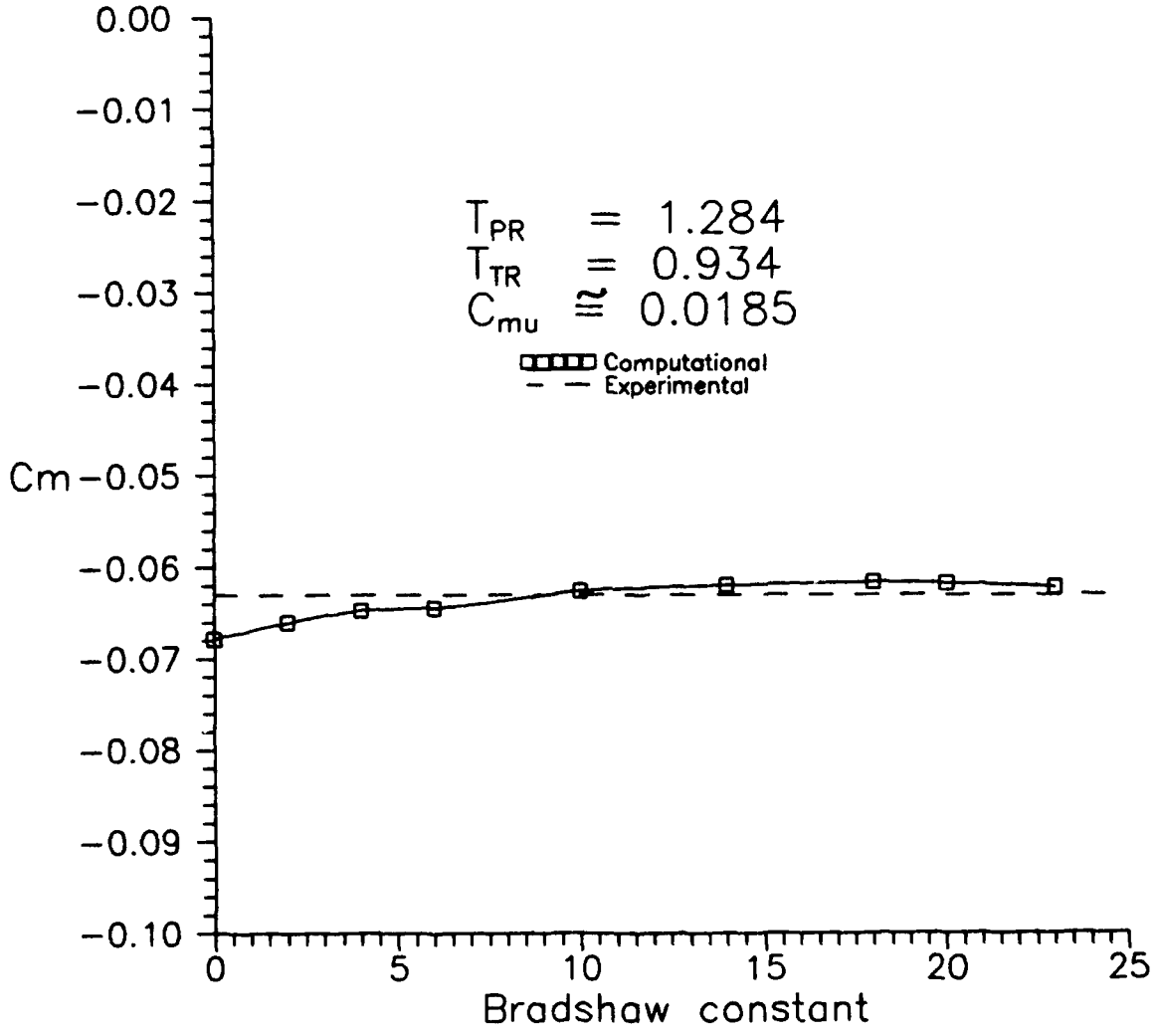

Figure 35 C_m versus Bradshaw, data point 36

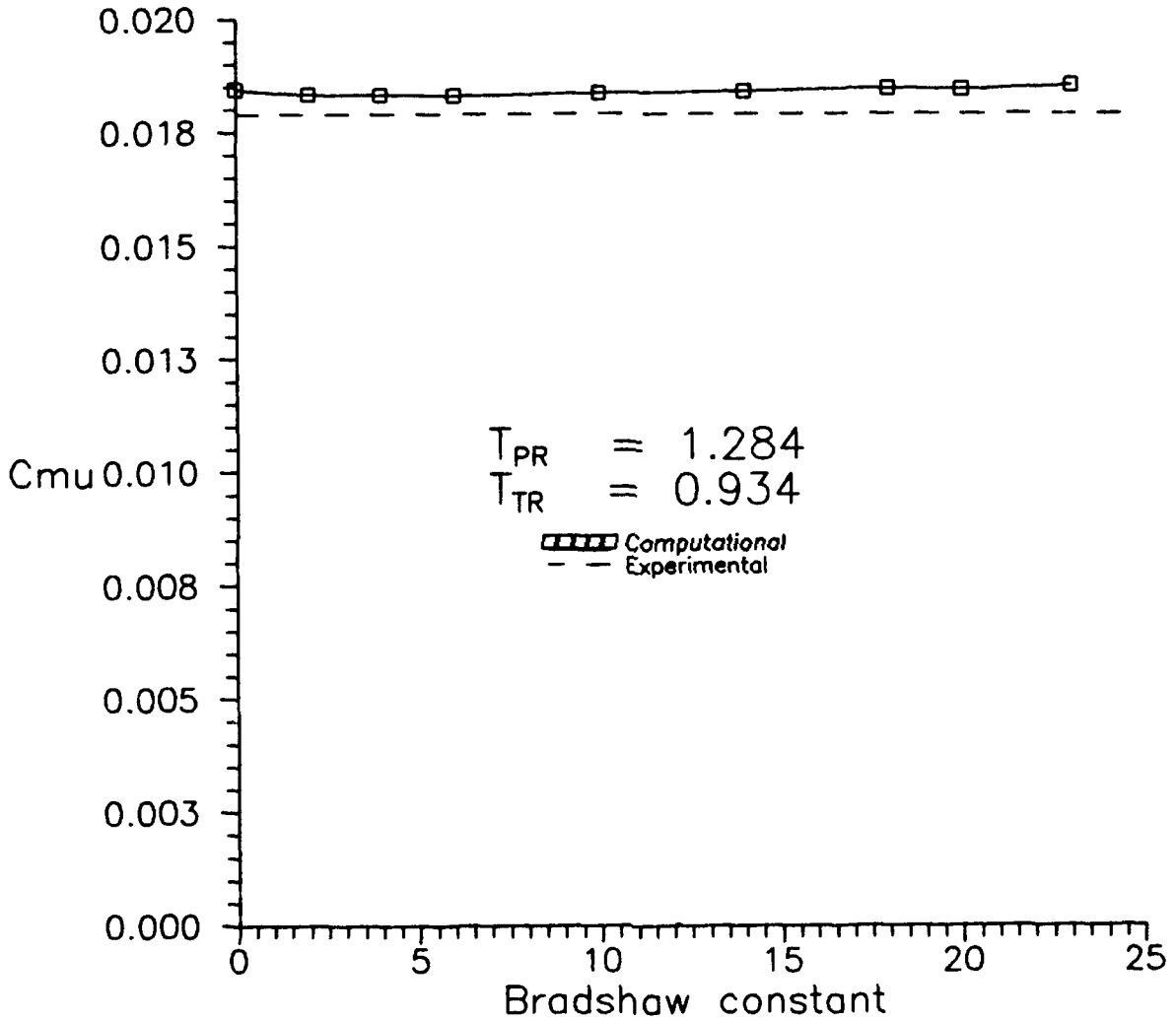

Figure 36 C_{mu} versus Bradshaw, data point 36

IV. CONCLUSIONS

Before a computational algorithm can analyze the benefits of a concept, it must first be able to accurately predict the performance. This report did not try to analyze the benefits of the circulation control airfoil concept. Instead, the purpose of this study was to investigated the effects of the empirical Bradshaw curvature correction on the predictive capabilities of a Beam-Warming approximate factorization algorithim.

4.1 Circular Cylinder

Using the circular cylinder to get a handle on the Bradshaw constant is a worthwhile investigation. However, the wake dominated characteristics of the cylinder flow field introduce many complexities not characteristic of the airfoil flow field. The main complication is the unsteady flow for most Reynolds number regimes. Indeed, this study was unable to achieve a steady "converged" solution for the flow around the cylinder. From the research accomplished, the lack of convergence might be attributed to a combination of three major factors:

1) Actual flow phenomena
2) Inadequate turbulence model
3) Grid

4.2 103RE Airfoil

The Bradshaw constant has a pronounced effect on the flow around the airfoil. The Bradshaw value influences both the flow field pattern and the flow coefficients, C_l, C_d, and C_m. The development of the flow field in the rear separation region approaches agreement with experimental observations as θ is increased. However, a primary and secondary vortex develop instead of two counter rotating vortices separated by a stagnation streamline. The flow coefficients stabilize as the Bradshaw value increases. This stabilization corresponds to a stabilization in the computed flow pattern. Beyond this stabilizing point, further increases in θ have little effect on the coefficients or the flow pattern.

These same general trends apply to higher blowing coefficients, with a couple of exceptions. The variation in the flow pattern is not as pronounced and the flow coefficients take longer to level off. Instead of the development of two vortices, the higher blowing case saw the refinement of the two vortices with increasing θ. The point of stabilization for the flow coefficients occurred at a higher value of θ. Any correlation between this delay and the flow refinement is not totally obvious for this case.

When the jet ratios are matched with experimental values, the momentum coefficients computed by the algorithm are, in general, lower than the experimental momentum coefficients. By matching the momentum coefficients instead

of the jet ratios, the computed flow coefficients are slightly better. However, the values are still not predictive of the actual experimental results. A substantial increase, more than 30 percent, in the momentum coefficient was required before computational values for lift and drag were in close agreement with the experimental results. The moment coefficient tended to lose accuracy as the momentum coefficient was increased.

Finally, a predictive ability was never achieved with the use of the Bradshaw modified Baldwin-Lomax turbulence model. A higher order turbulence model must be incorporated before any attempt can be made at predicting the flow around a circulation control airfoil.

V. RECOMMENDATIONS

For future research, the following recommendations are made:

1) Apply a higher order turbulence model. A two equation eddy viscosity model will preclude the need for an empirical curvature constant and improve the accuracy of the computational algorithim. The jet velocity decay and the recirculating flow can be modeled more accurately with a k-ϵ turbulence model (13).

2) Conduct a more indepth investigation into the flow around a cylinder at high Reynolds numbers. See if a "converged" solution can be obtained for a Reynolds number where the Strouhal number has a definitive peak.

3) Conduct an experimental investigation concentrating on the flow field in the separation region. What form do the streamlines take and how do they change with a change in the flow conditions? An analysis of the turbulence in the separation region can help with the development of CFD turbulence models (17:3).

4) Conduct a theoretical study of the circulation control flow field. Continue Smith and Dunham's (8,27) work on a cylinder with a jet slot and try to expand this mathematical model to a circulation control airfoil.

APPENDIX A. Non-dimensional Variables

In general, the governing equations are non-dimensionalized for convenience. By non-dimensionalizing, characteristic parameters such as Mach number, Reynolds number, and Prandtl number appear in the equations. And the flow variables are normalized as a result of non-dimensionalizing. To non-dimensionalize, a reference length, L, must be established along with reference values for velocity, temperature, density, and viscosity. In this case the chord is chosen as the reference length and the freestream values for velocity, temperature, density, and viscosity are used (3:619). The non-dimensional parameters are denoted as $()^*$. Note, in the main body of the report the superscripts are dropped.

$$x^* = \frac{x}{L} \quad y^* = \frac{y}{L} \quad u^* = \frac{u}{\vec{V}_\infty} \quad v^* = \frac{v}{\vec{V}_\infty}$$

$$T^* = \frac{T}{T_\infty} \quad \rho^* = \frac{\rho}{\rho_\infty} \quad p^* = \frac{p}{\rho_\infty \vec{V}^2} \quad e^* = \frac{e}{\vec{V}^2}$$

$$\mu^* = \frac{\mu}{\mu_\infty} \quad t^* = \frac{t}{L/\vec{V}}$$

Using the perfect gas law and substituting in for p, the non-dimensional pressure equation becomes

$$p^* = \frac{\rho RT}{\rho_\infty \vec{V}_\infty^2} = \rho^* T^* \left(\frac{RT_\infty}{\vec{V}_\infty^2}\right) = \frac{\rho^* T^*}{\gamma M_\infty^2}$$

Thus, the non-dimensional freestream pressure becomes

$$p_\infty^* = \frac{1}{\gamma M_\infty^2}$$

The dimensional form of Southerland's law is written as

$$\mu = \frac{C_1 T^{3/2}}{T + C_2}$$

When non-dimensionalized Southerland's law becomes

$$\mu^* = \frac{\mu}{\mu_\infty} = \left[\frac{C_1 T^{3/2}}{T + C_2}\right]\left[\frac{T_\infty + C_2}{C_1 T_\infty^{3/2}}\right] = (T^*)^{3/2}\left[\frac{T_\infty + C_2}{T + C_2}\right]$$

or

$$\mu^* = (T^*)^{3/2}\left[\frac{1 + C_2^*}{T^* + C_2^*}\right]$$

where

$$C_2^* = \frac{C_2}{T_\infty}$$

The parameter k/c_v shows up often in the governing equations. The non-dimensional version is obtained from the definition of the Prandtl number

$$Pr = \frac{c_p \mu}{k} = \frac{c_p}{c_v} \frac{\mu}{k/c_v}$$

Solving for k/c_v

$$\frac{k}{c_v} = \frac{\gamma \mu}{Pr} = \frac{\gamma \mu^* \mu_\infty}{Pr}$$

If the chord length (reference length) is one then

$$Re = \frac{1}{\mu_\infty}$$

thus

$$\frac{k}{c_v} = \frac{\gamma \mu^*}{Re\, Pr}$$

APPENDIX B. Jacobian Matrices

The Jacobian matrices specified in Eqs 64 and 65 are expanded below. Before calculating the derivatives, the vectors are rewritten in terms of the conserved variables (6:98)

$$A = \frac{\partial F_1}{\partial \tilde{U}}$$

$$A = \begin{pmatrix} 0 & \xi_x & \xi_y & 0 \\ \xi_x\varphi - uu_c & u_c - (\gamma-2)\xi_x u & \xi_y u - (\gamma-1)\xi_x v & (\gamma-1)\xi_x \\ \xi_y\varphi - vu_c & \xi_x u - (\gamma-1)\xi_y u & u_c - (\gamma-2)\xi_y v & (\gamma-1)\xi_y \\ (2\varphi - \gamma E_t)u_c & (\gamma E_t - \varphi)\xi_x - (\gamma-1)uu_c & (\gamma E_t - \varphi)\xi_y - (\gamma-1)vu_c & \gamma u_c \end{pmatrix}$$

$$B = \frac{\partial G_1}{\partial \tilde{U}}$$

$$B = \begin{pmatrix} 0 & \eta_x & \eta_y & 0 \\ \eta_x\varphi - uv_c & v_c - (\gamma-2)\eta_x u & \eta_y u - (\gamma-1)\eta_x v & (\gamma-1)\eta_x \\ \eta_y\varphi - vv_c & \eta_x u - (\gamma-1)\eta_y u & v_c - (\gamma-2)\eta_y v & (\gamma-1)\eta_y \\ (2\varphi - \gamma E_t)v_c & (\gamma E_t - \varphi)\eta_x - (\gamma-1)uv_c & (\gamma E_t - \varphi)\eta_y - (\gamma-1)vv_c & \gamma v_c \end{pmatrix}$$

where

$$\varphi = \frac{1}{2(\gamma-1)(u^2+v^2)}$$

The R and S matrices are defined as

$$R = \frac{\partial V_1}{\partial \tilde{U}_\xi}$$

$$R = \frac{1}{\rho}\begin{pmatrix} 0 & 0 & 0 & 0 \\ -(b_1 u + b_2 v) & b_1 & b_2 & 0 \\ -(b_2 u + b_3 v) & b_2 & b_3 & 0 \\ b_{41} & b_{42} & b_{43} & b_{44} \end{pmatrix}$$

where

$$b_{41} = -\left[b_1^2 + 2b_2 uv + b_3 v^2 + b_4 \gamma(\gamma-1)\,(u^2+v^2-E_t)\right]$$

$$b_{42} = b_1 - b_4 \gamma(\gamma-1)\,u + b_2 v$$

$$b_{43} = b_2 u + b_3 - b_4 \gamma(\gamma-1)$$

$$b_{44} = b_4 \gamma(\gamma-1)$$

$$S = \frac{\partial W_2}{\partial \tilde{U}_\eta}$$

$$S = \frac{1}{\rho}\begin{pmatrix} 0 & 0 & 0 & 0 \\ -(d_1 u + d_2 v) & d_1 & d_2 & 0 \\ -(d_2 u + d_3 v) & d_2 & d_3 & 0 \\ d_{41} & d_{42} & d_{43} & d_{44} \end{pmatrix}$$

where

$$d_{41} = -\left[d_1^2 + 2d_2 uv + d_3 v^2 + d_4 \gamma(\gamma-1)(u^2+v^2-E_t)\right]$$

$$d_{42} = d_1 - d_4 \gamma(\gamma-1)u + d_2 v$$

$$d_{43} = d_2 u + d_3 - d_4 \gamma(\gamma-1)$$

$$d_{44} = d_4 \gamma(\gamma-1)$$

APPENDIX C. Program Inputs

The Beam-Warming code developed by Dr Miguel Visbal allows a wide variety of user inputs. The user can specify the type of scheme, type of grid, turbulence model parameters, time stepping employed, jet slot conditions, among others. The following list describes all of the user defined inputs (31).

CARD 1:

H, PHI - Time differencing scheme to be employed with the Beam-Warming algorithm. H and PHI correspond to θ_1 and θ_2, respectively, as seen in most documentation.

Scheme	H	PHI	Order
Euler explicit	0	0	first
Euler implicit	1	0	first
Trapezoidal	0.5	0	second
3-point backward	1	0.5	second
Leap frog	0	0.5	first

CARD 2:

NSTEPI - Iteration number to start with.

TAU - Physical time at NSTEPI.

CARD 3:

IL - Number of grid lines in azimuthal (or wrap around) direction. If any grid lines are overlapped make sure they are included in the value for IL. If using the INGFDLNS program then IL is four more than the number of grid lines originally built due to overlapping.

JL - Number of grid points in normal direction.

ILE - Grid index for airfoil leading edge. If INGFDLNS has been used than ILE will be 3.

ITEL - Grid index for the airfoil trailing edge.

ITEU - This parameter is for an upper trailing edge location. However, the program does not use this parameter, so ITEU = 0.

CARD 4:

XM1 - Freestream Mach number.

RE - Reynolds number based on airfoil chord.

TW - Wall temperature normalized by freestream temperature (see IADW parameter).

S1 - Parameter for Southerland's law ($S1=C_2^*$).

ALFA - Angle of attack (degrees).

CARD 5:

IADW - Flag for adiabatic wall conditions. If IADW is 0 then TW must be specified; if IADW is 1 then TW must be 999.

CARDS 6-7:

OMEGA0, TOMG0, AFL0,ALF1, RFREQ - These parameters are for non-stationary airfoils. For analysis with stationary airfoils (as done in this study) these parameters are 0.

CARD 8:

CMOM - Reference point in the x-direction, normalized by airfoil chord, for computation of the pitching moment.

XC, YC - These parameters are for non-stationary airfoils. For analysis with stationary airfoils (as done in this study) these parameters are 0.

CARD 9:

IOFLW1 - Inflow/outflow boundary transition point for the upper surface. From this azimuthal grid index to IOFLW2, the outflow boundary conditions are imposed at the far-field boundary. A typical value is a grid index 3-5 points past midchord.

IOFLW2 - Inflow/outflow boundary transition point for the lower surface.

CARD 10:

IMOVE, IMPB - These parameters are for non-stationary airfoils. For analysis with stationary airfoils (as done in this study) these parameters are 0.

CARD 11:

NTURB - Iteration number for inclusion of the turbulence model. For high Reynolds numbers, the turbulence model should be included when *DTVIS is greater than zero.* Typically, The turbulence model is included in the algorithim at iteration 101.

IFREQ - Once the turbulence model is included in the analysis, IFREQ specifies now often the turbulence is recalculated. Nominally, the turbulence model should be recalculated every iteration, so IFREQ = 1.

CARD 12:

JLAST - This is a modification to the Baldwin-Lomax turbulence model to handle wake regions. It is a limit on how far out (normal direction) the turbulence model will search for the end of the boundary layer region. JLAST should be set to a value corresponding to the JMAX values calculated in the flow field before separation.

JFMAX - This is associated with the previous parameter. This parameter limits the number of indices in the normal direction to find FMAX and JMAX. Nominally, JFMAX = JLAST - 1. In addition, the output flag IFLAG must be watched. If IFLAG=0, the turbulence model is modeling a normal boundary layer, otherwise the turbulence model is modeling a separated wake region.

IJ1, IJ2 - Azimuthal grid indices for a region (on the surface) where the turbulence model is not used. This option is intended for use around sharp edges, i.e. jet slot.

IJBL - This defines the type of boundary layer for the region between IJ1 and IJ2. If IJBL is set to 0, then the region is laminar. If IJBL=1, then the region is turbulent and the eddy viscosity is linearly interpolated.

CARD 13:

ITRAN - Iteration number when the code starts to use the pressure gradient transition criteria. With this criterion the boundary layer transition point will be at the point of minimum pressure, if the point of minimum pressure is located between the stagnation point and DSTR1/2. This criteria will give a conservatively high estimate of the drag. This criteria should not be used until the turbulent boundary layer has converged sufficiently.

DSTR1 - Upper surface boundary layer transition location. Measured in arc lengths, normalized by the chord, form the stagnation point. See reference 23 Fig 17.9 for typical values.

DSTR2 - Lower surface boundary layer transition location.

CARD 14:

NDTAU - This number specifies the iteration when a new time step will be computed. Typically this option is not exercised.

CFL - Courant-Fredrichs-Lewy number. To avoid instabilities, CFL should be 1 for the first several iterations (approximately 100) while the initial condition is adapting to the current geometry. Later CFL can be increased, typically to 10.

BETA - Specifies the type of time stepping used by the algorithim.

BETA=0 -- time accurate solution where the time step is constant and equal to DTVIS.

BETA=1 -- local time stepping for steady state solution. The time step is the maximum of DTVIS or CFL times DTCFL.

DTVIS - Time interval. For local time stepping DTVIS should be 0 for initial iterations. For later iterations set DTVIS to .002 if possible.

CARD 15:

ISPECT - If set to one a scaling factor will be calculated for the fourth order damping coefficients. If ISPECT=0 then no fourth order damping will be added. Typically ISPECT=1.

WE, WI - Fourth order damping factors. Nominally WE should be between .01 and .02 with WI between .025 and .05. Typically WE=.01 and WI=.025. If these parameters have a significant effect on the solution then the grid resolution may not be sufficient for the case being examined.

WPE, WPI - Additional damping factors to be used in regions where supersonic flow exists. Should be between .1 and .5. For flows without any supersonic regions these values should be 0.

CARD 16:

INMAX - Maximum number of iterations to perform.

NCONV - Convergence and force data is written to appropriate files every NCONV iterations.

CARD 17:

ISLOT1, ISLOT2 - Azimuthal indices defining the location of the jet slot.

TPR - The non-dimensional ratio of jet total pressure to freestream static pressure.

$$T_{pr} = \frac{1}{\gamma M_\infty^2}\left(\frac{P_{o_{jet}}}{P_\infty}\right)$$

TTR - The ratio of jet total temperature to freestream static temperature.

$$T_{Tr} = \left(\frac{T_{o_{jet}}}{T_\infty}\right)$$

CARD 18:

ICURV - If this flag is 0, then the Bradshaw curvature correction is not used. If ICURV is 1, then the Bradshaw curvature correction is used.

CALP - Is the empirical constant, θ, in the Bradshaw curvature correction equation.

FCMIN, FCMAX - The minimum and maximum values of the Bradshaw curvature correction. Nominally, values of 0.5 and 1.5, respectively, are used.

APPENDIX D. Flow Regimes Around a Cylinder

Even though the geometry may be "simple", the flow around a two-dimensional circular cylinder is very complicated. The following list is a breakdown of the various flow regimes around a cylinder. The information was obtained form a variety of sources and the various regime titles are those most commonly used throughout the literature (2,21,22). The Reynolds number breakpoints are approximate; exact values are a function of freestream turbulence, surface roughness, etc.

Reynolds number	Flow Description
0 - 5	"Stokes range". This regime is typified by no separation and a seemingly inviscid fluid. The drag coefficient is very high but drops off quickly as the Reynolds number is increased, see Figure 37.
5 - 40	"Symmetrical wake region". The flow separates from the cylinder with the appearance of two counterrotating vortices. The flow is laminar up to the separation point. The pair of captive vortices are symmetric about the cylinder midplane. As the Reynolds number is increased the vortices elongate. The drag coefficient is steadily decreasing.
40 - 80	"Incipient Karmen vortex range". Instability sets in causing the vortices to become asymmetric and ultimately shedding occurs.
80 - 5000	"Pure Karmen range". A regular Karmen vortex street is established. The shedding frequency becomes periodic and is characterized by the Strouhal number.

5000 - 2 x 10^5	"Subcritical range". The disappearance of a regular vortex street and more of a quasi-periodic shedding typify this regime; the Strouhal number is constant at approximately 0.2. Laminar separation occurs before the flow reaches the vertical mid-plane.
2 - 4 x 10^5	"Critical range". In this regime, the drag is sharply reduced due to boundary layer transition. The laminar boundary layer separates from the cylinder. Immediately after separation, transition occurs. The turbulent flow reattaches to the body leaving a separation bubble on the surface of the cylinder. The higher energy of the turbulent boundary layer continues to flow along the body before finally separating near the aft end. The drag is reduced due to the decrease in the wake region. At first the flow is asymmetric due to the existence of only one separation bubble. As the Reynolds number is increased, a separation bubble forms on the opposite side and flow symmetry returns. The vortex shedding frequency is still quasi-periodic. The Strouhal number is no longer constant but has sharp discontinuities brought on by the flow phenomenon, see Figure 38.
4 - 10 x 10^5	"Supercritical range". The separation bubbles stabilize along with the drag coefficient. The quasi-periodic shedding continues.
1 - 5 x 10^6	"Upper transition". The quasi-periodic shedding is replaced by unperiodic broadband low frequency shedding, see Figure 39. The boundary layer transition occurs without the presence of the separation bubbles and the drag coefficient rises from the supercritical plateau (0.2) to the transcritical plateau (0.5).
5 x 10^6 and up	"Transcritical range". The periodic vortex shedding reappears in the transcritical regime and the drag coefficient levels off at 0.5.

Figure 37 represent effect of Reynolds number on the drag coefficient. Figure 38 is a closer look at the supercritical to transcritical regimes. The power spectra of the lift fluctuations is outlined in Figure 39. Note the lack a defined peak in pictures c and d.

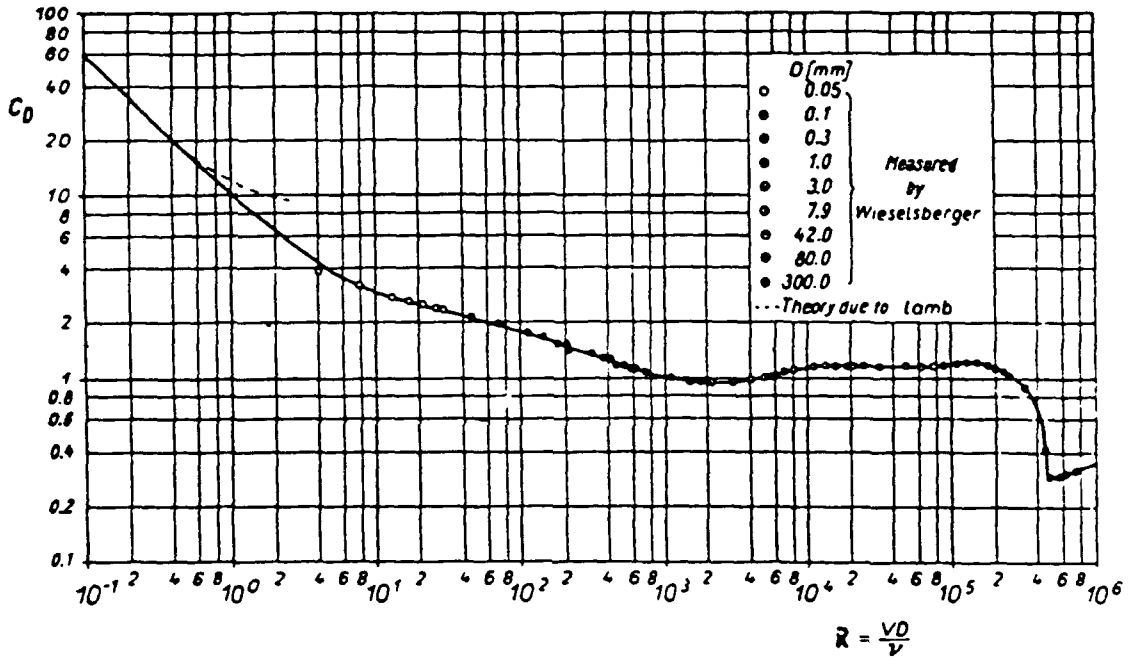

Figure 37. C_d versus Reynolds number for a cylinder (23)

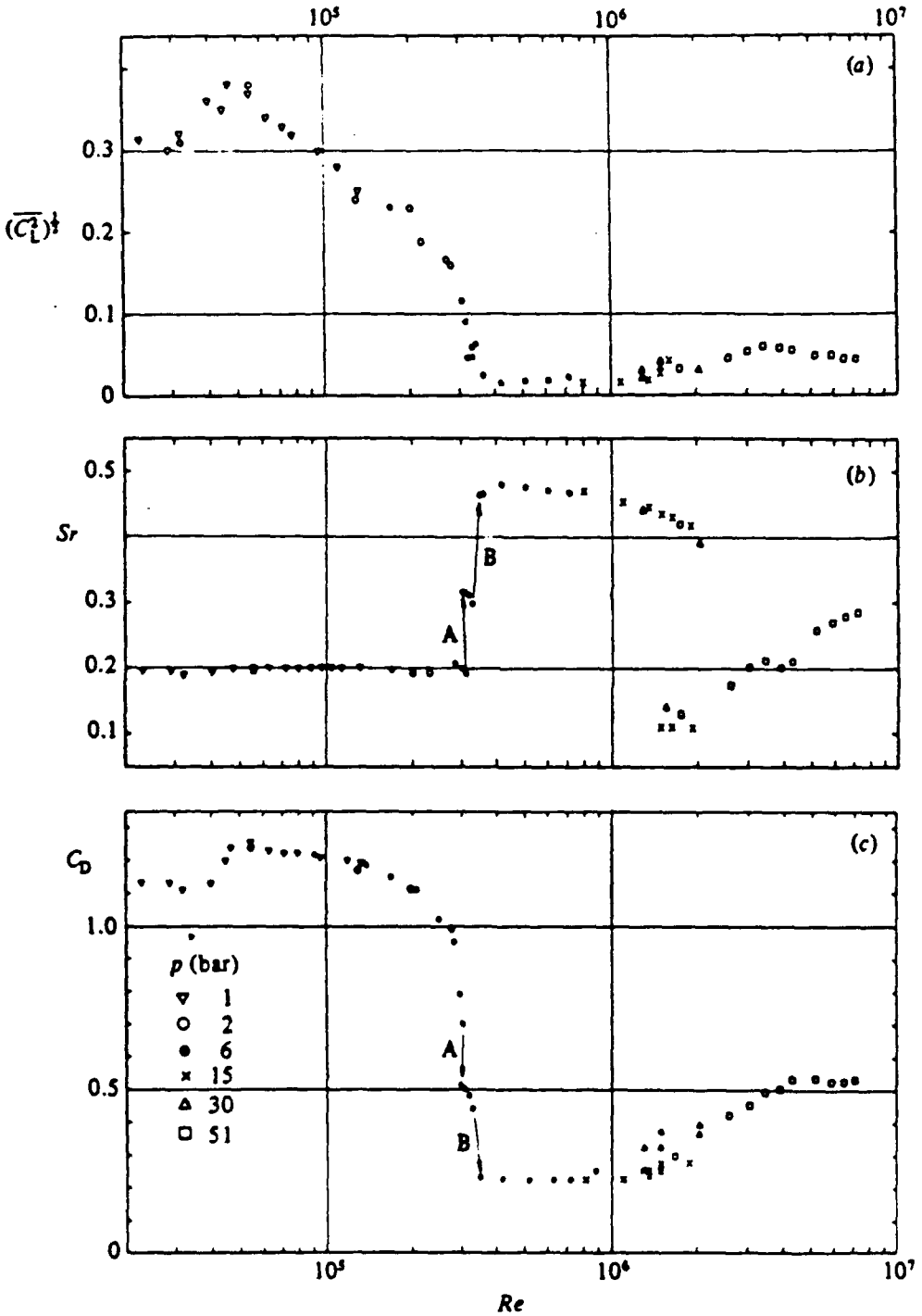

Figure 38. Re number effects in super to transcritical regime (Ref 22)

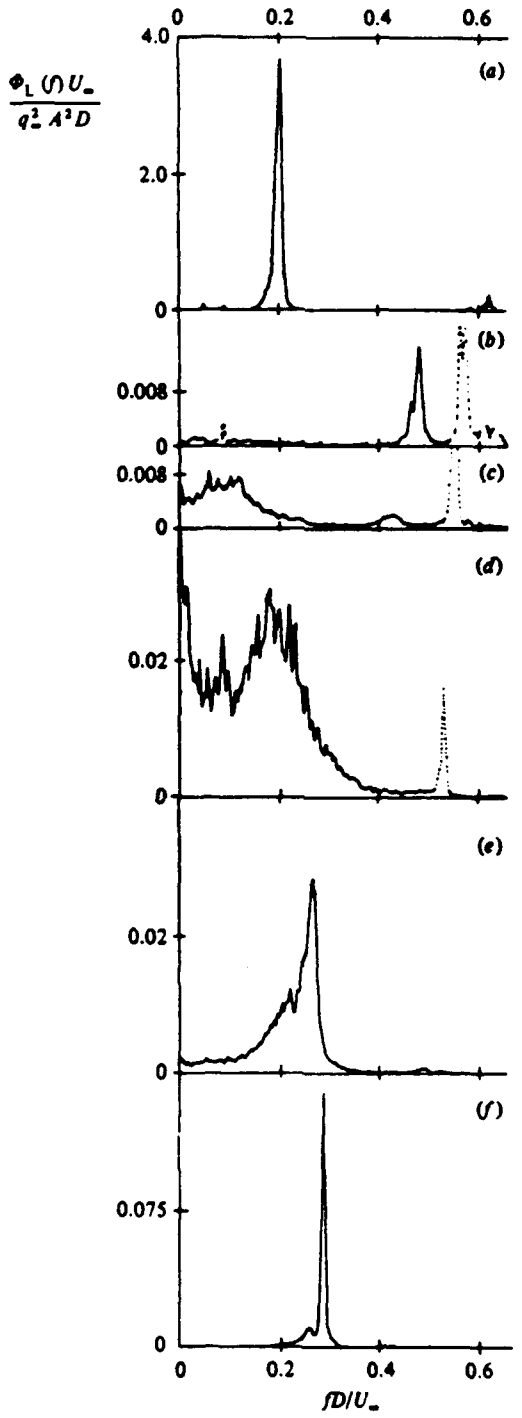

Figure 39. Power spectra of Lift Fluctuations. (a) Re=1.3x10^5, (b) Re=7.2x10^5, (c) Re=1.9x10^6, (d) Re=3.7x10^6, (e) Re=5.9x10^6, (f) Re=7.1x10^6 (ref 22).

Appendix E. Data Point 35 Plots

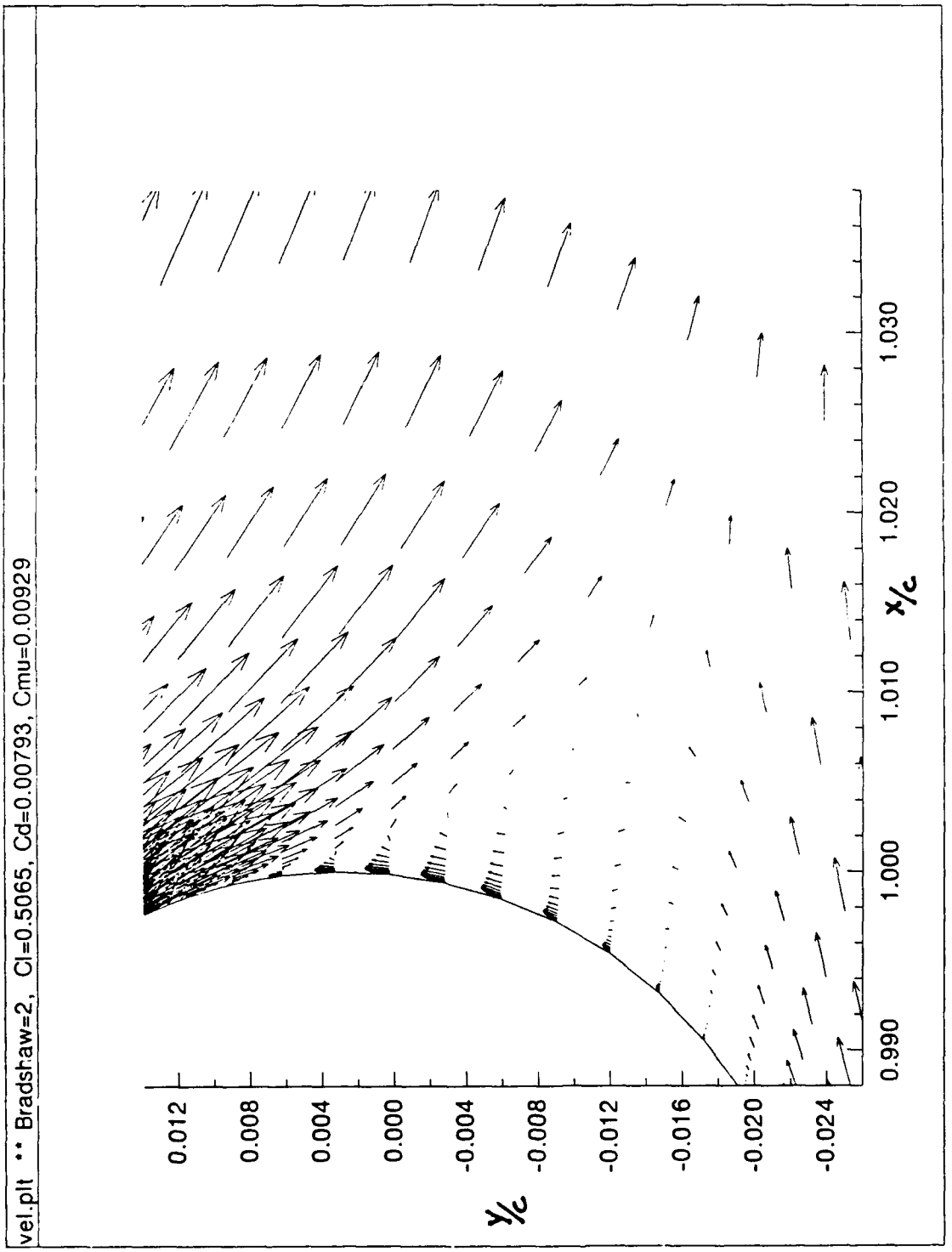

Figure 34. Velocity vectors, data point 35, Bradshaw=2

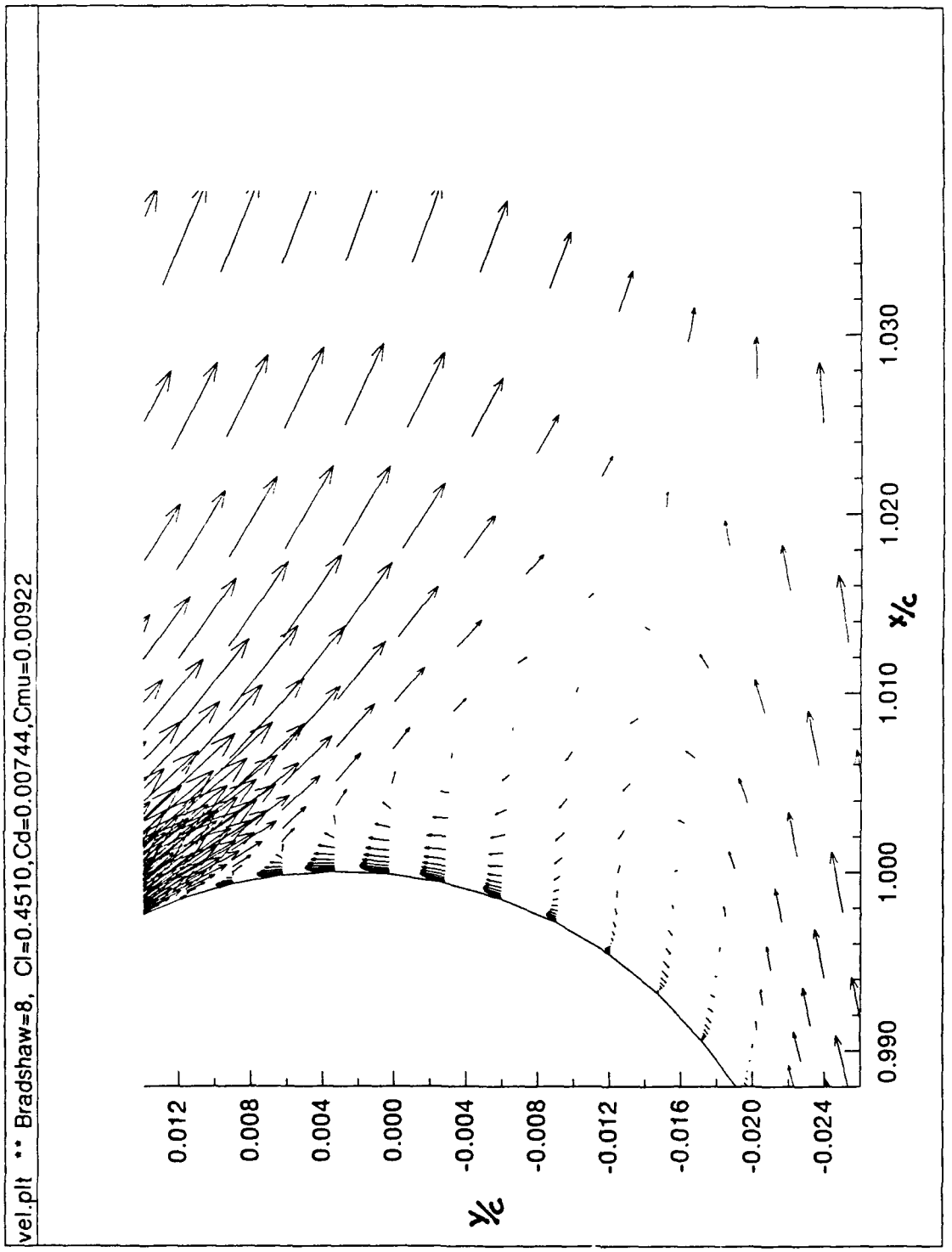

Figure 35. Velocity vectors, data point 35, Bradshaw=8

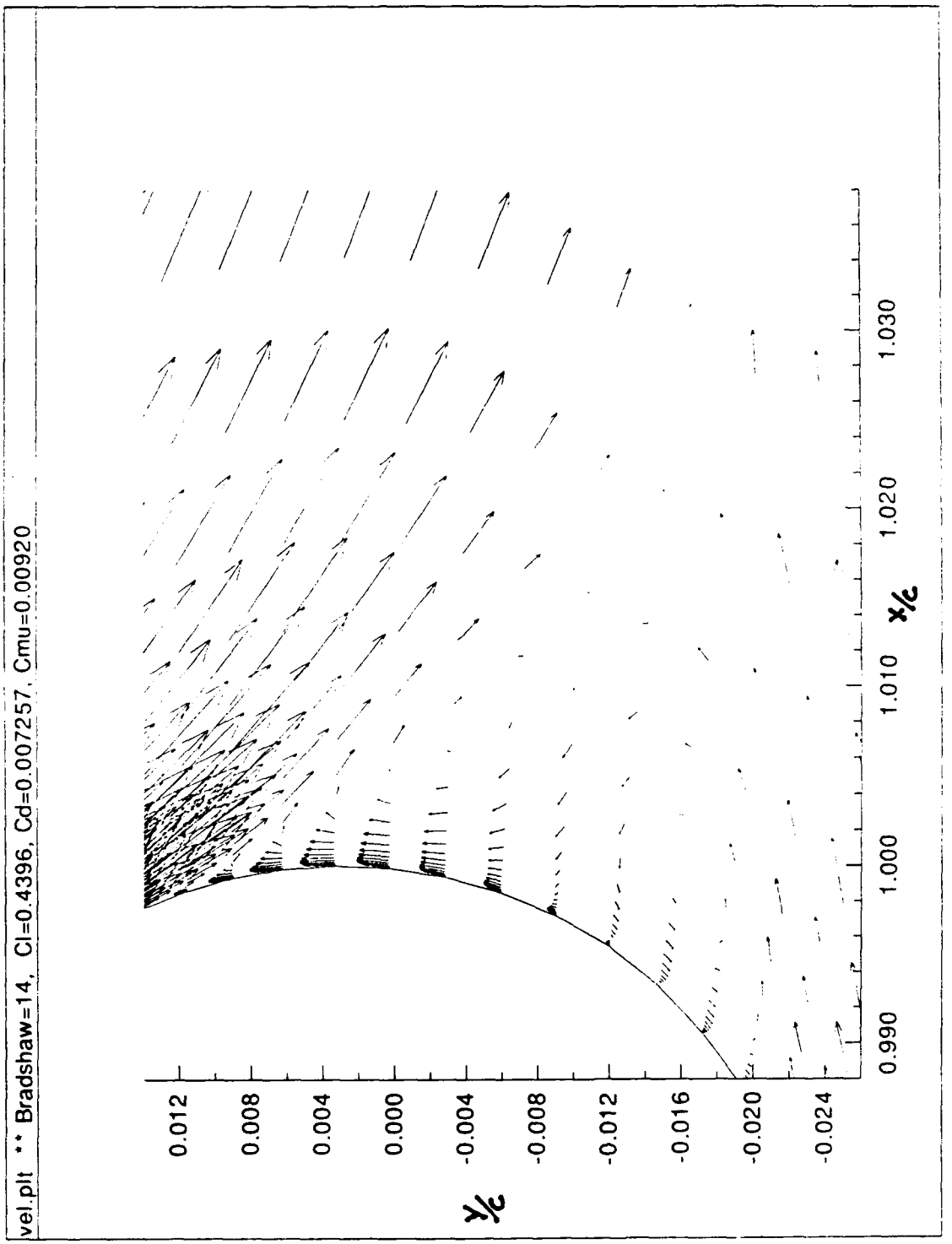

Figure 36. Velocity vectors, data point 35, Bradshaw=14

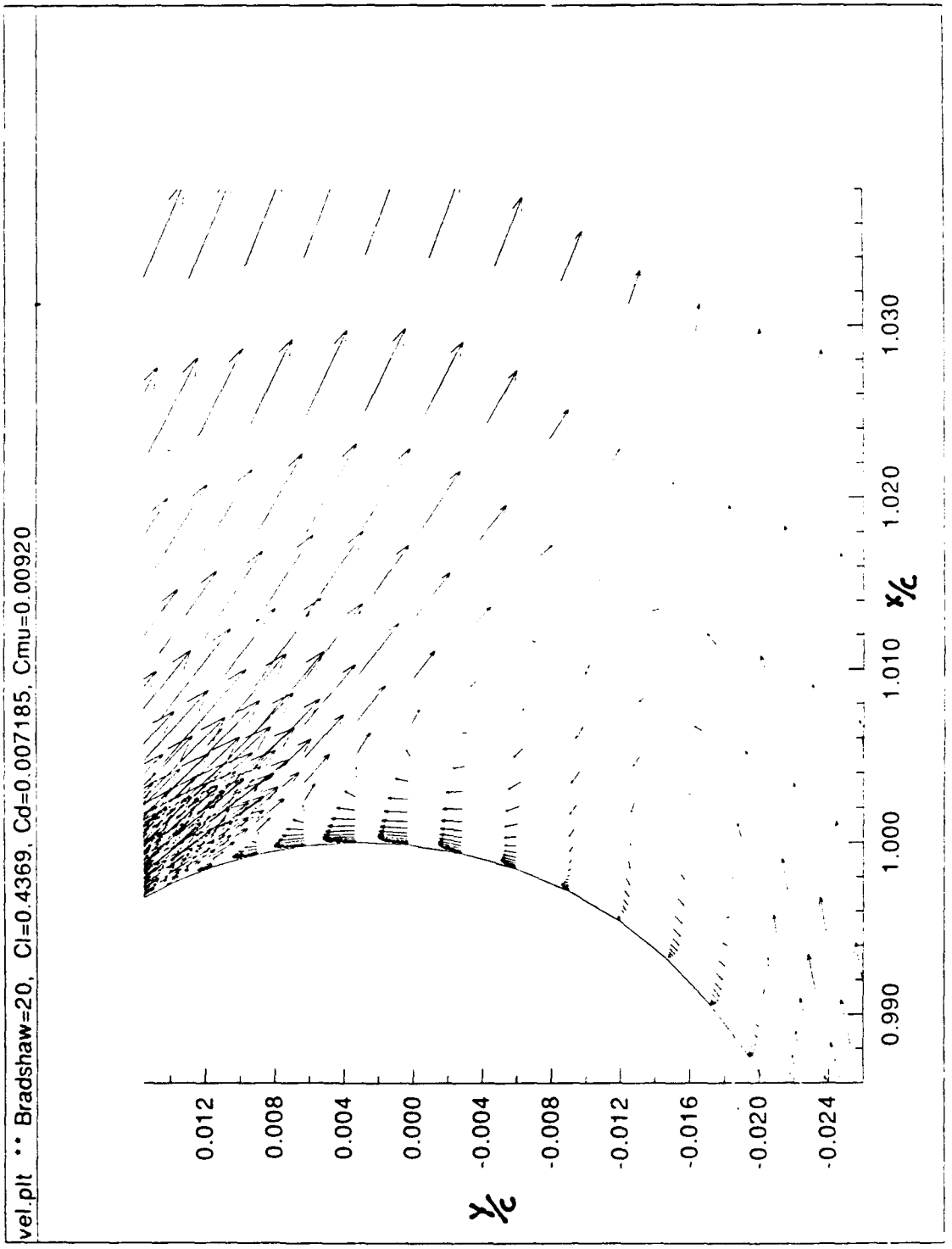

Figure 37. Velocity vectors, data point 35, Bradshaw=20

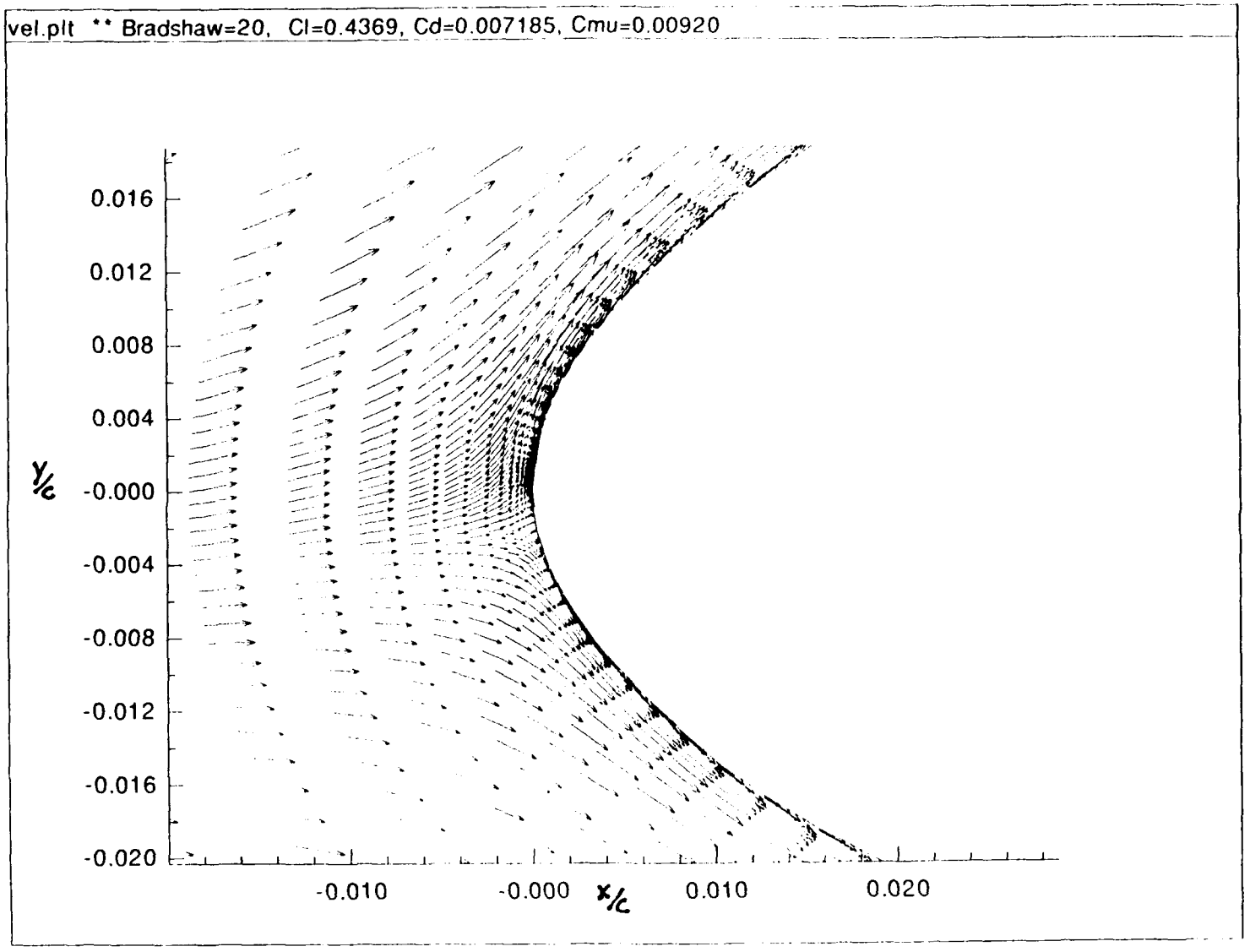

Figure 38. Velocity vectors, data point 35, Bradshaw=20

Appendix F. Data Point 36 Plots

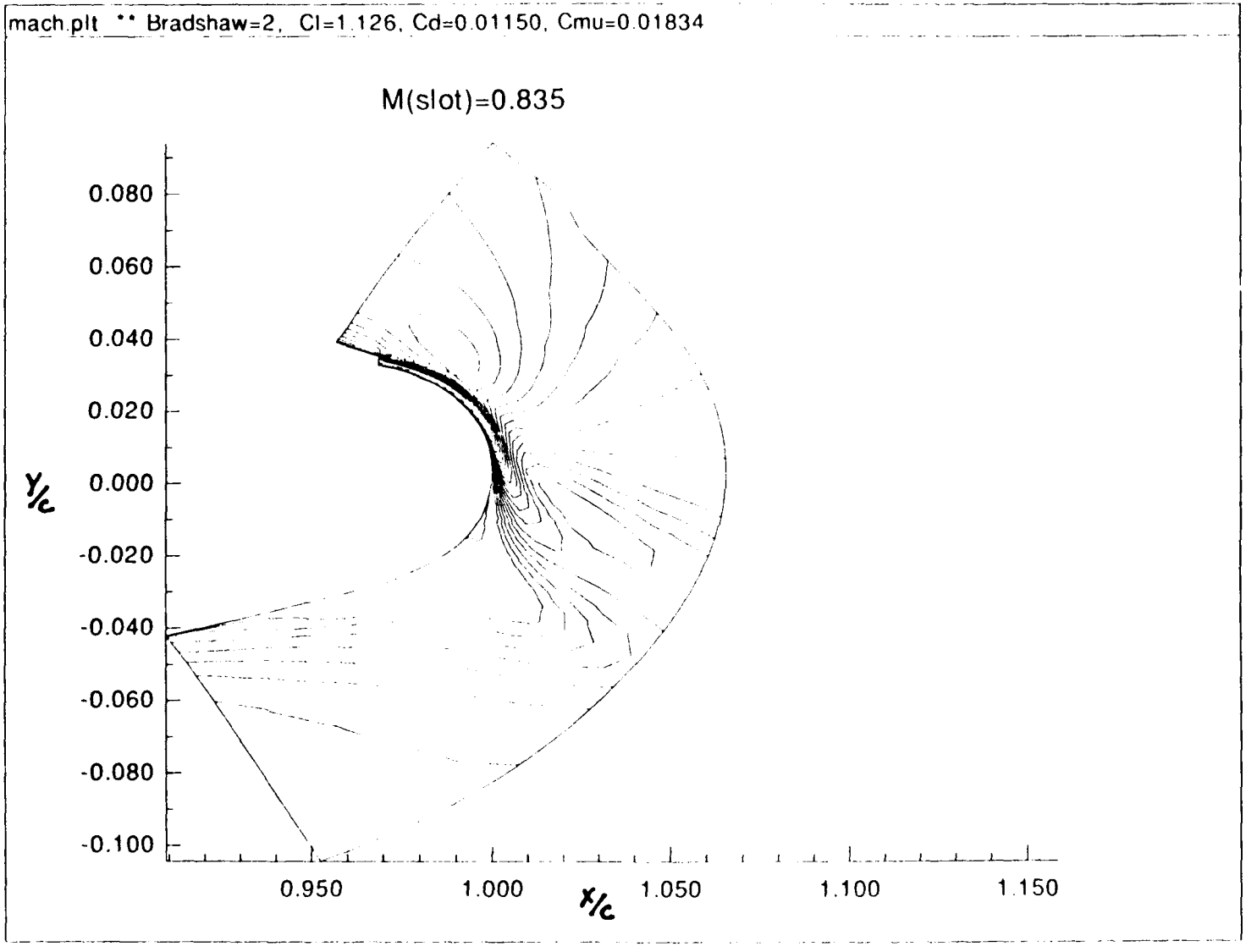

Figure 39. Mach contours, data point 36, Bradshaw=2

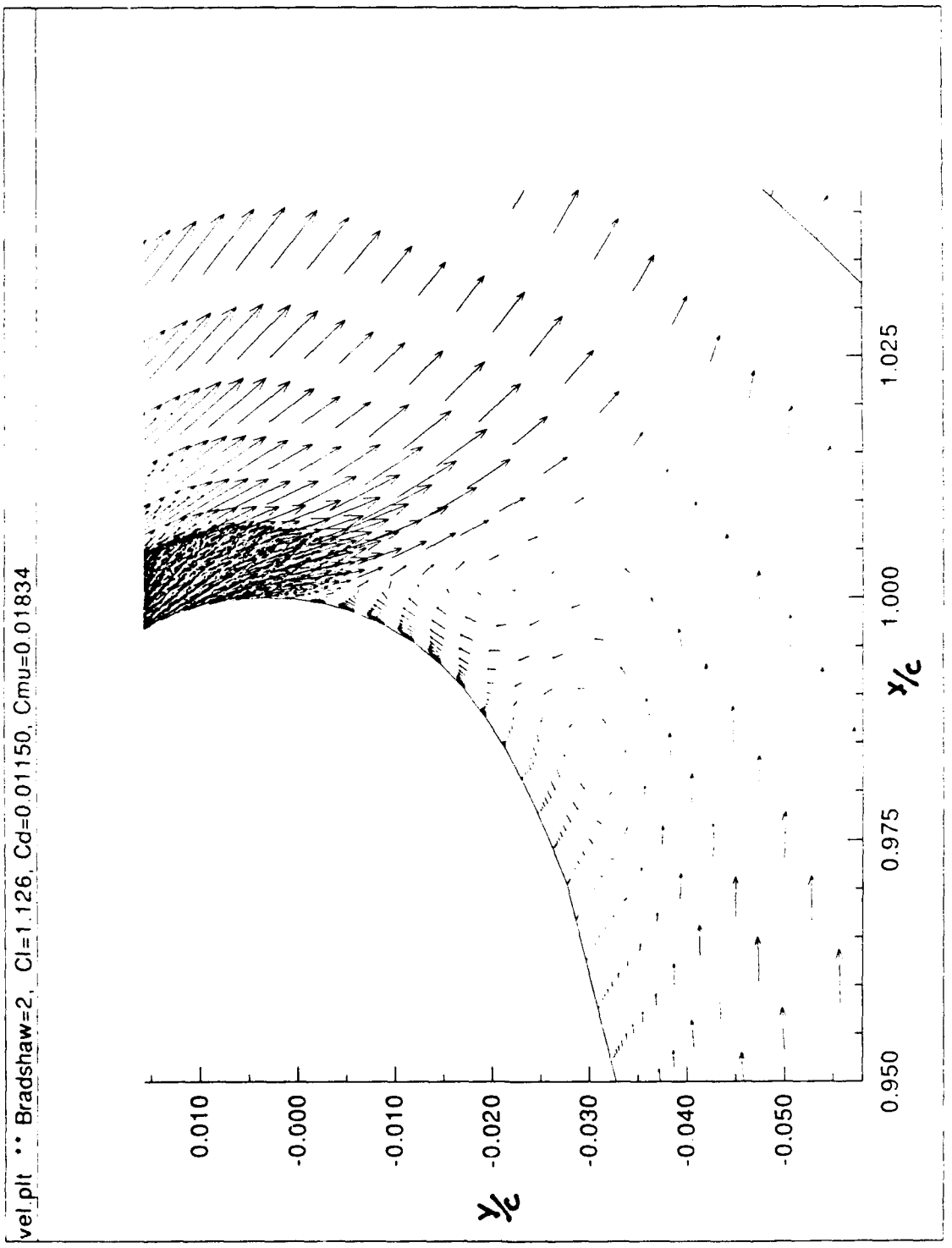

Figure 40. Velocity vectors, data point 36, Bradshaw=2

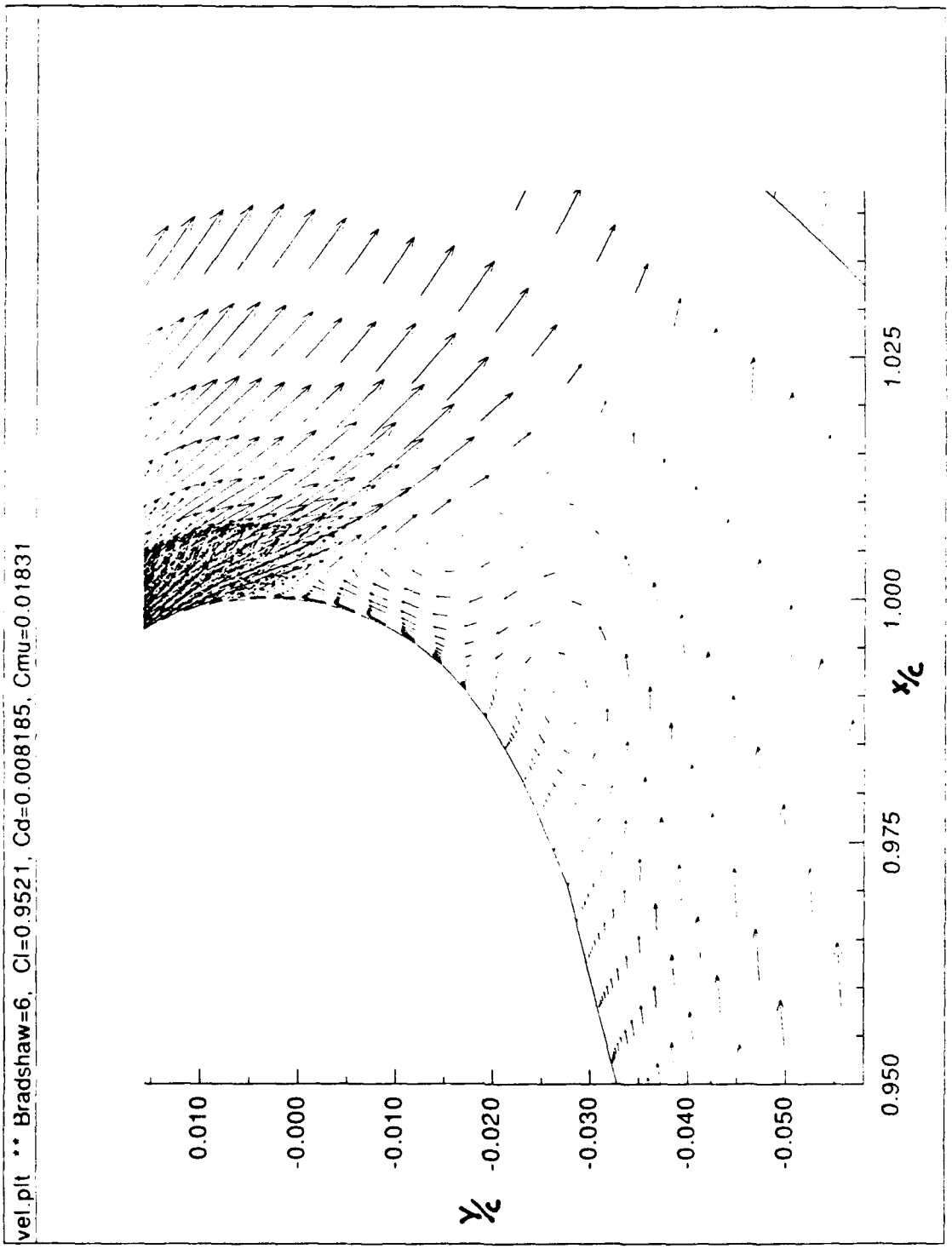

Figure 41. Velocity vectors, data point 36, Bradshaw=6

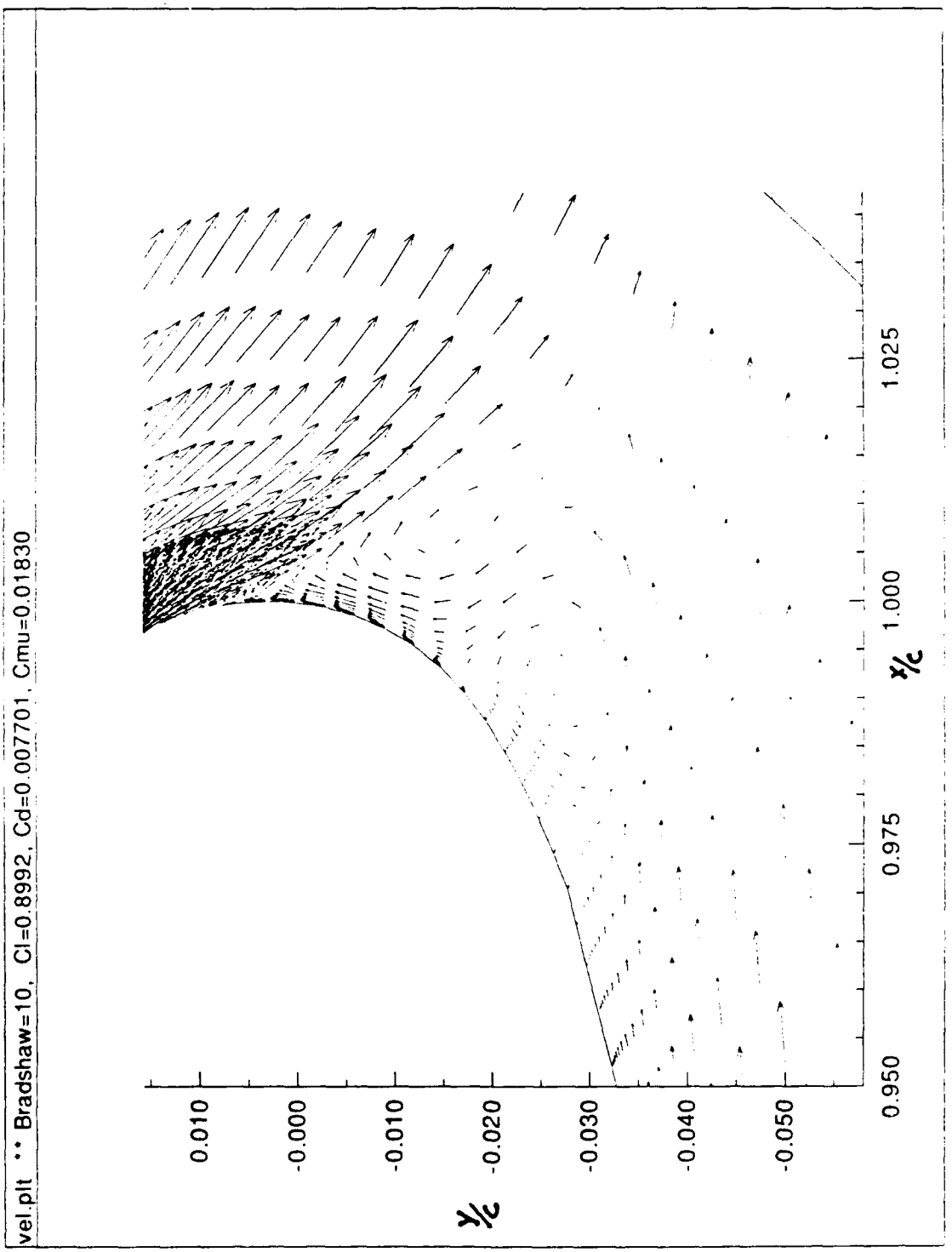

Figure 42. Velocity vectors, data point 36, Bradshaw=10

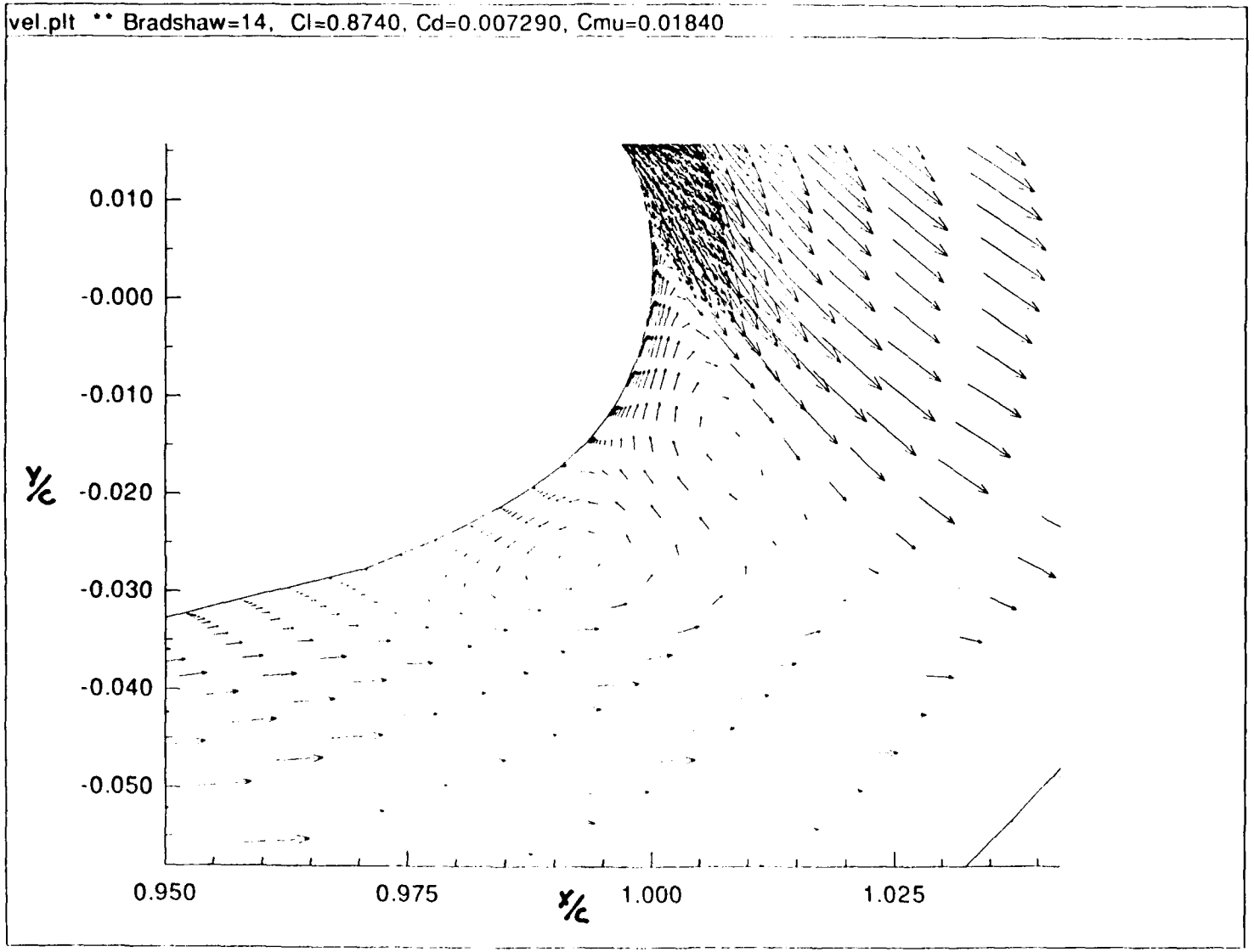

Figure 43. Velocity vectors, data point 36, Bradshaw=14

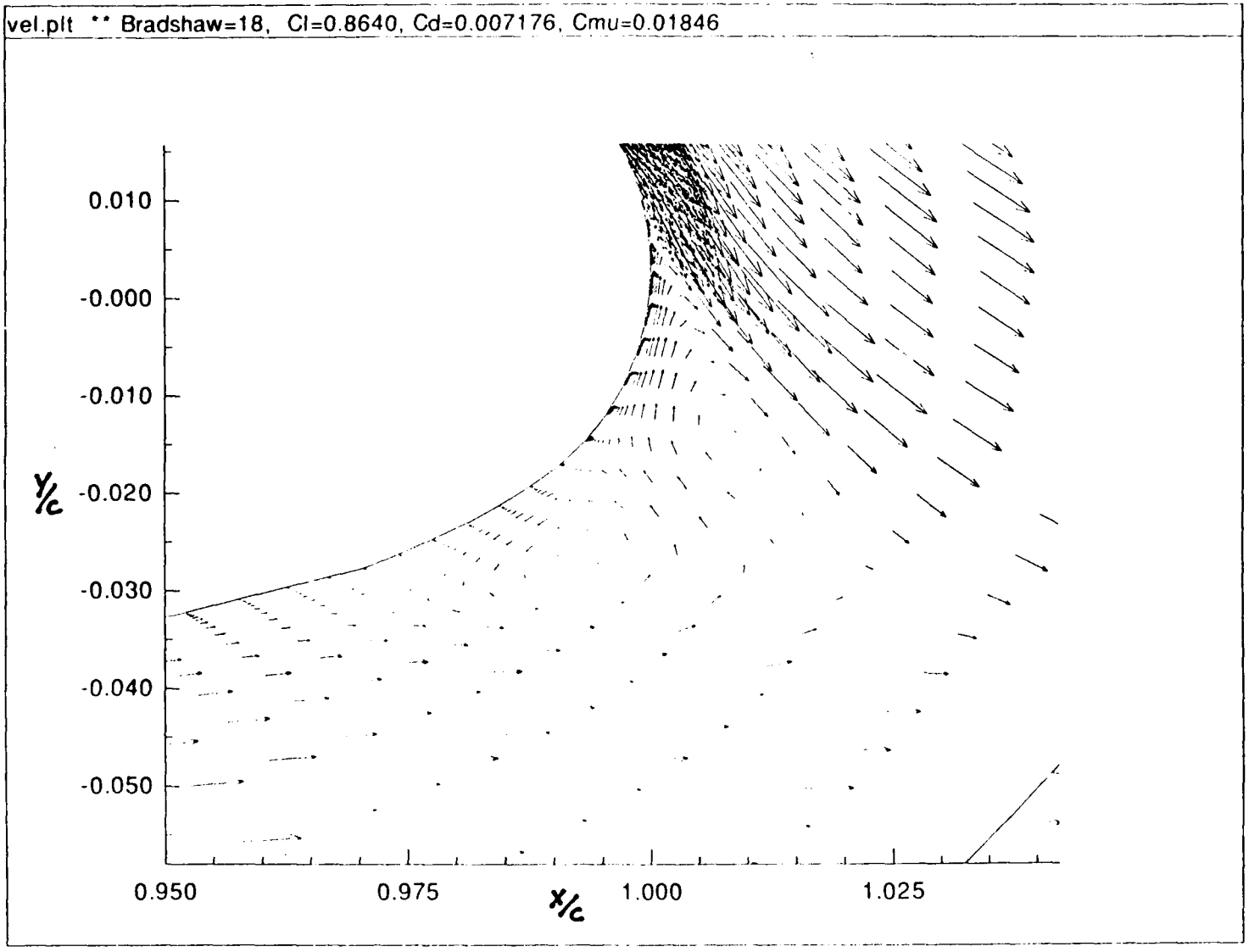

Figure 44. Velocity vectors, data point 36, Bradshaw=18

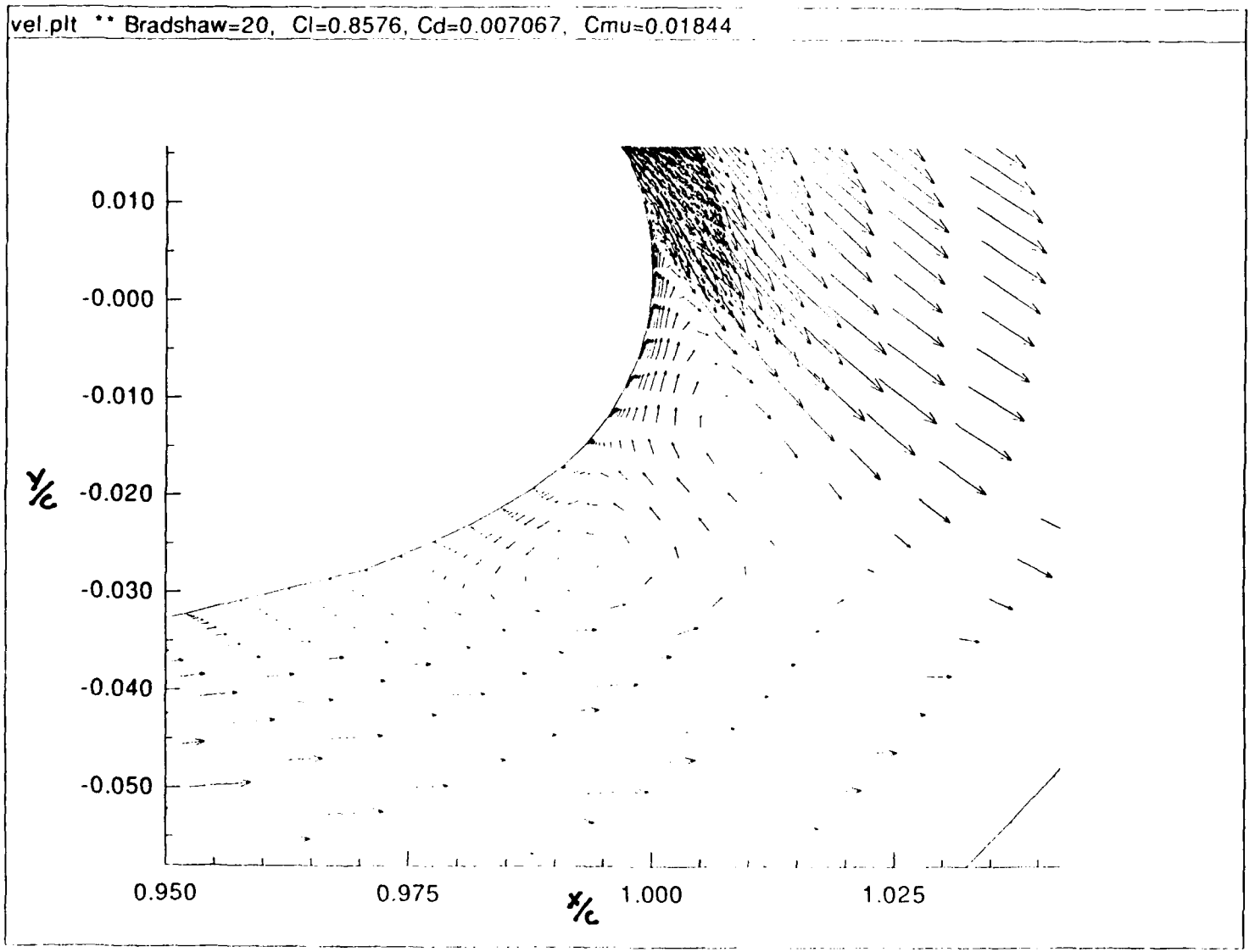

Figure 45. Velocity vectors, data point 36, Bradshaw=20

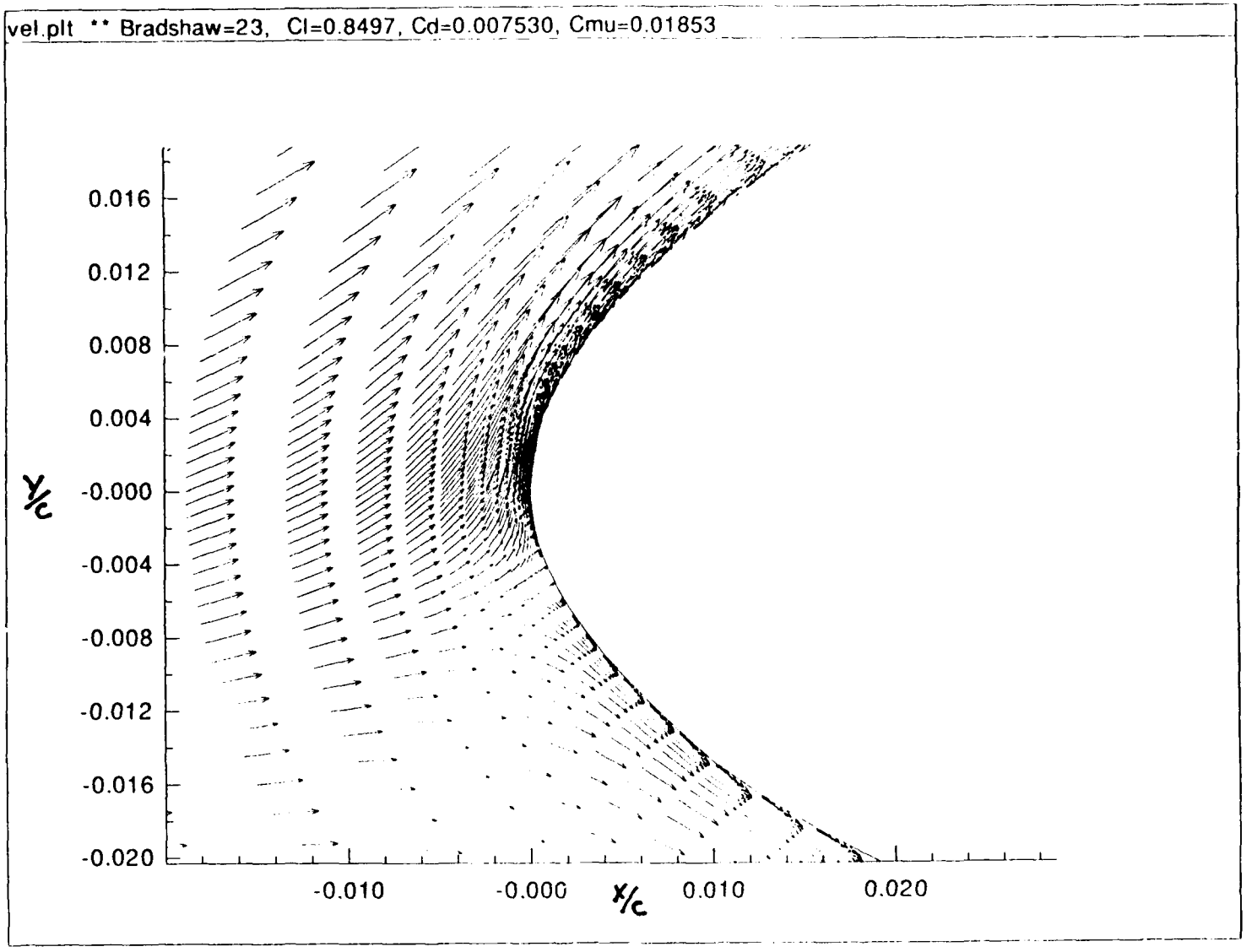

Figure 46. Velocity vectors, data point 36, Bradshaw=20

Bibliography

1. Abramson, J. and E. O. Rogers. "High-Speed Characteristics of Circulation Control Airfoils", Paper No 83-0265. *AIAA 21st Aerospace Science Meeting.* Reno, NV, January 1983.

2. Achenbach, E. "Distribution of Local Pressure and Skin Friction Around a Circular Cylinder in Cross-Flow up to $Re=5x10^6$", *Journal of Fluid Mechanics*,34:625-639 (December 1968).

3. Anderson, D. A., J. C. Tannehill, and R. H. Pletcher. *Computational Fluid Mechanics and Heat Transfer.* New York: Hemisphere Publishing Corp., 1984.

4. Baldwin, B. S. and H. Lomax. "Thin Layer Approximation and Algebraic Model for Separated Turbulent Flows", Paper No. 78-257. *AIAA 16th Aerospace Sciences Meeting.* Huntsville, AL, January 1987.

5. Beam, Richard M., and R. F. Warming. "An Implicit Factored Scheme for the Compressible Navier-Stokes Equations", AIAA Journal. Vol. 16, No. 4, April 1978.

6. Bradshaw, P. "Effects of Streamline Curvature on Turbulent Flow," *AGAR-Dograph No. 169.* London: Technical Editing and Reproduction Ltd, August 1973.

7. Cheeseman, I. C. and A. R. Seed. "The Application of Circulation Control by Blowing to Helicopter Rotors", *Aeronautical Journal of the Royal Aeronautical Society.* Vol. 71, No. 848, July 1966.

8. Dunham, J. "A Theory of Circulation Control by Slot Blowing Applied to a Circular Cylinder," *Journal of Fluid Mechanics.* Vol. 33 1968.

9. Englar, R. J. and G. G. Huson. *Circulation Control-An Updated Bibliography of DTNSRDC Research and Selected Outside References.* DTNSRDC Report 84-052. September 1984.

10. Ishii, K., Kuwahara, K., Ogawa, S., Chyu, W. J. and Kawamura, T., "Computation of Flow Around a Circular Cylinder in a Supercritical Roughness," Paper 85-1660. *AIAA 23rd Aerospace Sciences Meeting.* Reno, NV, January 1985.

11. Karamcheti, Krishnamurty. *Principles of Ideal-Fluid Aerodynamics.* Florida: Robert E. Krieger Publishing Company, 1966.

12. Kinsey, Don W. and Timothy J. Barth. *Description of a Hyperbolic Grid Generating Procedure For Arbitrary Two-Dimensional Bodies*, AFWAL-TM-84-FIMM. WPAFB OH, July 1984.

13. Launder, B. E. and D. B. Spalding. "The Numerical Computation of Turbulent Flows," *Computer Methods in Applied Mechanics and Engineering*. Vol. 3:269-289 (1974).

14. Levinsky, E. S. and T. T. Yeh. *Analytical and Experimental Investigation of Circulation Control by Means of a Turbulent Coanda Jet*, NASA CR-2114. Washington, D. C., September 1972.

15. Lockwood, V. E. *Lift Generation on a Circular Cylinder by Tangential Blowing from Surface Slots*, NASA TN-D-244. Washington, D. C., May 1960.

16. Lutton, Capt Mark J. *Comparison of C- and O- Grid Generation Methods Using a NACA 0012 Airfoil*. MS thesis, AFIT/GAE/ENY/89D-21. School of Engineering, Air Force Institute of Technology (AU), Wright-Patterson AFB OH, December 1989.

17. Nielsen, Jack N. and James C. Biggers. "Recent Progress in Circulation Control Aerodynamics," Paper 87-0001. *AIAA 25th Aerospace Science Meeting*. Reno, NV, January 1987.

18. ---. "Proceedings of the Circulation Control Workshop 1986," NASA CP-2432. *Proceeding of a workshop at NASA Ames Research Center*. February 1986.

19. Peyret, Roger and Thomas D. Taylor. *Computational Methods for Fluid Flow*. New York: Springer-Verlag, 1984.

20. Pulliam, Thomas H. et al. "Navier-Stokes Computations for Circulation Control Airfoils," *Proceedings of the Circulation-Control Workshop 1986*. NASA CP-2432. Washington: NASA, May 1987.

21. Roshko, A. "Experiments of the Flow Past a Circular Cylinder at Very High Reynolds Number," *Journal of Fluid Mechanics*. Vol. 34 1968.

22. Schewe, G. "On the Force Fluctuations Acting on a Circular Cylinder in Crossflow from Subcritical Up to Transcritical Reynolds Numbers," *Journal of Fluid Mechanics*, Vol. 133 (August 1983).

23. Schlichting, Hermann. *Boundary-Layer Theory (Seventh Edition).* NY: McGraw-Hill Book Company, 1979.

24. Shrewsberry, George D. "Numerical Study of a Research Circulation Control Airfoil Using Navier-Stokes Methods," *Journal of Aircraft*, Vol. 26, pg 29, (January 1989).

25. ---. "Evaluation of a Research Circulation Control Airfoil Using Navier-Stokes Methods," Paper 87-0002. *AIAA 25th Aerospace Sciences Meeting.* Reno, NV, January 1987.

26. ---. "Analysis of Circulation Control Airfoils Using an Implicit Navier-Stokes Solver." Paper 85-0171. *AIAA 23rd Aerospace Science Meeting.* Reno, NV, January 1985.

27. Smith, R. V. *A Theoretical and Experimental Study of Circulation Control With Reference to Fixed Wing Applications.* PhD Dissertation. Department of Aeronautics and Astronautics, University of Southampton, July 1978.

28. Visbal, M. R. "Evaluation of an Implicit Navier-Stokes Solver for Some Unsteady Separated Flows," Paper 86-1053. *AIAA/ASME 4th Fluid Mechanics, Plasma Dynamics and Lasers Conference.* Atlanta, GA, May 1986.

29. ---. *Calculation of Viscous Transonic Flows About a Supercritical Airfoil.* Technical Report, AFWAL, Flight Dynamics Laboratory, WPAFB OH, 1986. AFWAL-TR-86-3013.

30. Warming, R. F. and Richard M. Beam. "On the Construction and Application of Implicit Factored Schemes for Conservation Laws," *SIAM-AMS Proceedings*,Vol. 11, p.85.

31. Williams, Steven W. *Use of navier-Stokes Methods to Predict Circulation Control Airfoil Performance.* MS Thesis, AFIT/GAE/AA/89M-4. School of Engineering, Air Force Institute of Technology (AU), Wright-Patterson AFB, OH, March 1989.

32. Wood, N. and J. Nielsen. "Circulation Control Airfoils Past, Present and Future," Paper 85-0204. *AIAA 23rd Aerospace Sciences Meeting.* Reno, NV, January 1985.

Vita

Captain T. Bryan Scruggs was born on the sixteenth of August, 1962 in Richmond, Virginia. In 1980, he graduated from Henrico High School. He then proceeded to Auburn University in Auburn, Alabama. He graduated from Auburn in 1985 with a Bachelor of Aerospace Engineering degree. He joined the Air Force and went to Officer Training School. After being commissioned, he was stationed at Falcon AFB in Colorado Springs, Colorado. At Falcon AFB, Captain Scruggs worked as satellite integration engineer with the Global Positioning System (GPS/NAVSTAR). From there, he was accepted by the Air Force Institute of Technology to obtain a Master of Science degree in Aeronautical Engineering (hopefully).

Permanent address: 2311 Greenway Ave
Richmond, VA 23228

REPORT DOCUMENTATION PAGE

Form Approved
OMB No 0704-0188

Public reporting burden for this collection of information is estimated to average 1 hour per response, including the time for reviewing instructions, searching existing data sources, gathering and maintaining the data needed, and completing and reviewing the collection of information. Send comments regarding this burden estimate or any other aspect of this collection of information, including suggestions for reducing this burden, to Washington Headquarters Services, Directorate for information Operations and Reports, 1215 Jefferson Davis Highway, Suite 1204, Arlington, VA 22202-4302, and to the Office of Management and Budget, Paperwork Reduction Project (0704-0188), Washington, DC 20503.

1. AGENCY USE ONLY (Leave blank)	2. REPORT DATE	3. REPORT TYPE AND DATES COVERED
	December 1990	Master's Thesis

4. TITLE AND SUBTITLE
Computational Investigation of Circulation Control Turbulence Modeling

5. FUNDING NUMBERS

6. AUTHOR(S)
T. Bryan Scruggs, Captain, USAF

7. PERFORMING ORGANIZATION NAME(S) AND ADDRESS(ES)
Air Force Institute of Technology, WPAFB OH 45433-6583

8. PERFORMING ORGANIZATION REPORT NUMBER
AFIT/GAE/ENY/90D-27

9. SPONSORING MONITORING AGENCY NAME(S) AND ADDRESS(ES)
Dr. Joe Shang WRDC/FIMM
Wright-Patterson AFB, OH 45433-6583

10. SPONSORING MONITORING AGENCY REPORT NUMBER

11. SUPPLEMENTARY NOTES

12a DISTRIBUTION AVAILABILITY STATEMENT
Approved for public release;
distribution unlimited

12b. DISTRIBUTION CODE

13. ABSTRACT (Maximum 200 words)

A computational study of the turbulence model parameters and the effect on the flow field of a circulation control airfoil was conducted. A Beam-Warming algorithm with a modified Baldwin-Lomax turbulence model was used to solve the Navier-Stokes equations. A comparison between the effects of the Bradshaw constant on the flow field about the cylinder and the flow field about an airfoil were to be made. The lack of a steady "converged" solution for the cylinder precluded the analysis of the flow field about a cylinder. For the airfoil, the separation point moves rearward and an enhanced vortex pattern is developed as the Bradshaw constant is increased. Once a high enough value is reached, the curvature correction has minimal effect. The results obtained indicate that a better turbulence model must be employed before CFD can be used to accurately predict the flow around a circulation control airfoil.

14. SUBJECT TERMS	15. NUMBER OF PAGES
Circulation control, Computational fluid dynamics, Beam-Warming algorithim, Navier-Stokes equations	120
	16. PRICE CODE

17. SECURITY CLASSIFICATION OF REPORT	18. SECURITY CLASSIFICATION OF THIS PAGE	19. SECURITY CLASSIFICATION OF ABSTRACT	20. LIMITATION OF ABSTRACT
unclassified	unclassified	unclassified	UL